NASA CR 65484

SOIL EROSION BY LANDING ROCKETS

CONTRACT NAS9-4825

FINAL REPORT

HAYES
INTERNATIONAL CORPORATION
BIRMINGHAM, ALABAMA

HAYES
INTERNATIONAL CORPORATION
BIRMINGHAM, ALABAMA

SOIL EROSION BY LANDING ROCKETS

CONTRACT NAS9-4825

FINAL REPORT

Engineering Report No. 1301

15 July 1966

PREPARED BY:

J. D. Alexander
Dr. J. D. Alexander

W. M. Roberds
Dr. W. M. Roberds

R. F. Scott (by J.D.A.)
Dr. R. F. Scott

APPROVED BY:

J. D. Alexander
J. D. Alexander
Project Manager

P. R. Coulson
P. R. Coulson
Program Manager

REVISIONS

DATE	PAGES AFFECTED	REMARKS	BY	APP.

FORM E-509 REV. 2/3/61

ABSTRACT

A test program involving a series of pressurized cold gas (nitrogen) firings and a series of live rocket firings has been conducted to evaluate the cratering which would be expected from a re-entry capsule using retro rockets to assist in a soft earth landing. These firings involved both stationary jets and jets moving with horizontal velocities as high as 30 ft/sec over sand, scalped earth and sod soils.

It was found that for jet surface pressures above a critical value, cratering resulted from an "explosive" failure of the material as the yield strength of the soil below the surface was exceeded. For lower surface pressures cratering results from a relatively gradual erosion action.

A somewhat detailed theoretical model has been developed to explain the explosive cratering resulting from a single rocket at normal incidence in the soil surface. Also, a simplified method has been developed which will permit engineering estimates of crater dimensions to be made over a variety of jet-soil conditions.

The jet and soil properties which are significant in crater formation have been defined in a manner suitable for engineering applications over a wide range of terrestrial conditions.

Mr. Jerry E. McCullough, Landing Technology Branch, was the Technical Supervisor and the work herein reported was accomplished under Contract No. NAS9-4825 with Manned Spacecraft Center, National Aeronautics and Space Administration.

TABLE OF CONTENTS

TABLE OF FIGURES

TABLE OF FIGURES (Cont'd)

TABLE OF FIGURES (Cont'd)

SOIL EROSION STUDY (LANDING ROCKETS)

I. INTRODUCTION

The purpose of this project is to evaluate the effect of a descending rocket exhaust on soils in an earth environment.[1] Characteristic expressions and curves have been developed from theoretical analysis and experimental data which, along with rocket motor performance can be used to predict cratering effects during a soft earth landing.

Two general experimental methods have been used and the effects on sand, clay and sod surfaces have been studied.

(1) A series of cold flow tests were run using pressurized nitrogen through a nozzle used for the Honest John spin rocket -- throat diameter 0.54", perfectly expanded for chamber pressure, P_c= 271 psia. These tests were conducted in sand, clay and sod soils, and involved both a stationary jet and a moving jet with horizontal velocity components as high as 25 ft/sec.

(2) Also, a series of hot firing tests were run using surplus Honest John spin rockets. For the hot flow tests, the rockets were mounted on a descending carriage whose motion with respect to the ground simulated closely that of a landing capsule.

Information has been developed which defines the problem areas, provides assistance for retro-rocket scaling, and which describes basic effects of gas jets impinging on sand and clays. Some theory also has been developed to relate crater dimensions to the ground surface pressure and the soil characteristics.

II. SUMMARY AND CONCLUSIONS

1. Stationary Cold Gas Tests

The cold test apparatus (illustrated in Figure 1) consisted of a high pressure tank and controls mounted on a heavy trailer. This was used to provide gas flow through an Honest John spin rocket nozzle for thrust levels up to 650 pounds.

Most of the tests were made on soil samples in large bins, some tests were also run on previously undisturbed field soils.

(1) Contract NAS9-4825, Soil Erosion by Landing Rockets

A few tests were made with the nozzle canted at various angles from the vertical.

2. Moving Cold Gas Tests

Tests were also made with the jets moving horizontally at various nozzle heights and at speeds up to 25 ft/sec. These moving tests were made both in bins and in undisturbed field soils.

3. Hot Firing Tests - General Program

The tests were carried out with the configuration shown in Figure 2. These tests consisted of firing small jets (Honest John spin rockets) vertically downward as the rocket mount (or carriage) approached the earth at three angles between 41 degrees and 70 degrees. The vertical velocities, at the time of firing, were approximately 27 ft/sec in each case, but the horizontal velocity varied with the angle of approach - from about 10 ft/sec to 30 ft/sec.

The rocket was fired into three types of terrain: (1) dry sand in deep pits, (2) natural sod, (3) scalped earth, which consisted in large part of clay and silt.

4. Pressure Distribution on Surfaces

Pressure distribution on the surface within the impingement areas were measured for various chamber pressures and nozzle heights and for both flat and concave surfaces.

5. Soil Tests

Shear tests and moisture content determinations were made on the soil samples at the hot test site and a specimen of field soil was submitted to a testing laboratory for composition analysis.

6. General Conclusions

For low surface pressures, the cratering in sand is somewhat like that shown in studies by Leonard Roberts[2], Norman Land

(2) Roberts, Leonard: The Interaction of a Rocket Exhaust with the Lunar Surface. Presented at a Specialist' Mtg. on "The Fluid Dynamic Aspects of Space Flight" (Marseille, Fr.), AGARD, April 20-24, 1964.

and Leonard Clark[3] and Stitt[4]. However when the surface pressures become higher than some critical value, distinctly different phenomena occur:

(a) An entrainment phenomena ensues for about 50 milliseconds (for the particular jet-valve configuration) blowing away the loose surface areas and producing a small cavity or pocket on the surface. During this phase erosion begins, first under the center of the jet and then quickly spreading laterally.

(b) Then there follows an almost explosive action, lasting 150 to 300 milliseconds (in sand -- and somewhat longer for clay) thereby forming an "initial crater". High speed motion pictures show soil being lifted into a bubble, or cake-like structure and then being thrown out to form the crater. For a 600 pound thrust level, this initial crater may be 40 inches or more in diameter and 20 inches deep.

(c) After the initial crater is formed, its diameter changes very little with time, and the depth increases much more slowly. Although the initial crater forms in about 300 milliseconds, typically, it may require 5 seconds to double the initial depth.

The whole cratering action is accompanied by the shooting of a geyser of soil more than 40 feet into the air, and the velocities of the particles near the crater have been estimated to be in excess of 60 ft/sec.

It is believed that the cratering action may be due to simultaneous, and consecutive action of several effects:

(a) The overloading and rupturing of the soil, as its shear strength is exceeded, to produce a momentary cavity. The impingement surface is then no longer a plane but a deep cup, and the pressure distribution is altered drastically.

(3) Land, Norman & Clark, Leonard V.: Investigation of Jet Impingement of Surfaces of Fine Particles in a Vacuum Environment, NASA TN D-2633.

(4) Stitt, Leonard V.: Interaction of Highly Under-Expanded Jets with Simulated Lunar Surfaces, NASA TN D-1095.

(b) The pressures on the interior surfaces, act laterally and upwardly and "blow out" the surrounding soil.

(c) In coarse or porous soils an internal pressurization also contributes to the "blow out". That is, gas enters and spreads through the pores for some distance. This latter effect is important where many veins and fissures exist in an otherwise compact soil.

(d) The "blow out" again changes the pressure distribution, vents the surrounding space and drops the stresses on lateral surfaces to very low values, so that there is relatively little more "widening" action. Entrainment of surface particles is present, to a greater or less degree, throughout the whole action.

(e) A mathematical model which describes the detailed mechanisms of the cratering action is presented in Section V. This model appears to be basically valid for the conditions studied in the program. Section VII enumerates an "engineering tool" which can be used to predict jet cratering action.

III. DETAILED DATA AND OBSERVATIONS

1.0 Detailed results of the test program are presented here along with certain observations and comments concerning the specific tests.

1.1 Pressure Distribution on Surfaces: In order to evaluate the cratering action it was necessary to know the pressure distribution on the ground surface. Preliminary literature surveys indicated that data for jets of the type used in the Honest John spin rocket was quite limited, and therefore it was necessary to perform tests at Hayes to determine this quantity.

A flat aluminum plate was fitted with a number of pressure sensing orifices extending in three directions from a central orifice. This orifice plate was mounted rigidly and was carefully positioned directly below the jet.

All tests were conducted under ambient atmospheric pressures and temperatures.

After determining that the pressure distribution was sensibly symmetrical, the jet was fired at several different chamber pressures, and this procedure was repeated for several heights of the nozzle above the plate, making a

total of over 40 shots. However, only a limited number of curves are presented here to show the typical forms.

Figures 3 through 5 show the pressure distribution curves for the Honest John nozzle-exit radius 0.44 inch and perfectly expanded at sea level for a chamber pressure of 271 psia.

A second nozzle having the same exit orifice, but having a perfect expansion for a 1500 psia chamber pressure, also was tested. The "1500 psia" nozzle data is shown in Figures 6 through 8.

In addition to the measurements of pressure distribution on a flat surface, it was felt that a knowledge of the distribution on a deeply concave surface would be very helpful in understanding the action of the jet in craters.

The concave aluminum surface (Figure 9) is virtually parabolic at the lower extremity, and then fares into a cylindrical section in the upper part. The vessel is 18 inches deep over-all, and some 12 inches in diameter at the cylindrical open end.

The pressure distributions on the surface of this "ogive" vessel, for the nozzles described above, are shown in Figures 10 through 13.

It is worthy of note that the pressure distributions on the concave surface are more uniform and symmetrical than those on the flat plate.

2.0 Cold Gas Static Tests

The test apparatus is illustrated in Figure 1. Basically it consisted of a pressure vessel and suitable controls mounted on a heavy trailer. The system supplied gas at controlled pressure to a nozzle mounted at the end of an outrigger line extending laterally from the trailer.

The gas flow (nitrogen) was controlled by a line regulator which could be pre-set at any pressure from tank pressure to nearly zero.

The trailer mount facilitated the making of moving jet tests and also made it possible to transport the whole system to field test sites.

An electrically actuated ball valve was mounted in the line between the regulator and the nozzle. A pressure sensor measured the pressure at the nozzle chamber and transmitted a signal to a remote recorder.

An automatic timer switch was arranged to make and break the circuit to the ball valve in accord with preset values.

The gas supply line extended horizontally from the pressure supply for about seven feet and then turned vertically downward to the nozzle. The vertical section had several joints so it was possible to vary the height of the nozzle quite easily.

For stationary firing and especially for pressure distribution measurements the horizontal section of the supply line was anchored by guys to the ground,otherwise the reaction caused the jet to shift 3 to 5 degrees.

The tests in sand and some of the clay tests, were made on soil samples contained in large wooden bins - about 30 inches deep and 6 x 10 feet in plan dimensions. However most of the tests in clay and in sod were made at field sites where the soil had been undisturbed for several years.

The tank was normally pressurized to 3000 psi but for field tests the original pressure was as high as 4000 psi. This was sufficient for 15 to 25 shots depending on the time duration of the shots and the chamber pressures at which they were made.

As each shot was made, the average dimensions of the crater were measured and recorded.

2.1 Sand: Figures 14 through 16 show typical contours of craters in sand for various chamber pressures, heights, and times.

Most of the deeper craters show effects of slumping and "fall in". The craters made at low pressures have a shallow dish shape. However, the craters formed at high pressure usually have a sharp downward cusp at the center.

2.2 Clay: The craters in clay vary even more widely, due principally to nonhomogeneity of the soil. In some instances a relatively small clear hole goes down two feet or more and from this, gas spreads laterally to break up the surrounding ground into large chunks so that no clearly defined crater is formed. This occurs in soils where there are subsurface faults which permit dissipation of the jet gases. For field clays which are homogeneous laterally, but which possess a hard surface layer for several inches and soft clay underneath, a wide mouth crater is formed which narrows to a steep apex a foot or two from the surface.

In other places where the clay is relatively homogeneous, "good" craters are formed. They appear much like the ones found in damp sand. Two such clay craters are shown in Figure 17.

The size and shape of craters in clay varies widely due to moisture content and distribution, and due to stratification where hard dense strata are mingled with softer porous material.

2.3 Oblique Incidence: Although this was not a specified contractual objective a series of shots was made with the jet inclined at angles up to 40 degrees with the vertical, in order tentatively to evaluate the effects of oblique incidence.

Typical crater shapes are shown in Figures 18 through 20.

It is seen that they are slightly oval -- elongated in the direction which included the firing angle. However, in sand, the over-all crater dimensions are essentially the same as those made with the jet at normal incidence. The ratio of major to minor diameters (1.25) was no greater than some of the variations in the latter craters.

Noteworthy factors are:

(a) The deepest point does not coincide with the aiming-point-after-excavation. It was more nearly directly under the aiming point on the undisturbed flat surface.

(b) For the 40 degree angle, (Figure 20) a distinct channel-like depression was left, as shown, along the projection of the line of action of the jet. This could have been caused by the same action which leaves the downward "cusps" at the bottom of normal craters.

3.0 Cold Gas Moving Jet Tests: The effect of a moving jet was found by pulling the jet trailer past the sand bins and field clay,at various speeds and with the nozzle at various heights. The speed was determined by measuring the time required for the 25 foot trailer to pass a fixed sighting point.

3.1 Sand: The cratering, or trenching action, in sand, by a horizontally moving jet, shows characteristics generally similar to those of a stationary jet in the same material. However, inasmuch as the time of impingement on a given area by a jet moving 10 to 25 feet a second is considerably less than the times used for a stationary jet, the over-all crater dimensions are smaller. Two distinct types of action were observed. For the lower surface pressure velocity products, the trench left by the moving jet was softly rounded as shown at B of Figure 21. At higher pressures, however, the trench had vertical sides and slump lines were observed paralleling the trench on both sides.

For the moving jet, in sand, the explosion-like action observed with stationary jets causes a "bow wave", perhaps a foot or so high, to accompany the

jet. This is then followed by a "rooster tail" explosive geyser of sand which rises many feet diagonally upward and to the rear. At higher horizontal speeds of the jet, the impingement point moves forward until it coincides with the leading edge of the "bow wave". However, the following rooster tail seems little affected by the increase in speed.

The high pressure trench was also characterized by considerable "fill in".

Figures 22 and 23 show measured contours of trench cross sections.

The width of the trench varies slightly with the jet's horizontal velocity while the depth variation is more pronounced (Figure 24).

It should be noted that for the tests of a moving jet in sand, the valve was opened and the jet stabilized a full second or two before the jet was carried over the sand bin. Thus, the effect of a changing jet pressure was not observed in these tests. This procedure contrasted with that of jets over clay which were conducted in the field where, by necessity, the pressure was allowed to build up and shut down while the jet was at the controlled horizontal speed. Thus, in the sand tests the mode of jet pressure applications, together with the porosity of sand and the short paths possible, acted to diminish any blow out and ditching pattern which was observed in the traces in sod and clay. Figure 24 shows the relation between crater dimensions, horizontal velocity and height of nozzle.

3.2 Clay: The same cold gas and trailer mount shown in Figure 1 was used to conduct these moving jet tests. The tests were conducted at the same location as the stationary tests. At the time these tests were conducted the area possessed a substantial sod cover. The results of the tests are best understood by referring to the drawings of Figures 25 through 27. These outlines are approximately to scale. The "blow out" and trenching effect is immediately evident.

It should also be noted that the width and depth of the traces vary but slightly with the horizontal speed - - as with sand. Cross-hatched areas represent broken and lifted, but not expelled, terrain.

In general, the traces begin and end with narrow and shallow sections due to the buildup and dying out of the pressure. Maximum pressure is attained 0.4 to 0.7 second after the beginning of the discharge, at the left, in each instance.

The variation in the character of the soil and sod, even over distances as short as 20 feet, makes it difficult to distinguish the effects which are strictly due to the horizontal motion. However, the alternate wide and narrow trench sections were also noted in the Hot Gas tests to be described, although in the case of the latter, only one showed more than a single blow-out before the terminal crater.

3.3 Comparison of Clay and Sand Trenches: The tests of moving jets on heavy natural sodded soils showed one characteristic distinctly different from that observed in loose sand. This is alternate wide craters connected by narrow ditches. Some of the effect is due to varying soil characteristics at various positions along the jet's path. However, there may also be the effect of a "blow out" occurring whenever the impingement point is surrounded too closely by "walls". This blow out then vents the path and allows excess pressure to discharge back along the path until another soft area is encountered where the thrust of the jet makes an unusually deep penetration, thus forming a cup.

This periodic blowout and channeling was observed both in tests by the cold jet and by the hot jet when the soil was heavy sod and clay.

4.0 Hot Firing Tests: The tests were conducted with the configuration diagramatically illustrated in Figure 2.

The tests were made over three types of terrain: (a) deep sand pits, (b) undisturbed sod, and (c) scalped clay-silt. Three different angles of approach were used for each soil -- approximately 70 degrees; 54 degrees, and 41 degrees with the horizontal. The rocket was fired as it passed the contactor stand some 6-1/2 feet above the soil surface. The vertical velocity was approximately 27 ft/sec in each case and the horizontal velocity varied with angle of approach - nominally 10, 20 and 30 ft/sec for the 70 degrees, 54 degrees and 41 degrees angles respectively.

Motion pictures were made at both 24 and 84 frames per second. Knowing the camera frame speed and referring to a background grid, it was possible to trace the trajectory of the rocket carriage and to measure its horizontal and vertical speed.

4.1 Test Results: The test results are briefly summarized in Figure 28 in terms of the maximum trench depth and width.

Figure 29 is a photo of the carriage at the moment of firing (which lasted approximately .3 second).

Figure 30 is a photo of the trench made in sand for a horizontal component of approximately 20 ft/sec. (a bit of the background grid shows at the extreme left.

Figure 31 shows the crater produced in sand while the rocket was held stationary.

Figure 32 shows the shallower trench left in the sod terrain. (Due to lack of perspective and color contrasts the photo does not accurately portray the actual interior dimensions very satisfactorily).

In sand, the resulting trenches were long ovals approximately 28 inches wide at the top and 11 to 16 inches deep. The trench depth increased more or less linearly from zero to the maximum depth which occurred at the end of travel. The lateral cross section was a wide "V" in contour.

The sand trench contours and general dimensions are essentially similar to those obtained in the many tests conducted earlier in the program with cold gas, and at a thrust level comparable to the rocket thrust.

The stationary shot which was fired into the sand produced a crater which compared very well with those of the cold gas tests at the same thrust level. The hot gas crater diameter was 43 inches, -- cold gas diameter 42 inches -- while the hot gas depth was 14 inches and cold gas depth was 18 inches.

In general, the variation of the hot test and cold test results for sand (both moving and stationary) was within the scatter of the cold test data. We can, therefore, conclude that the gas temperature condition is not significant in crater formation.

The trenches produced in sod and earth however had distinctly different characteristics from those in sand, apart from the different dimensions. The sod and earth trench contours are illustrated in Figures 33 and 34.

The cratering begins within a horizontal distance of 4 feet from the ignition point and while the rocket nozzle is 4 feet above the ground surface. The crater grows wider and deeper as the rocket moves forward, for 2-1/2 to 3 feet further. Then, there occurs a wider and slightly deeper area which we have called the "blow out" area. This is followed by a narrow trench of about 1/3 the width but having essentially the same depth. This continues until the carriage comes to rest. Here, a somewhat wider crater begins to form as the thrust decays.

4.2 Trajectories of the Rocket Carriage: Figures 35 through 37 are graphs of the carriage paths obtained from the motion pictures. (The paths of two points on the carriage are plotted since one is often prematurely obscured by dust and smoke). The graphs were made from the 84 frame/sec. motion picture film. The time between data points is .0119 second. It is seen that about 60 milliseconds elapse after the igniter fires and before the carriage begins to depart from its straight-line path. This time is required for the chamber pressure to come up to its normal thrust value.

5.0 Soil Shear Tests: Since the characteristics of the soil determine to a large extent the shape and dimensions of the craters measurements were made to determine the shear strength of sand and the field earth.

For the sand measurements the basic apparatus was arranged as in Figure 38. An open frame 18 inches square and 4 inches high was placed on the sand surface in a test bin. Two rails embedded in the sand assisted in maintaining a horizontal motion. The frame was filled with sand and gently tamped so that the sand in the frame and that in the bin were essentially a unit. The shear force was measured with a spring dynamometer.

The maximum shear force necessary to pull the frame occurred suddenly as the sand formation "broke". This shear force also varied with the load placed on the load plate shown in the figure. A plot of yield stress versus normal load is shown in Figure 39. The shear stress varied linearly with the normal stress with a slope of 0.584. Using the Coulomb relation $\tau = c + \sigma \tan \phi$, the above slope would indicate a value of $\phi = 30.2$ degrees which is a typical value for sand.

The properties of clay are quite sensitive to the moisture content, and consistent readings have been difficult to obtain. Observed values range from 0.4 lbs/in^2 in wet loose clay to 1.6 lbs/in^2 in specimens which had been packed and allowed to dry for more than one week. The internal friction angle varied from specimen to specimen, but was never greater than 10 degrees due to air content. (See page 32 for discussion).

The shear strength of the earth soil at the Hot Test Site was measured in situ on undisturbed, nearby areas (see Figure 40).

The unloaded shear strength was 1.13 psi and this increased to 1.33 psi for normal loads of 1.2 psi, giving an internal friction angle $\phi = 9$ degrees for this soil.

A sample of the soil was also sent to a soil testing laboratory for analysis of composition and moisture content. The results are summarized in Figure 41.

6.0 General Observations and Remarks:

The high pressure storage tank used in the test could safely be pressurized to 4000 psi. Such a charge provided a full half-day of testing in the field without recharging.

The trailer mount permits both the horizontal movement of the jet while it is being fired, and the easy transportation to field locations. This feature has proven to be very valuable in the tests of field clays.

A line pressure regulator and an electrically operated ball valve serve to feed gas to the nozzle chamber. The feed tube extends laterally and down from the trailer. The nozzle itself is mounted at the end of a vertical

section of the tube so that by using extension sections of various lengths, the nozzle may be positioned at a number of heights above the test surface.

Several factors tended to mask and confuse the effects which produce the crater. Chief of these is the tendency for the soil to slump and to fall back when pressurization ceases. Stable configurations during firing are not stable when the firing stops.

This "fall back" effect is especially troublesome at crater depths greater than 12 to 16 inches. It is quite random and while it usually begins at depths of about a foot, ocassionally craters 22 inches deep with nearly straight sides and a diameter of 30 inches have been observed in damp sand (water content 6-7 percent).

Also, since much of the material thrown out often falls back into the excavation, the final appearance of the crater is affected by the angle of repose of the particular sand.

The cohesive properties of sand are greatly affected by the presence of moisture. Even water contents of less than 1 percent are effective in changing the coherence of sand.

In the case of wet clay, the slumping and fall back will proceed very slowly and may continue for several minutes after the jet has been shut off. However, for dryer clay there is little, if any, slumping - the crater walls remaining sharply sculptured. It may be pointed out that the strength properties of clay are directly related to its water content.

Another factor which makes it difficult to control accurately the experimental conditions is that of obtaining a rapid rise and fall of pressure in the cold gas jet. This is due to limitations of the valve which controls the gas flow and its location several feet from the nozzle. Moving the valve nearer to the nozzle would aid response time, but would also increase the danger of soil particles entering and damaging the precise valve mechanism.

In view of these facts and the widely varying characteristics of real soils, it is not surprising that the data is somewhat scattered. However, the results are of sufficient accuracy to permit engineering determination of the cratering mechanism to be made.

IV. DATA REDUCTION

1.0 Ground Force: The total force on the ground and the surface pressure distribution are the most basic causative parameters in crater formation, exclusive of the soil properties. Therefore it was necessary to evaluate these quantities as functions of nozzle height and chamber pressure. The total force was obtained

by integrating the product of pressure at a given point and the element of area on which the pressure was applied. For this purpose, the pressure distribution plots of III, 1.1, were divided into elementary rings and the area of each ring multiplied by the average pressure existing at that location. Then, these products were summed over the whole impingement area.

The pressure distribution parameter a was taken to be the radius at which the surface pressure had fallen to 5 percent of its peak value. The data is presented in Figures 42, 43 and 44. Figure 42 is a dimensionless plot of a/r_{ne} as a function of h/r_{ne} where a is as defined above, h is the nozzle height above the ground and r_{ne} is the nozzle exit radius. Figure 43 is a plot of the average surface pressure $\overline{P} = T/\pi a^2$ divided by the chamber pressure as a function of h/r_{ne}. The value of $\overline{P}/P_c$ varied markedly with height of the nozzle and with the general range of P_c. But the most remarkable fact is that $\overline{P}/P_c$ apparently varies cyclically with nozzle height.

It will be noticed that the median values of each curve slopes with nozzle height, and that the lower the pressure range, the greater is the slope.

Some attempt has been made to correlate the cyclic function with the "wavelength" of the Mach diamonds, but so far this has not been explored extensively. If the points had not fallen so nicely on the oscillatory curves the departure from the constant slopes would have been charged to data scatter.

The values of $\overline{P}/P_c$ obtained from integrating the vertical forces in the concave surface are also plotted in Figure 43.

The "height" of the nozzle is taken as the distance to the concave surface.

It will be noticed that in the case of the pressure on a concave surface the $\overline{P}/P_c$ for the higher chamber pressures is actually a little lower than that for the lower chamber pressures. This is likely due to random errors.

2.0 Sand Craters: Figure 44 is a plot of sand crater Radius/a versus $\overline{P}$. Figure 45 shows a plot of the Depth/a of the sand craters $\overline{P}$.

3.0 Clay Craters: As was mentioned previously, the data from firing into clay varies quite a bit, due to variations in the clay properties. Figures 46 and 47 represent data taken in an area behind the Birmingham Airport which had the most consistent and homogeneous soil readily available for testing. Figure 46 is a plot of crater Radius/a versus $\overline{P}$ while Figure 47 shows the Depth/a as a function of $\overline{P}$.

4.0 High Speed Camera Studies: A series of high speed motion pictures have been taken of the cratering action both in sand and clay. These movies were taken with a Fastax camera at a framing rate of approximately 1000 frames/second. These high speed pictures clearly illustrated that the material is lifted up in a cake-like structure which blows out to form the crater. Selected frames from the high speed movies are reproduced in Figure 48. The sand shot clearly shows the domed structure with a fracture surface along a line which later becomes the crater circumference. Perpendicular to this line are smaller fracture lines.

The clay shot also illustrates a lifting up of the soil material and the formation of fracture lines. Due to inhomogeneities, the symmetry of the clay shot was not as "clean" as the sand.

5.0 Hot Firing Tests: For sand, the hot test and cold test data compare quite well. The stationary sand crater dimensions for the hot and cold tests are essentially the same within the scatter of the cold test data. In the moving rocket tests a trench of uniform width and depth is formed whose dimensions compare quite well with those of the trenches produced in the cold gas moving tests. (Remember that in the hot tests the nozzle height was not constant due to the vertical velocity component.) As a rough rule of thumb it has been found that the stationary crater width (or diameter) is reduced by a factor of approximately 0.67 and the depth by a factor of approximately 0.5 by a moving source in the velocity range studied.

In the rocket tests with earth and sod specimens a new phenomenon has been observed. In these tests a large oblate area was formed near the point where the motor reached full thrust. This area then narrowed down to a trench whose width was between 1/3 and 1/2 that of the oblate region. The depth was approximately 2/3 that of the oblate region.

The ratios of the dimensions of the oblate region to the stationary crater dimensions correspond rather well to the dimension ratios for the sand trenches, i.e., the width is approximately 0.67 the stationary crater diameter and the depth approximately 0.5 the stationary crater depth which would be predicted by the theory presented in the Mid-Project Report[5]. For example, refer to Figure 24. The average maximum oblate region width is 17 inches and the depth 6 inches for earth. The soil yield stress was found to be 1.1 lbs/in^2. For a rocket thrust of 650 pounds the stationary crater depth would be 11.5 inches and the diameter (or width) would be 28.6 inches. Using the factors 0.67 for width and 0.5 for depth, we obtain the dimensions of 19 inches and 5.8 inches for the oblate region width and depth respectively.

It was originally thought that the characteristic shape of the trenches in earth and sod -that of a widened area followed by a narrow trench was due to pitching and yawing of the rocket. However, careful examination of the motion

(5) "Soil Erosion by Landing Rockets," Contract NAS9-4825, Mid-Project Report 28 Feb. 1966

pictures shows this is not the answer. Moreover the pictures do show an upward vector of soil shooting up through the dust and smoke of the early erosion action, at an angle of 30-40 degrees from the point of maximum width of the trench and continuing long after the rocket has passed over this point.

V. THEORETICAL PREDICTION OF CRATER FORMATION

1.0 General: The experimental data obtained from the static tests conducted on sand and clay specimens indicate that, in the moderate-to-high thrust region the crater is formed in two distinct steps: The first is an explositive-type phenomenon in which a conical crater forms in the region about the jet, the surface diameter of the cone corresponding to the final diameter of the crater. The entire mass of material is lifted and then breaks up into smaller segments which are "blown out". This process occurs in a relatively short time (on the order of 100 - 200 milliseconds). The second step is a subsequent digging action in which the depth increases but the radius remains essentially unchanged. This latter process is extremely slow compared with the explosive action. Along with these processes, there is also an erosive action in which the loose material is removed from the surface of the ground by entrainment.

The following model will attempt to explain the initial process which essentially determines the final crater radius and the "short time" crater depth. The process is basically a failure of the soil material in shear due to stresses induced by the applied thrust load and as such depends only on the magnitude and surface distribution of these loads and the yield shearing stress of the particular soil. Also, pressure gradients induced in the soil by diffusion of the jet gases augment the effect in porous soil media and can be significant in these materials.

It must be emphasized that the model proposed pertains to a quasi-static phenomena in which the internal stresses compatible with the surface loading are instantaneously reached. This simplification can be justified since the linear dimensions of the craters are on the order of a few feet and the velocity of propagation of stress waves in typical soils is in excess of 5,000 ft/sec. Thus, in the region of interest, the steady-state stresses are reached in times on the order of a small fraction of a millisecond.

It is assumed that after the failure occurs the material inside the failure contour is removed from the crater by internal pressures and also by erosive and/or entrainment action. This will take place relatively rapidly for sand. For clay, which breaks into large clods, the removal action proceeds at a lower rate. However, the initial failure process will occur very quickly in each case.

2.0 Simulation of Jet or Rocket Cratering By Projectile Penetration: A jet or rocket directed at and normal to a soil surface gives rise to radially symmetric normal and shearing stress distributions over the surface. When the soil medium is permeable, there will be a time-dependent diffusion of the hydrostatic pressure into the soil until eventually a steady state of pore pressure distribution is reached. At the same time soil movements will occur. For jet thrust levels which are low in relation to the strength and grain size properties of the soil, the principal mechanism of grain movement is erosion resulting from the shearing stresses caused by the jet at the surface.

However, for a given soil and jet, a thrust level exists at which the gas pressures at and below the soil surface exceed the bearing capacity of the material. Above this thrust the jet develops a hole in the soil relatively rapidly, and this is followed by an explosive cratering event. The crater developed changes only relatively slowly in time thereafter, principally by erosion. The form of the crater is maintained by the combination of the gas flow and soil properties. When the jet is cut off, the crater shape changes due to the change in boundary conditions and the resulting diffusion of pore pressure out through the surface under the new boundary pressure conditions.

Changes in pore pressure will always occur in the granular medium as a result of the presence of the jet, but the relation of the time associated with the pore pressure variation to the time involved in the cratering event depends on the permeability of the soil medium. In a water-saturated fine-grained soil like clay, the pore pressure changes will be negligible for jet firing conditions of seconds to minutes. On the other hand, the pore air pressure in a dry, medium to coarse, sand probably changes sufficiently rapidly to play a significant part in the cratering process.

A saturated clay soil exhibits very cohesive properties during a test of the typical duration of a jet firing and consequently, with the absence of transient pore pressure consideration, the thrust level at which cratering will commence can be calculated.

2.1 Explosive Cratering: It is assumed for the following analysis that the effect of the radial shear stresses caused by the gas flow over the surface can be neglected and that the jet effect can be represented by a normal pressure distribution over a circular area at the surface.

In this case, the bearing capacity of the cohesive soil is given by the relation

$$T = \pi a^2 N_c c \qquad (1)$$

where N_c is a constant with the approximate value of 5, a is the radius of the circular area and c is the cohesive strength of the soil. Cratering will commence when the thrust exceeds this value of T, or when

$$\frac{T}{\pi a^2 c} = \frac{\bar{P}}{c} > N_c \approx 5 \qquad (2)$$

(Refer to further discussion in Section VI, page 32).

where $\bar{P} = T/\pi a^2$ is the average pressure on the loaded area.

In deep sands, the cratering event depends on the development of the pore pressure in the soil, and consequently a cratering criterion must contain the soil's permeability and include the time-dependent diffusion process.

2.2 Cratering Depth: It is possible to view the cratering mechanism of the jet as being analogous to the penetration of a cylindrical projectile into the soil. The crater depth is given by the maximum penetration of the projectile. For this analogous situation, the diameter of the projectile will be taken to be the effective diameter of the jet pressure at the surface, and the weight of the projectile is taken equal to the jet thrust. Since the jet static pressure distribution at the soil surface generally falls off from a maximum value at the intersection of the axis of the jet, it is considered that a cylindrical projectile with a conical nose (vertex angle 90°) gives a more suitable representation of the jet behavior. The projectile length may be taken to be equal to its diameter, although this is not an important consideration.

Consequently, it is desired to predict the penetration of this projectile into a soil of selected properties under an appropriate value of gravity, with an initial projectile velocity of zero.

There are two parts to the motion: those during and after the cone penetration.

(1) During Cone Penetration

The relevant parameters are shown on Figure 49, which also indicates the mechanism of deformation of the material around the tip of the cone. The equation of motion of the projectile is obtained by equating the change of momentum of the projectile and moving soil at a particular depth to the weight of the projectile less the resistance offered by the soil. It is assumed that the soil resistance can be calculated to be that which would be offered to the static penetration of an object of the effective cone diameter at the soil surface. The soil's shearing resistance is then considered to be developed as a succession of static plastic states.

The weight of the projectile is given by mg, which is made equal to the thrust of the jet; however, this is reduced by the weight of the soil in the

annular region (1) (see Figure 49) which is equal to $\pi \rho g\ z^3/3$. The soil resistance is given by the usual approximate static soil mechanics [6] relation, of which Eq. (1) is a special case.

$$F = \pi z^2 N_c c + \pi z^3 N_\gamma \rho g \tag{3}$$

where ρ is the soil's density, z enters because the cone angle is taken to be 90° and N_c and N_γ are coefficients dependent upon the angle of friction of the soil.

Equating the projectile and soil weights and the soil resistance from Eq. (3) to the change of momentum of soil and projectile at depth z, and making the result dimensionless by dividing throughout by $\rho g a^3$ gives the equation in a convenient form

$$\frac{d(V^2)}{dZ} + \frac{6dZ^2 V^2}{e + dZ^3} = \frac{2(e - gZ^2 - hZ^3)}{e + dZ^3} \tag{4}$$

in which

$d = 5.48$ (a geometrical constant)

$e = M = \dfrac{m}{\rho a^3}$

$g = N_c B$ (not gravity)

$h = \pi/3 + \pi N_\gamma$

$B = c/\rho ga$

$V = v/\sqrt{ga}$

$Z = z/a$

and v is the velocity.

The term in V^2 arises through the inertial resistance of the soil. The solution to Eq. (4) is

$$V^2 = \frac{1}{(e + dZ^3)^2} \left[e^2 V_i^2 + 2e^2 Z - \frac{2eg}{3} Z^3 + \left(ed - eh\right) Z^4/2 - dg Z^6/3 - 2dhZ^7/7 \right] \tag{5}$$

and in this case, the initial velocity V_i is to be taken equal to zero.

(2) Cone Penetration Complete

Figure 49 shows the mechanism of deformation after complete penetration of the cone into the soil. In this stage of motion the mass of moving soil

(6) Scott, R. F., "Principles of Soil Mechanics", Chap. 9, Addison-Wesley, Reading, Mass., 1963

is varying linearly with depth rather than with the third power of depth as with cone penetration. Also, an annular mass of soil is moving upward and its weight opposes the motion.

At this stage, the static shearing resistance of the soil to the movement of the projectile is given by the equation

$$f = \pi a^2 N_c c + \pi a^2 N_\gamma \rho ga + \pi a^2 N_q \rho g(z-a) + 6\pi a(z-a) c + 3\pi K_o \rho ga(z-a)^2 \tan \phi \quad (6)$$

in which, on the right-hand side, the first two terms are the same as those of the right-hand side of Eq. (3), but in which the radius a replaces the radius z of Eq. (3). The third term arises because the projectile has to overcome the shearing resistance caused by the depth (z - a) of the base of the cylindrical portion below the ground surface, and the fourth and fifth terms represent the cohesive and frictional shearing resistance of the soil along the periphery of the region (2) in Figure 49. In Eq. (6) N_q and K_o are coefficients related to the angle of internal friction of the soil, the latter is usually taken equal to 0.5.

In addition, the motion is assisted by the weight of the projectile mg, as before, and resisted by the weight of the moving regions of soil (1) (2) in Figure 49. The height of the region (2) above the original surface is given by the requirement that the volume of this portion is equal to the volume of the cavity formed by the projectile. With this condition, the gravitational forces assisting penetration are equal to $mg - \rho ga^3$.

Taking the change in momentum to be equal to the sum of the gravitational terms and the soil's shearing resistance and making the resulting equation of motion dimensionless as before by dividing throughout by ρga^3. gives the equation of motion

$$\frac{dV^2}{dZ} + \frac{2qV^2}{P + qZ} = \frac{2(r - sZ - tZ^2)}{P + qZ} \quad (7)$$

where

$$p = M + 2.04$$

$$q = 3.5$$

$$r = M + 27.25 - B(\pi N_c - 6\pi) - \pi N_\gamma + \pi N_q - 3\pi K_o \tan \phi$$

$$s = 6\pi B + \pi N_q - 6\pi K_o \tan\phi + 9\pi$$

$$t = 3\pi K_o \tan \phi$$

K_o, N_q = coefficients depending on angle of internal friction of soil; K_o usually equal to 0.5[6].

The solution to Eq. (7) is

$$V^2 = \frac{1}{(p + qZ)^2} \left[2p\,rZ + (qr - p\,s)\,Z^2 - \frac{2(qs + p\,r)}{3} Z^3 - \frac{qt}{2} Z^4 + u \right] \qquad (8)$$

where u has to be obtained from the initial condition that V is given by V in Eq. (5) at the depth $z = a(Z = 1)$.

Equations (6) and (8) can then be used to give the motion of the projectile during penetration and, in particular, the maximum depth of penetration.

2.3 Effects of Pore Pressure: In a cohesionless soil (sand)it is expected that the results will be influenced by pore air pressure effects generated by the jet. These tend, by increasing the pore pressure, to decrease the effective strength of the soil. Consequently, a solution for the maximum depth of penetration of a projectile in a cohesionless soil based on Eqs. (5) and (8) will give penetration depths in general smaller than those observed experimentally. The pore pressure effect can be accounted for approximately in the projectile analogy as follows.

The strength τ of a cohesionless soil, as used in the bearing capacity equations of the preceding section is given by the Coulomb equation

$$\tau = \bar{\sigma} \tan \phi \qquad (9)$$

where $\bar{\sigma}$ is the so-called effective normal stress acting across a shear surface in the soil and ϕ is the angle of internal friction of the material. Terzaghi's effective stress hypothesis (Reference 6, pp. 270-272) is that

$$\bar{\sigma} = \sigma_n - p \qquad (10)$$

where σ_n is the total normal stress and p is the hydrostatic pore pressure. Thus, Eq. (9) becomes

$$\tau = (\sigma - p) \tan \phi \qquad (11)$$

which may be written alternatively as

$$\tau = - p \tan \phi + \sigma \tan \phi \qquad (12)$$

However, the general equation for the strength of a soil with both cohesive and frictional properties and on which the general bearing capacity equations are based, is

$$\tau = c + \sigma \tan \phi \qquad (13)$$

The value of c in Eqs. (5) and (8) is obtained from Eq. (13) applied to soil shearing test results. Consequently, comparing Eqs. (12) and (13) it can be seen that if we place in Eqs. (5) and (8) a value of c equal to $-p \tan \phi$ we will get a depth of penetration modified by a pore pressure p. Naturally, this value of c cannot be greater (negatively) than $\sigma \tan \phi$.

A method of calculating the pore pressure p to use in the calculation of an equivalent c for a cohesionless soil with pore pressure effects is given in Section 3.

3.0 Pressure Buildup in Soil: In a highly porous soil or in one possessing many fissures or cracks, pressure buildup will substantially effect the cratering process. A sophisticated treatment of this phenomena is extremely complicated and was beyond the scope of the present program. However, the following approximate analysis will be indicative of the importance of this factor in certain soil conditions.

3.1 Soil Pressurization Model: The soil is assumed to possess a large number of small tubes or capillaries per unit of surface area as illustrated in Figure 50. The diameters of the capillaries are so small that viscous flow can be assumed to exist in all cases. The gas flow is governed by the Stokes-Navier equations and by the equation of continuity and is extremely complex. To simplify the analysis it was assumed that the gas flow in the soil is laminar, and the steady-state flow conditions have been reached.

The steady-state flow assumption is questionable during crater formation, but should give an upper limit on the pressure forces. To account for the time-dependent flow would require integration of a non-linear partial differential equation and as such, was not feasible. Laminar flow should be expected some distance in the soil from the jet.

With these assumptions, the flow in a section of a capillary of length Δl (see Figure 50) is given by Poiseuille's formula[7] which may be expressed as

$$\underline{v} \approx \frac{\nabla p d^2}{\eta} \tag{14}$$

where $\underline{v}$ = flow velocity vector

∇p = pressure gradient

η = coefficient of viscosity

d = capillary diameter

(7) Joos, G., "Theoretical Physics", p. 203, Hafner Publishing Co., N. Y.

For steady-state conditions, the equation of continuity, which states that the amount of fluid leaving an element of volume equals that going in plus that created in the volume element, gives

$$\nabla \cdot (\rho \underline{v}) = 0 \tag{15}$$

where ρ = gas density

If we assume that the gas expansion in the soil is isothermal, we have $p \sim \rho$. Combining Eqs. (14) and (15) gives

$$\nabla \cdot (p \nabla p) = 0 \tag{16}$$

or

$$\nabla^2 (p^2) = 0 \tag{17}$$

where ∇^2 is the Laplacian operator.

3.2 Solution of Pressure Eqs.: The steady-state pressure in the soil resulting from diffusion is given by Eq. (17) which is Laplace's equation in p^2. To solve this equation, we will assume that the flow is azimuthally symmetric and that the pressure source on the ground surface (the jet impingement point) is a mathematical point. As in the case of stress distribution, a point source approximation enormously simplifies the solution and is valid at distances greater than three times the loaded radius.

The boundary condition which must be met is that the pressure is equal to p_∞, the ambient atmospheric pressure, at large distances from the impingement point.

A solution to Eq. (17) which meets these conditions is

$$p = p_\infty \sqrt{1 + B \frac{\cos \theta}{R^2}} \tag{18}$$

where R = radius vector from impingement point

θ = angle with respect to normal-to-ground surface

B = constant related to jet strength

To evaluate B we will require that the integral of the soil overpressure $p - p_\infty$, over a hemispherical surface in the soil whose radius R_o is large compared with the crater dimension, be equal to a specified fraction f of the

total thrust, i. e. ,

$$\int_S (p - p_\infty)\, dA = fT \tag{19}$$

Over the hemispherical surface $dA = 2\pi R_o^2 \sin\theta\, d\theta$, and θ goes from $0 - \pi/2$. Assuming R_o large we obtain $B = 2fT/\pi p_\infty$ and thus,

$$p = p_\infty \sqrt{1 + \frac{2fT}{\pi p_\infty} \frac{\cos\theta}{R^2}} \tag{20}$$

At large distances from the jet (large R) Eq. (20) can be simplified by expanding the radical and keeping the first two terms to give

$$p = p_\infty + \frac{fT}{\pi} \frac{\cos\theta}{R^2} + \ldots \tag{21}$$

For a point directly under the jet $\cos\theta = 1$ and $R = Z$ so that

$$p - p_\infty = \frac{fT}{\pi Z^2} \tag{22}$$

Equation (22) has been used to estimate the soil pore pressure for the cratering calculations.

The quantity f is an empirical term whose value lies between zero and unity and is a measure of the correctness of the steady-state approximation. For highly porous soils such as sand where the steady-state condition is quickly reached f will assume a value on the order of unity. For compact soils such as wet clay, f will be quite small since the amount of diffusion occurring in times comparable to the jet action time will be negligible.

It must be emphasized again that this diffusion model is quite crude and can be used only as an estimate of the soil pressure. It does not account for the time rate of change of the flow conditions of the soil or the change in the ground surface contour during crater formation. However, for highly porous sand where the steady-state conditions may be reached quickly before a large amount of crater material has been ejected, the model should give somewhat reasonable results.

4. 0 Crater Radius: The penetration model presented in Section 2 of the theoretical analysis which has been used to predict the crater depth does not yield an expression for the crater radius. To obtain an expression for this quantity and its relation to depth a model based on the theory of elasticity has been utilized. The behavior of the soil material which is evicted to form the crater is of course governed by the equations of plasticity, as is discussed in Section 2. However, the elastic equations yield a relatively simple expression for the crater dimensions which have been used to predict the depth/radius-ratio.

and which provides a lower bound for the over-all cratering effects, as will be discussed in Section 5.

This method of calculation of crater radius is highly approximate and cannot be rigorously justified. However, it has the virtue of simplicity and appears to agree with the test data reasonably well for the jet conditions studied in this program.

4.1 Point Load Solution: Since the effective area of application of the surface loads is considerably smaller than the crater dimensions for the jet which was used in the tests, the external load is assumed to be a concentrated point load. This is justified through St. Venant's principle which states that influences in a body due to two sets of statically equivalent forces (or moments) applied to a small part of its surface have no significant difference at distances which are large compared with dimensions of that part of surface. (The flat plate pressure tests show that the surface pressure is negligible four inches from the center of the jet.) Assuming that the material in the region of interest is homogeneous and isotropic, the problem reduces to Bossinesq's problem of semi-infinite space subjected to the normally applied loads [8].

The process of the crater formation based on the elastic failure model is illustrated in Figure 51. The salient features of the analysis are summarized in the following five steps:

(a) The stress distribution in the semi-infinite body is determined from the Bossinesq's solution, assuming point loading,

(b) The octahedral shearing stress at any location in the region is determined and equated to the yielding shearing stress of the soil to obtain the first stage failure surface. Inside this surface the octahedral shearing stress is greater than yield, while outside, less than yield. The surface thus obtained is a closed surface which is approximately a sphere whose upper surface is bounded by the surface of the soil,

(c) The material inside this surface is now assumed to become a medium which distributes the externally applied load uniformly along and normal to the surface.

(d) The pressure loading on the initial surface now introduces additional stresses in the unfailed medium, which

(8) Timoshenko, S. and J. N. Goodier, Theory of Elasticity, 2nd Edition, McGraw-Hill Book Co., 1951, pp. 364-369.

causes a failure along a cone defined by the direction of the maximum induced forces,

(e) The part of the soil within the first stage failure surface and that enclosed by the cone are removed to form the initial crater.

In the step (b) of analysis, the soil is assumed to be incompressible and hence, Poisson's ratio may be taken to be 0.5. From the theory of plasticity the elastic medium goes to the plastic range when the octahedral shearing stress exceeds the yielding shearing stress of the medium.

On account of the axial symmetry of the state of stresses about the z-axis through the origin O the shearing stresses in the vertical, radial planes are equal to zero. The other stress components are obtained by means of a stress function satisfying the boundary conditions of a semi-finite body. This solution is known as Bossinesq's equations[8], which are shown as follows

$$\sigma_r = \frac{T}{2\pi}\left[\frac{1-2\nu}{R(R+z)} - \frac{3zr^2}{R^5}\right]$$

$$\sigma_t = \frac{T(1-2\nu)}{2\pi}\left[-\frac{1}{R(R+z)} + \frac{z}{R^3}\right] \qquad (23)$$

$$\sigma_z = -\frac{3T}{2\pi}\frac{z^3}{R^5}$$

$$\tau_{rz} = \frac{3T}{2\pi}\frac{z^2 r}{R^5}$$

where σ_r , σ_t , and σ_z are the normal stresses in radial, tangential and vertical direction in cylindrical coordinate system, τ_{rz} the shearing stress in rz-plane, T the concentrated force applied normally at 0, the Poisson's ratio of the soil medium and $R = \sqrt{r^2 + z^2}$. For incompressible solids, the Poisson's ratio ν has a value of 0.5 and, thus, the stress components become

$$\sigma_r = \frac{T}{2\pi}\left(-\frac{3zr^2}{R^5}\right)$$

$$\sigma_t = 0$$

$$\sigma_z = \frac{T}{2\pi}\left(-\frac{3z^3}{R^5}\right) \qquad (24)$$

$$\tau_{rz} = \frac{T}{2\pi}\left(-\frac{3z^2 r}{R^5}\right)$$

The octahedral shearing stress is given in the cylindrical coordinate system as follows:

$$\tau_{oct.} = \frac{1}{3}\left[(\sigma_r - \sigma_t)^2 + (\sigma_t - \sigma_z)^2 + (\sigma_z - \sigma_r)^2 + 6\tau^2_{rz}\right]^{\frac{1}{2}} \tag{25}$$

Substituting Eq.(24) into Eq. (25) yields

$$\tau_{oct.} = \frac{T z}{\sqrt{2}\pi R^3} \tag{26}$$

From theory of plasticity, the material goes into plastic range when

$$\tau_{oct.} \geq c \tag{27}$$

where c is the yielding shearing stress of the material.

Thus, replacing $\tau_{oct.}$ by c in Eq. (26) gives the equation of a surface in which the soil becomes a perfect plastic medium without shearing strength, i. e.,

$$(r^2 + z^2) = \left(\frac{T}{\sqrt{2}\pi c}\right)^{\frac{2}{3}} z^{\frac{2}{3}} \tag{28}$$

or,

$$r^2 + z^2 = k^{\frac{4}{3}} z^{\frac{2}{3}} \tag{29}$$

where

$$k = \left(\frac{T}{\sqrt{2}\pi c}\right)^{\frac{1}{2}} \tag{30}$$

or

$$k = 0.475\sqrt{\frac{T}{c}} \tag{31}$$

The maximum depth occurs at $r = o$,

$$(z)_{max.} = k = 0.475\sqrt{\frac{T}{c}} \tag{32}$$

and the maximum radius of the surface occurs at $z = 0.44k$,

$$(r)_{max.} = 0.62k \tag{33}$$

A plot of Eq. (29) is illustrated in Figure 51 as the initial rupture surface.

The initial crater depth D from the elastic model is equal to the maximum depth of the elastic failure surface calculated as Eq. (32) and is thus given by

$$D = (z)_{max.} = 0.475\sqrt{\frac{T}{c}} \tag{34}$$

Crater Radius: Following the first stage of failure, the soil medium inside the initial surface of failure is assumed to behave like a fluid which distributes the externally applied load uniformly over and normal to the surface. The surface pressure is simply given by

$$p = \frac{T}{A}\ \alpha \tag{35}$$

where A is the surface area and α is a dimensionless constant expressing the fraction of the total load acting on the failure surface. Its numerical value is unimportant in the subsequent discussions. The surface area A may be obtained by evaluating the integral

$$A = 2\pi\int_s r\, ds$$

$$= 2\pi\int_o^k r\sqrt{1 + \left(\frac{dr}{dz}\right)^2}\, dz \tag{36}$$

Using Eq. (29) the integral yields

$$A = 1.384\ \pi\ k^2 \tag{37}$$

As shown in Figure 51, the pressure over the surface MOM' tends to push the soil above the MM' plane out to form the crater.

An exact calculation of the stress distribution in the surrounding medium resulting from the pressure exerted by the "perfect fluid" inside the initial surface is an extremely difficult and formidable problem in three dimensional elasticity theory, and has not been attempted. Instead, a basic assumption has been made in the analysis. It is assumed that the maximum shearing stresses are along a cone which begins at the maximum radius of the initial surface (points M and M' in Figure 51).

The tangent of the cone angle is given by the ratio of the vertical and horizontal components of the forces above the surfaces OM and OM'. A rupture will occur along this cone which thus defines the secondary surface. The crater radius is determined by the intersection of the rupture cone with the ground surface.

The forces are calculated as follows:

$$F_z = 2\pi\,\alpha p k^2 \int_0^{0.62} \eta\, d\eta$$

$$F_r = 2\pi\alpha p k^2 \int_0^{0.44} (\xi^{\frac{2}{3}} - \xi^2)^{\frac{1}{2}}\, d\xi \qquad (38)$$

where ξ and η are normalized variables defined as

$$\xi = \frac{z}{k}\ ,\ \eta = \frac{r}{k} \qquad (39)$$

After integration of Eq. (38) and also making use of Eqs. (35) and (37), the force components are obtained:

$$F_r = 0.332\ T\ \alpha \qquad (40)$$

$$F_z = 0.275\ \ T\ \alpha$$

Then, from geometry,

$$\tan\ \alpha = \frac{F_z}{F_r} = \frac{0.44k}{R - 0.62k} \qquad (41)$$

where R is the crater radius.

Then, from Eq. (41)

$$\alpha = \tan^{-1}\ \frac{0.275}{0.332} = 39.6 \text{ degrees} \qquad (42)$$

$$R = 1.151k = 1.151D \qquad (43)$$

Equation (43) can be used to prescribe crater radius in terms of crater depth.

5.0 Incipient Cratering Boundary: The plastic flow penetration model gives the condition $\bar{P}/c > 5$ (Eq. (2)) for cratering to occur by the shear failure mechanism. For lower surface pressures cratering is due to the erosion process which has been reported by various workers (References 2, 3, 4).

It is of interest to compare the cratering boundary obtained from the plastic model with that obtained from the yield condition (Eq. (27)) of elasticity. This latter quantity can be obtained by considering the load to be applied over a finite surface area.

A solution for the stress distributions for the case of a load uniformly distributed over a circular area of radius a, as shown in Figure 52 may be found in the literature [9]. The general expression is somewhat involved and will not be presented here. However, for a point directly under the resultant load, i.e., r = o, the expression is considerably simplified [8] and the stresses are given by:

$$\sigma_z = \left[\frac{z^3}{(a^2 + z^2)^{\frac{3}{2}}} - 1 \right] \bar{P}$$

$$\sigma_r = \sigma_t = \left[-2 + \frac{3z}{\sqrt{(a^2 + z^2)}} - \frac{z^3}{\sqrt{(a^2 + z^2)^3}} \right] \bar{P} \qquad (44)$$

$$\tau_{rz} = 0$$

in which the Poissons's ratio is taken as 0.5. $\bar{P}$ is the average surface pressure over the loaded area and is defined as $\bar{P} = T/\pi a^2$. By the same criterion used in Eq. (27), the equation defined the maximum depth is obtained:

$$1 + \left(\frac{D}{a}\right)^2 = 0.79 \left(\frac{\bar{P}}{c}\right)^{\frac{2}{3}} \left(\frac{D}{a}\right)^{\frac{2}{3}} \qquad (45)$$

The dimensionless crater depth (D/a) as a function of $\bar{P}/c$ as obtained from solution of Eq. (45) is also shown in Figure 52. Cratering commences when $\sqrt{\bar{P}/c} > 1.92$, or $\bar{P}/c > 3.7$.

The two boundary regions $\bar{P}/c = 5$ and 3.7 give a measure of comparison of the plastic flow penetration model and the elastic model for the low thrust region. The boundary for the elastic model is about 30 percent lower than the plastic model. This shows that the elastic model gives a lower bound for the cratering process and also implies that for the lower surface pressures and total force levels the crater dimensions obtained from the elastic model would be approximately correct. This provides a measure of justification of its use to calculate the crater depth-radius relation. However, it must be emphasized that for higher stresses the elastic model is not valid and the penetration model must be used.

Parenthetically, it will be noted in Figure 52 that for D/a = 3 the crater depth for this distributed load elastic model is given by $D/a = 0.84\sqrt{\bar{P}/c}$ to an accuracy better than 10 percent. This is identical to the point load solution (Eq. (34)) if we set $T = \pi a^2 \bar{P}$. This result is what would be expected from St. Venant's principle.

(9) A. E. H. Love, Transactions Royal Society (London), Series A, Vol. 228, 1929.

6.0 Gravitational Effects (Elastic Model): The elastic model of Section 4 which has been used to determine the crater radius-depth relation has an advantage of simplicity and will serve as a rough rule-of-thumb prediction of the crater dimensions for lower thrusts and surface pressure conditions. However, the development of Section 4 is not valid for soils such as sand which possess low cohesive strengths and whose yield strength is primarily due to Coulomb friction between the individual soil particles.

In such materials, the yielding stress is given by a relation of the form

$$\tau = c + \sigma_n \tan\phi \tag{46}$$

Normally for sand, c is quite small while ϕ is on the order of 30 degrees. In sand, c is primarily a function of moisture content and is largest for damp sands. In sand the frictional forces arising from gravitational loading are primarily responsible for the strength properties. Therefore, these effects must be included to treat such soils.

Gravitational forces give rise to a vertical stress component - γZ and a stress component in any plane perpendicular to the gravitational field - $K\gamma Z$. Here, γ is the soil specific weight and K is a dimensionless constant whose value ranges from about 0.5 for a soil which has never known stresses other than those due to an existing overburden, to unity or greater if cycles of stress application and release have occurred. K is commonly referred to in literature as the earth pressure coefficient and must be regarded as a semi-empirical soil parameter which is constant over a certain range of loading conditions, depending on the particular soil. Using the point load approximation for the stresses induced in the soil by the jet forces with $T = \pi a^2 \bar{P}$ the stresses in the soil directly under the jet (r = o) are given by:

$$\begin{aligned} \sigma_t &= \sigma_r = -K\gamma Z \\ \sigma_z &= -\frac{3a^2\bar{P}}{2Z^2} - \gamma Z \\ \tau_{rz} &= 0 \end{aligned} \tag{47}$$

The yield condition gives for the point directly under the jet:

$$\frac{\sqrt{2}}{3}\left|\sigma_z - \sigma_t\right| = \tau \tag{48}$$

The normal stress across the yielding surface, σ_n, is given by the first stress invarient

$$\sigma_n = \frac{\sigma_r + \sigma_t + \sigma_z}{3} = \frac{\sigma_z + 2\sigma_t}{3} \tag{49}$$

Thus, the yield condition is:

$$\frac{\sqrt{2}}{3}\left|\sigma_z - \sigma_t\right| = c + \left|\frac{\sigma_z + 2\sigma_t}{3} \tan\phi\right| \qquad (50)$$

From Eqs. (47) and (50) we obtain the following expression for the crater depth:

$$n\,(D/a)^3 + m\,(D/a)^2 - 1 = 0 \qquad (51)$$

where

$$n = \left[\frac{2\tan\phi + \sqrt{2}}{\sqrt{2} - \tan\phi} K - 1\right] \frac{2\gamma a}{3\bar{P}}$$

$$m = \frac{2}{\sqrt{2} - \tan\phi} \frac{c}{\bar{P}}$$

It will be noted that when $\gamma = 0$, and $\phi = 0$, $n = 0$ and the depth equation reduces to

$$\frac{D}{a} = 0.84\sqrt{\frac{\bar{P}}{c}} \quad .$$

For cohesionless soils, $c = o$, the equation becomes

$$\frac{D}{a} = \left(\frac{1}{n}\right)^{\frac{1}{3}} \sim \bar{P}^{\frac{1}{3}} \quad .$$

VI. COMPARISON OF THEORY AND TEST DATA

Comparison of the crater radius and depth data with the theory presented in Section V is made in Figures 44 through 47 in the form of curves passing through the test data points. The parameter c is the yield stress of the material under zero normal load. The solid lines are based on the penetration model (Eqs. (4) and (7)) while the dashed lines are based on the elastic failure criteria (Eq. 51). Both models were included for comparative purposes. However, the penetration model based on plasticity equations is the more nearly correct, theoretically. The elastic model is included because of the basic simplicity of the cratering equations.

In Figures 44 and 46 the theoretical radius curves were obtained from the relation $R = 1.15D$ (Eq. (43)).

Figures 44 and 45 are for cohesionless sand and for sand having a cohesive strength of 0.2 psi. This represents the upper limit to be expected for the sand cohesive strength in the moist condition. In all curves the internal friction angle ϕ is 30 degrees, and K is 0.5.

Also included are curves showing the effects of soil pore pressure induced by diffusion. The soil pore pressure effects were calculated by replacing the soil cohesive stress c by the term $-(P - P_\infty)\tan\phi$ obtained from Eq. (22) and using this quantity in the penetration equations (Eqs. (4) and (7)) and in the elastic failure equations (Eq. (51)). It can be seen that in sand the pressure buildup is quite significant in crater formation for the lower surface pressure (thrust) conditions. At the higher pressure conditions its effect is less pronounced. For example, with a surface pressure of 25 psi the penetration model shows that the crater dimensions are increased by a factor of about 30 percent while at 6 psi they are more than doubled. In the very low surface pressure region, buildup may be even more significant than is indicated in the figures. Certain approximations made in solving the penetration equations with pore pressure included are not entirely valid in this region and somewhat underpredict the effect. Further investigations along these lines are considered desirable to completely evaluate this effect.

Figures 46 and 47 are for clay. In these calculations the clay was assumed to be perfectly plastic, i.e., $\phi = 0$. The parameter is the cohesive strength c. In the shear tests conducted on the clay at the cold test site, c was found to vary from about 0.4 psi to values as great as 1.6 psi at points as close as 20 feet to each other. However, the friction angle was less than 10 degrees in each case. It can be seen that the theoretical curves fit the data within the observed range of the cohesive strength.

At this point it is worthy to note that the measured shear strength was quite low. For homogeneous soft clay the shear strength is normally 5 - 10 psi. It is believed that the low value resulted from minute faults and fissures in the clay soil and the resultant trapped air. For shear tests involving small amounts of material, relatively homogeneous samples would be encountered and the measured strength would be large. However, in large samples the effects of the faults would be evident since failure would first be along the weakest fault. After the initial failure, local stress concentrations would reach quite high values in the fault areas and will thus cause the effective shear strength of this large sample to be much less than a small sample. The shear test apparatus used was 18" x 18" x 4" and sheared an area comparable to the crater area. The shear strength measured by this apparatus was thus approximately the effective shear strength of the medium for purposes of cratering calculations.

It is of some interest to compare the results of the more theoretically correct penetration model (solid curves) to the elastic failure model (dashed lines). For cohesionless materials (sand) the elastic failure model yields a function dependence of $\sqrt[3]{\overline{P}}$ for crater dimensions and for cohesive soils $\sqrt[2]{\overline{P}}$. The penetration model gives a somewhat complicated dependance of crater dimensions on $\overline{P}$ but it can be shown that for large $\overline{P}$ the variation is as the first power. This trend appears to be compatible with the crater depth data, especially for clay.

It can be seen that for small $\overline{P}$ the elastic model overpredicts the crater dimensions, as is explained in Section V of the report where the boundary regions for "explosive" cratering are derived, and thus this represents a conservative engineering tool for estimating crater dimensions. However, for high surface pressure levels the results are much too small.

The crater radius which is based on the relation $R = 1.15D$ is valid in the low pressure region, but will break down at higher levels as is indicated in Figure 44(sand). A more accurate calculation of crater radius will require further theoretical development.

VII. EVALUATION OF PROGRAM ACCOMPLISHMENTS

All technical contractual objectives of the program have been achieved. In addition, certain areas were investigated which were beyond the original scope of the program when it became apparent in the course of the study that they were significant.

In the test program all the hot firing tests specified were performed, and in addition, a number of static hot tests were made. In the cold gas tests, a large number of stationary and moving tests were performed to evaluate the basic cratering mechanism. In some instances, these were covered by high speed (Fastax) camera photography which gave particular insight into the process of crater formation. A hitherto unenumerated cratering process was observed from these movies. When the surface pressure from the jet is greater than a relatively low value, cratering results from an "explosive" process rather than from gradual erosion. The ejected material rose to a height of 60 feet in some cases.

In moving jets the crater (or trench) dimensions have been found to be reduced from the stationary values by a factor of 2/3 in width and 1/2 in depth for horizontal velocities up to 30 ft/sec. These empirical factors appear to be valid within the scatter of the test data.

A series of theoretical equations have been developed which predict the static explosive crater dimensions within the accuracy of the test data and which can be used to determine the crater dimensions resulting from a single jet at normal incidence over a homogeneous soil. The significant parameters are the jet ground pressure distribution and the soil cohesive strength and friction angle.

For jet surface pressures less than approximately 10 psi the crater depth can be predicted by Eq.(51) for materials having both friction and cohesion and by Eq.(45) for perfectly plastic materials (clay). The radius is given by the relation $R = 1.15D$. The crater dimensions given by these relations will be somewhat larger than the actual dimensions in the low pressure range and will

serve as a useful engineering tool in this case. The boundary region for explosive cratering is given by $\bar{P}/c = 3.7$ for materials where pore pressure can be neglected (wet clay soils). $\bar{P}$ and c are the jet surface pressure and soil cohesive strengths, respectively. Pore pressure effects will reduce this boundary by a significant amount in porous soils. Detailed evaluation of this will require further investigation.

For higher surface pressures the more complicated penetration model (Eqs.(4) and (7)) must be used since the "engineering equations" underpredict the crater dimensions in this region. The surface pressure regions where the "engineering equations" should no longer be used will depend to a large extent on the apparent seriousness of the problem as per these equations, time available for more detailed analysis, and the judgment of the practicing engineer.

The soil cohesive strength parameter c, which is used in all calculations, should be determined by shearing tests involving large samples of the material comparable to the crater dimensions rather than small samples. Such tests will include the effects of faults and fissures, etc., which are present in real soils.

The results of the program have been substantial, but point out many problem areas which should be further investigated. For example, it is apparent that "explosive" cratering can be potentially dangerous in many mission applications and this phenomenon should be thoroughly determined. The phenomenon may be especially important in the LEM system since the Surveyor and Russian lunar programs have shown that the lunar surface is in many respects like loose porous sand. When the Descent Stage is firing at full thrust near the ground, the surface pressure will be in excess of 1 psi. The pore pressure induced by the jet, coupled with the low lunar gravity, will drastically reduce the Coulomb frictional forces in the soil and the threshhold pressure for "explosive" cratering will be quite low. The pore pressure effect can be more significant in a vacuum environment than for a jet firing in the ambient atmosphere and will offset the lower surface pressures resulting from greater jet expansion in a vacuum. Thus, one could reasonably expect violent explosive cratering. The height which the ejected debris will travel will be much higher than on earth, due both to the reduced gravity and the absence of atmosphere.

PHOTO OF COLD TEST APPARATUS

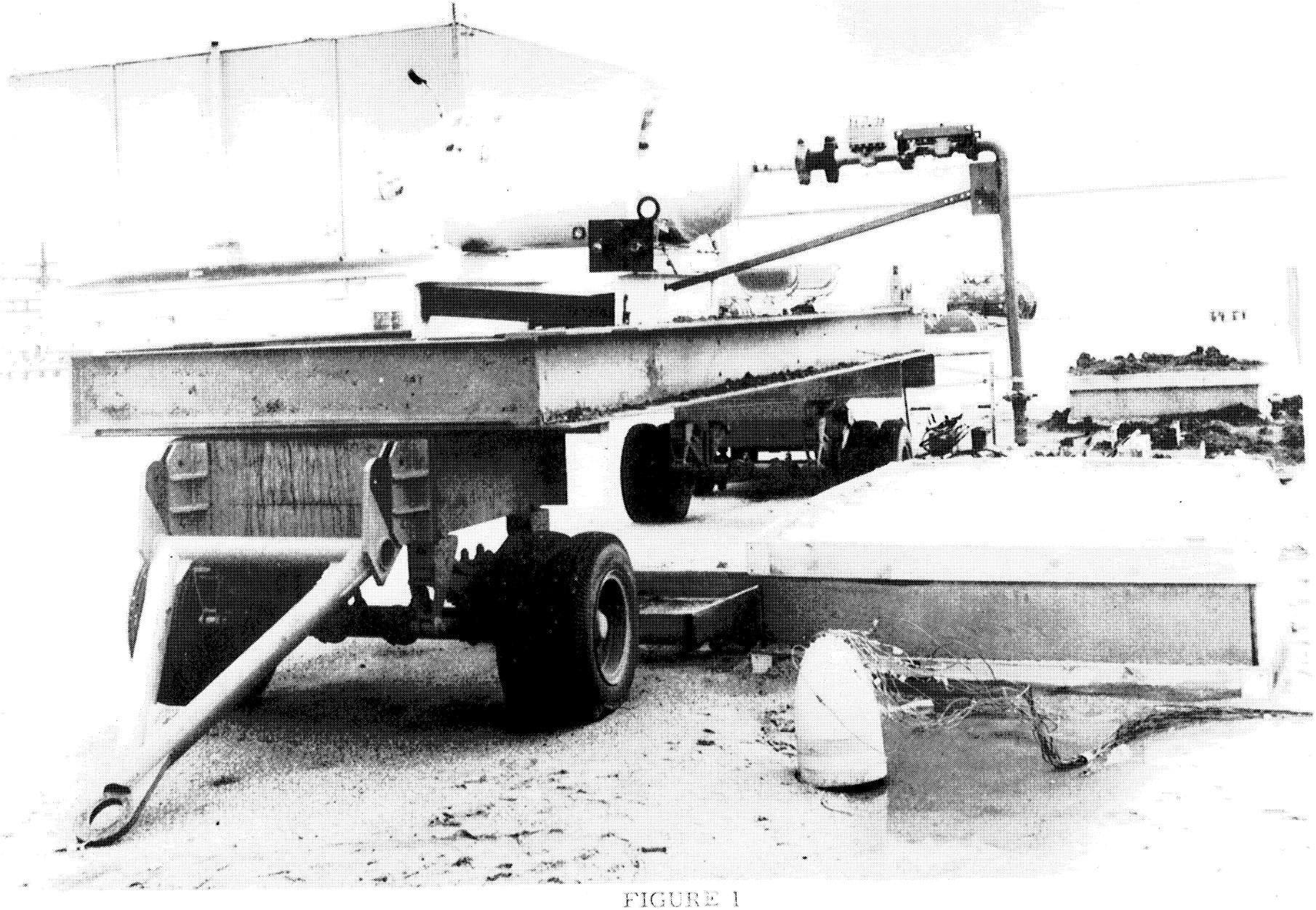

FIGURE 1

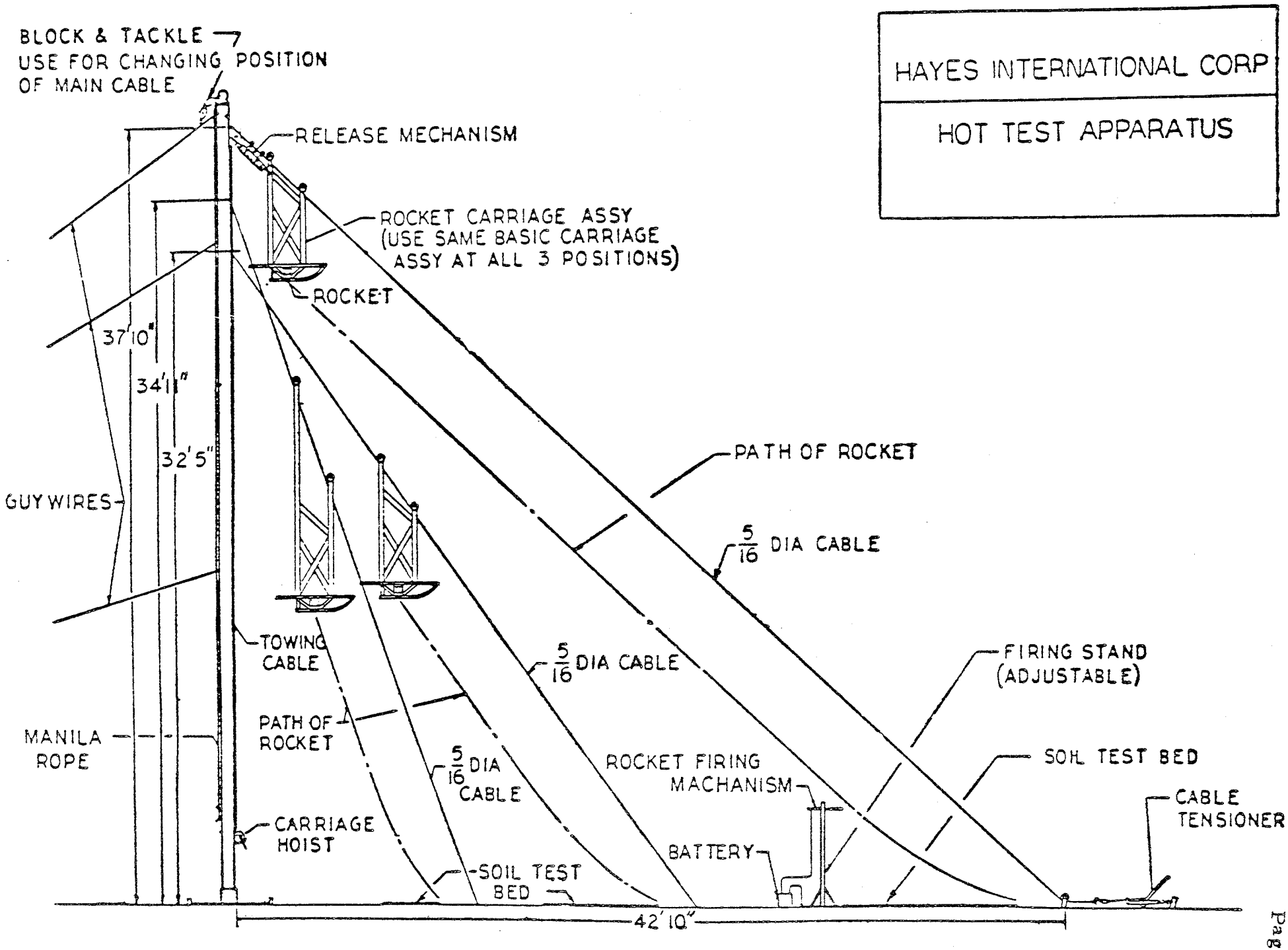
BLOCK & TACKLE
USE FOR CHANGING POSITION
OF MAIN CABLE
HAYES INTERNATIONAL CORP
HOT TEST APPARATUS
RELEASE MECHANISM
ROCKET CARRIAGE ASSY
(USE SAME BASIC CARRIAGE
ASSY AT ALL 3 POSITIONS)
ROCKET
37'10"
34'11"
32'5"
GUY WIRES
PATH OF ROCKET
5/16 DIA CABLE
TOWING
CABLE
5/16 DIA CABLE
FIRING STAND
(ADJUSTABLE)
MANILA
ROPE
PATH OF
ROCKET
5/16 DIA
CABLE
ROCKET FIRING
MACHANISM
SOIL TEST BED
CABLE
TENSIONER
CARRIAGE
HOIST
BATTERY
SOIL TEST
BED
42'10"

FIGURE 2

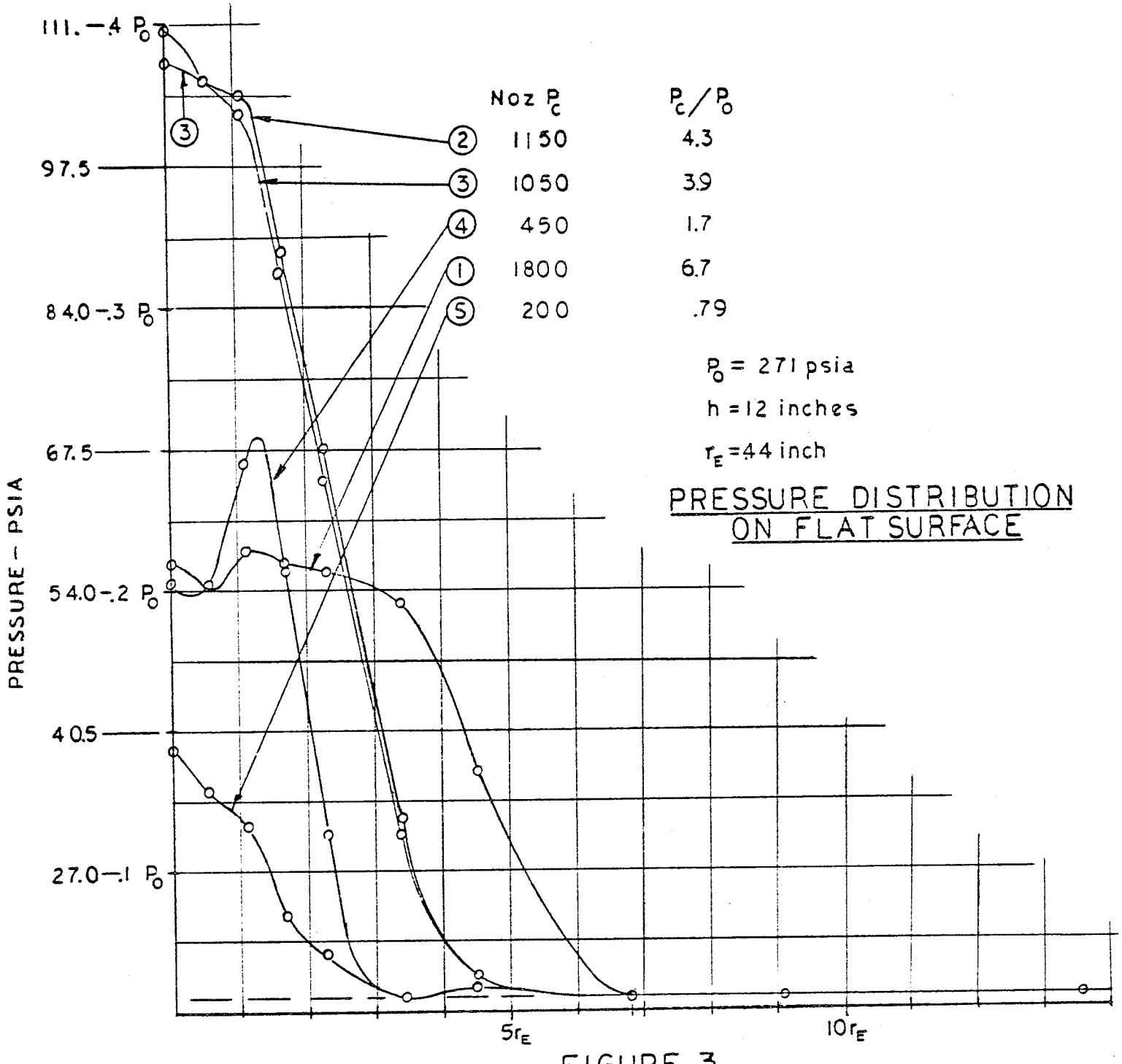
111. −.4 P0
97.5
84.0 −.3 P0
67.5
54.0 −.2 P0
40.5
27.0 −.1 P0
PRESSURE − PSIA
Noz Pc
Pc/P0
② 1150 4.3
③ 1050 3.9
④ 450 1.7
① 1800 6.7
⑤ 200 .79
P0 = 271 psia
h = 12 inches
rE = .44 inch
PRESSURE DISTRIBUTION ON FLAT SURFACE
5rE
10rE

FIGURE 3

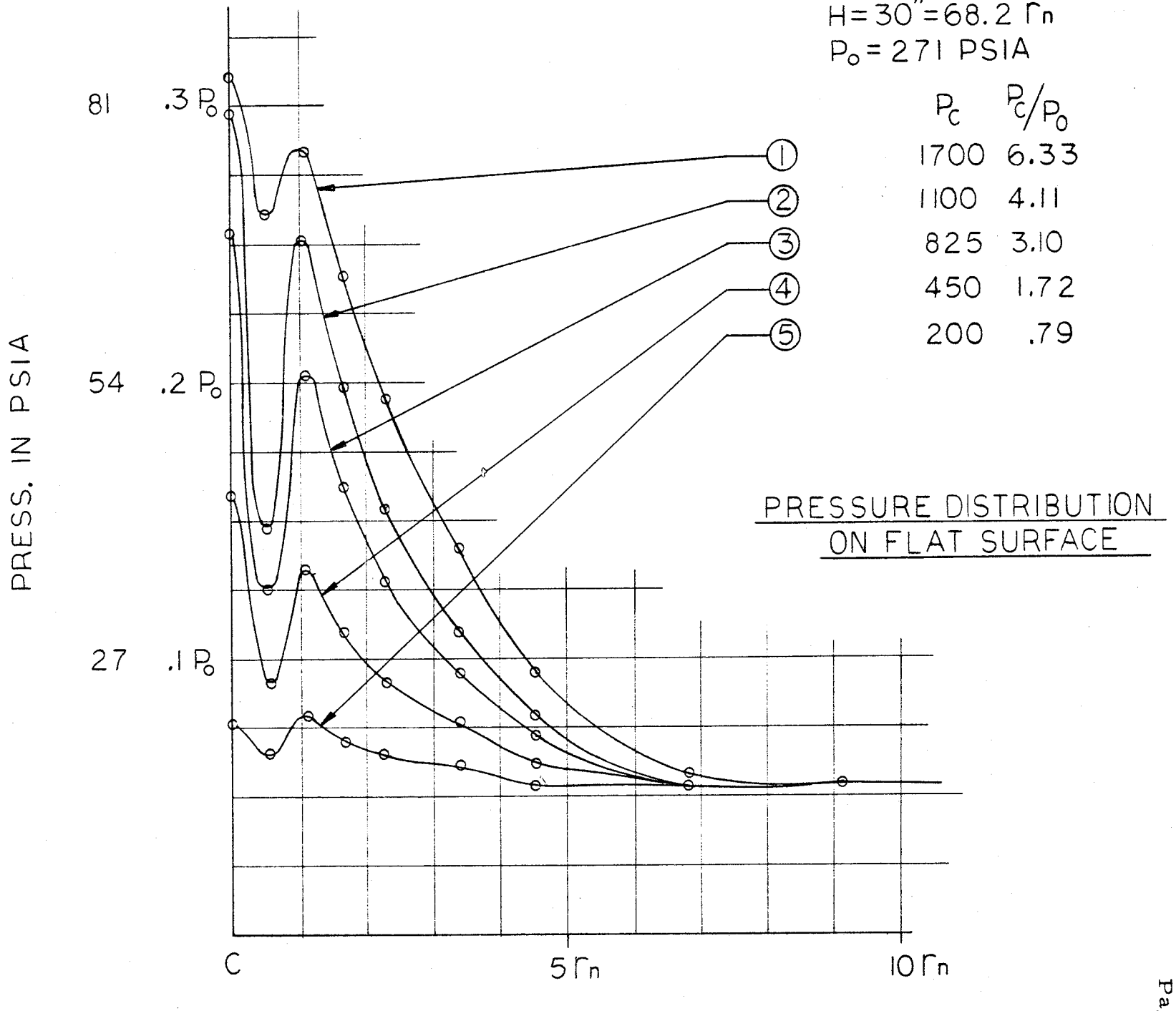
H = 30" = 68.2 rn
Po = 271 PSIA
Pc Pc/Po
1700 6.33
1100 4.11
825 3.10
450 1.72
200 .79
PRESSURE DISTRIBUTION ON FLAT SURFACE
PRESS. IN PSIA
81 .3 Po
54 .2 Po
27 .1 Po
C
5 rn
10 rn
1
2
3
4
5

FIGURE 4

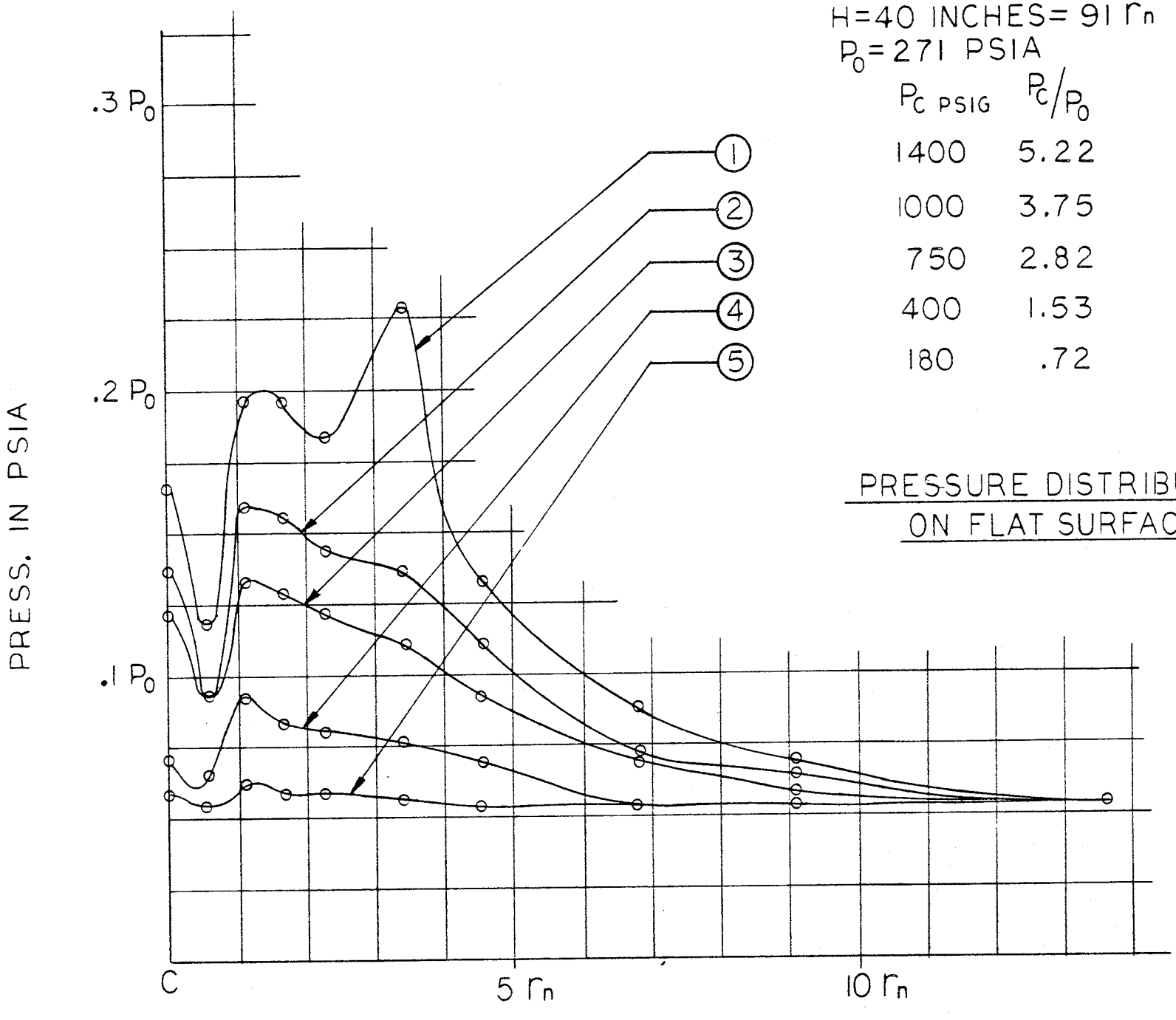
H=40 INCHES= 91 r_n
P_0= 271 PSIA
$P_{C\ PSIG}$ P_C/P_0
1400 5.22
1000 3.75
750 2.82
400 1.53
180 .72
PRESSURE DISTRIBUTION ON FLAT SURFACE
PRESS. IN PSIA
.3 P_0
.2 P_0
.1 P_0
C
5 r_n
10 r_n
1
2
3
4
5

FIGURE 5

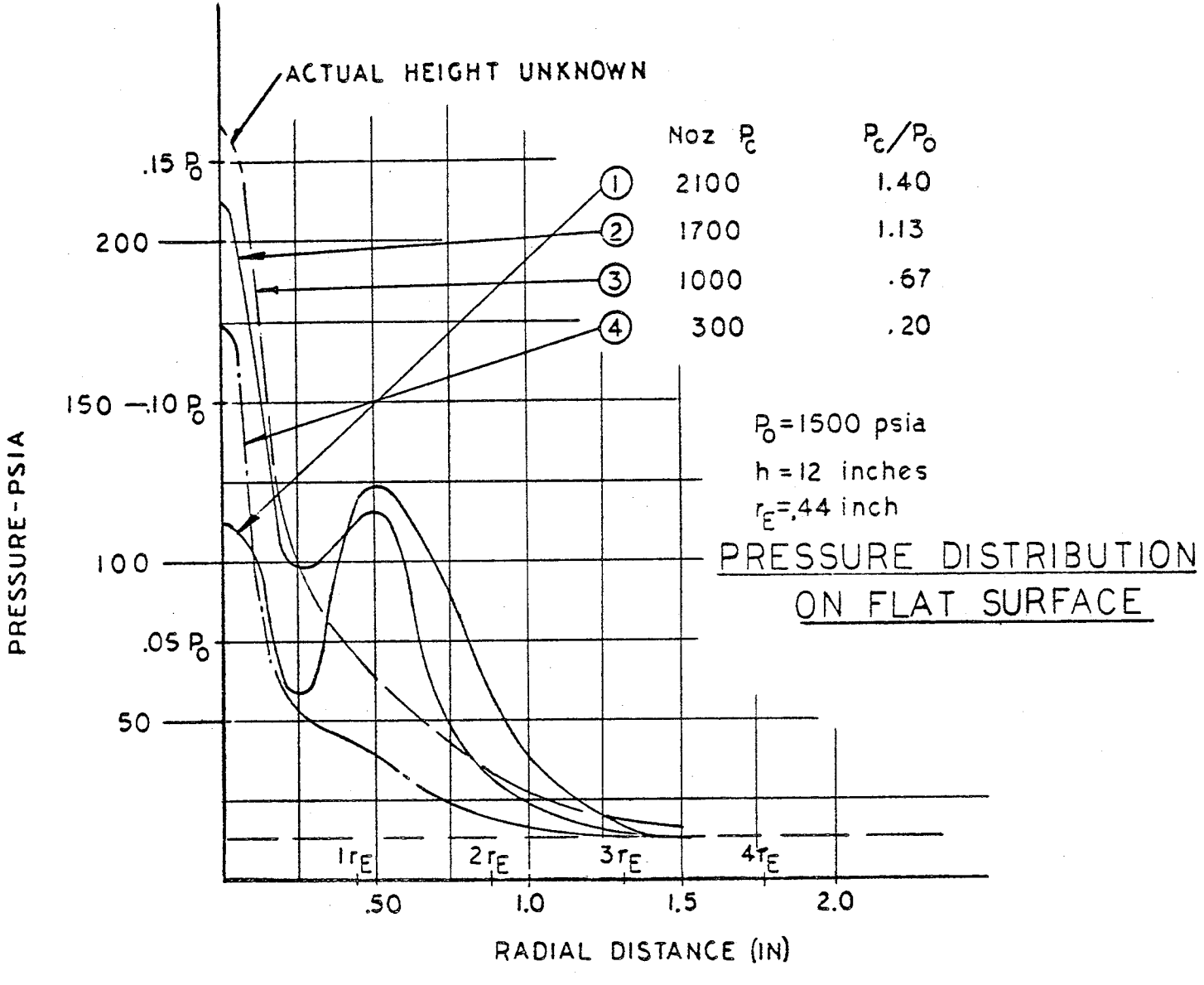
ACTUAL HEIGHT UNKNOWN
Noz P_c
P_c/P_o
① 2100 1.40
② 1700 1.13
③ 1000 .67
④ 300 .20
P_o=1500 psia
h = 12 inches
r_E=.44 inch
PRESSURE DISTRIBUTION ON FLAT SURFACE
PRESSURE-PSIA
.15 P_o
200
150
.10 P_o
100
.05 P_o
50
1r_E
2r_E
3r_E
4r_E
.50
1.0
1.5
2.0
RADIAL DISTANCE (IN)

FIGURE 6

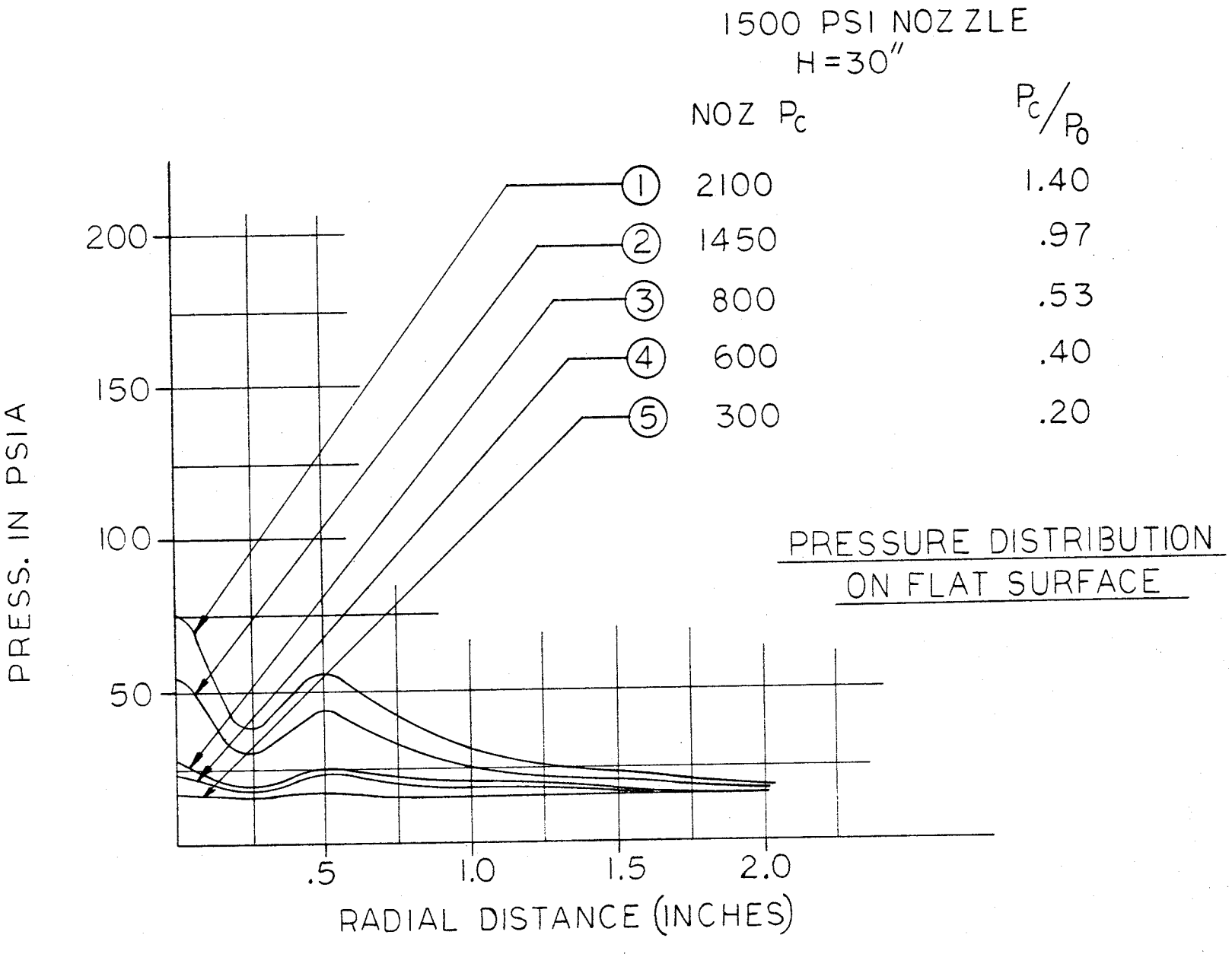
1500 PSI NOZZLE
H=30"
NOZ P_c
P_c/P_o
1 2100 1.40
2 1450 .97
3 800 .53
4 600 .40
5 300 .20
PRESSURE DISTRIBUTION
ON FLAT SURFACE
PRESS. IN PSIA
200
150
100
50
.5
1.0
1.5
2.0
RADIAL DISTANCE (INCHES)

FIGURE 7

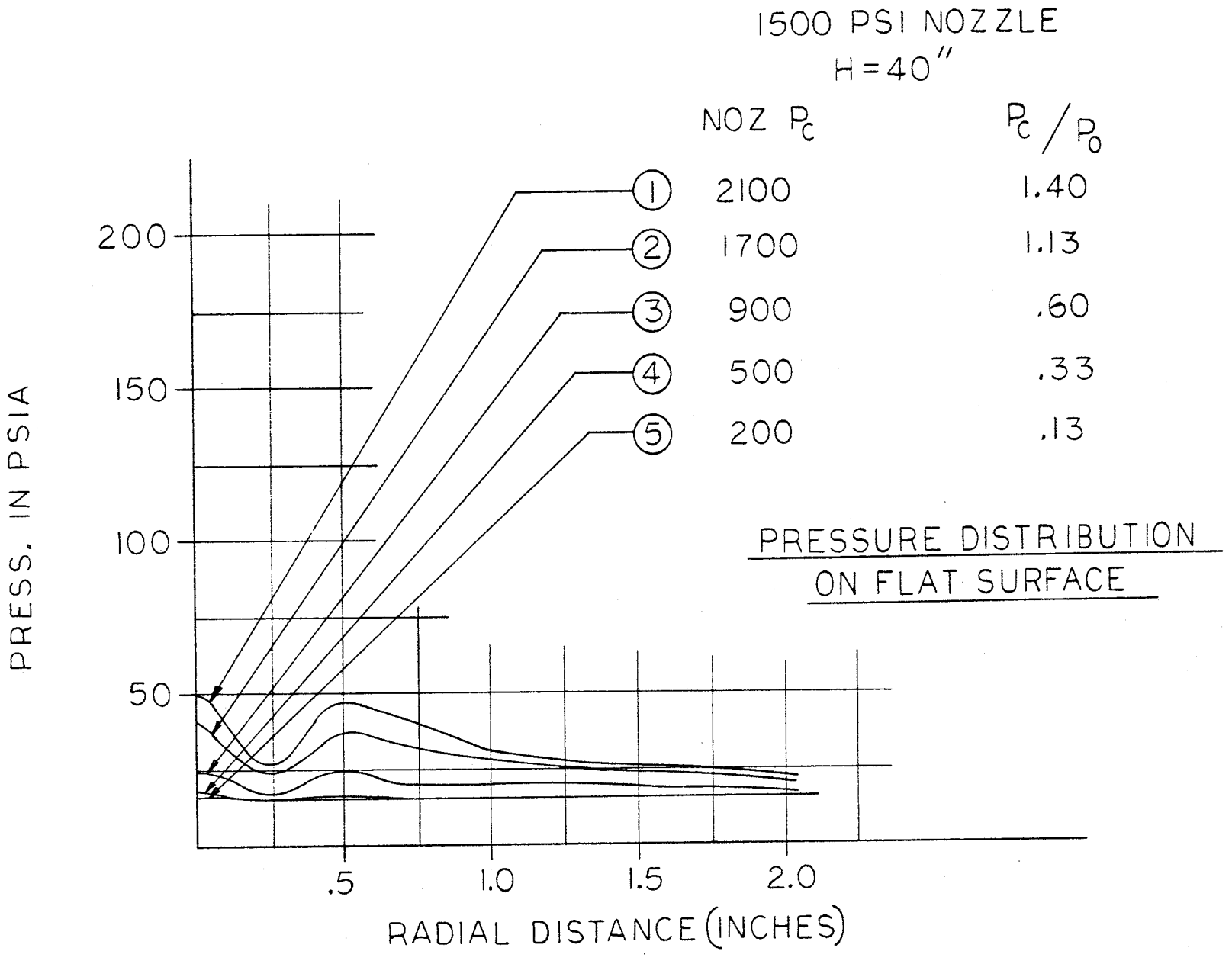
1500 PSI NOZZLE
H = 40"
NOZ P_c
P_c / P_o
① 2100 1.40
② 1700 1.13
③ 900 .60
④ 500 .33
⑤ 200 .13
PRESSURE DISTRIBUTION
ON FLAT SURFACE
PRESS. IN PSIA
200
150
100
50
.5
1.0
1.5
2.0
RADIAL DISTANCE (INCHES)

FIGURE 8

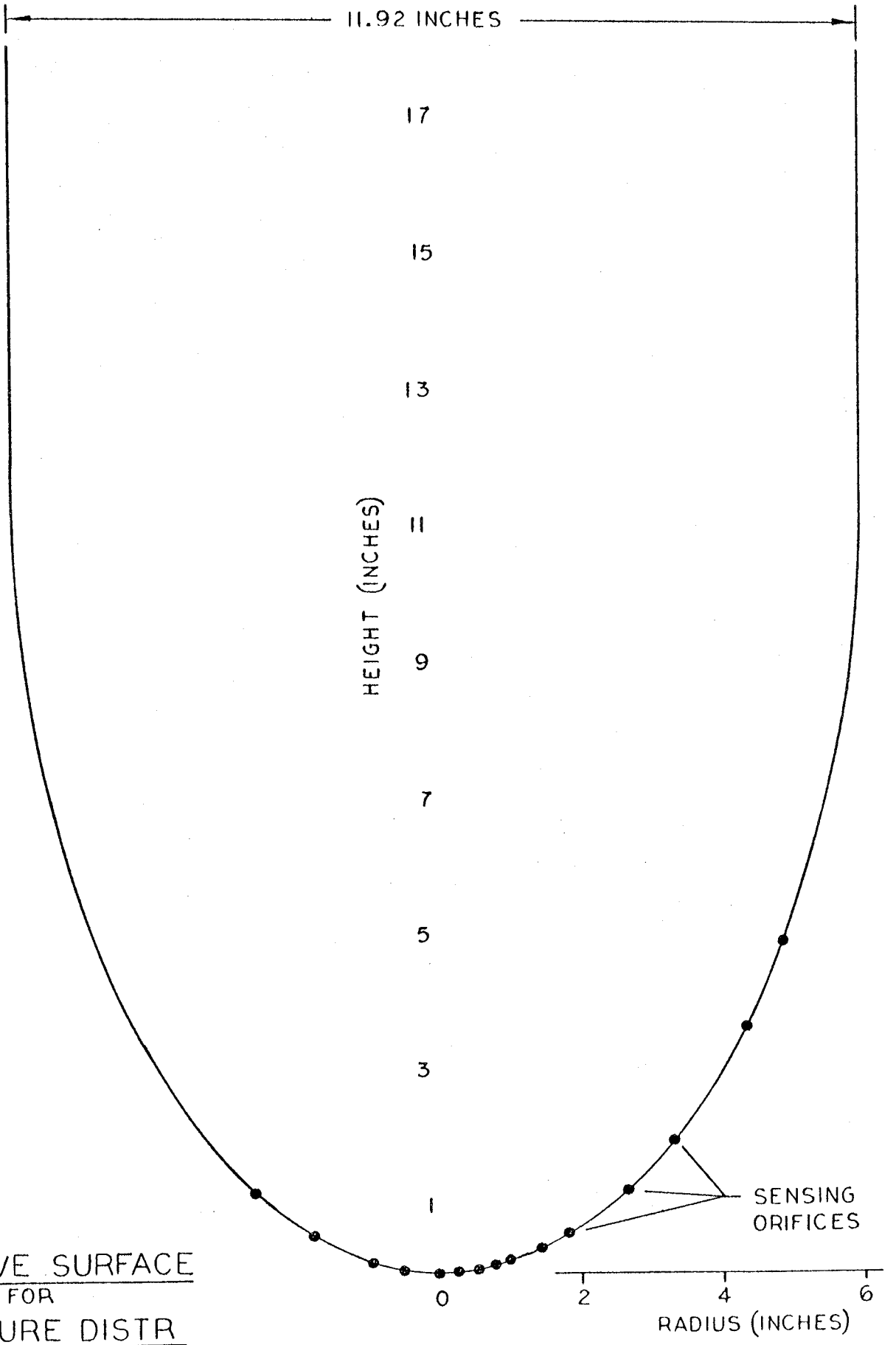

CONCAVE SURFACE
FOR
PRESSURE DISTR
MEASUREMENTS

FIGURE 9

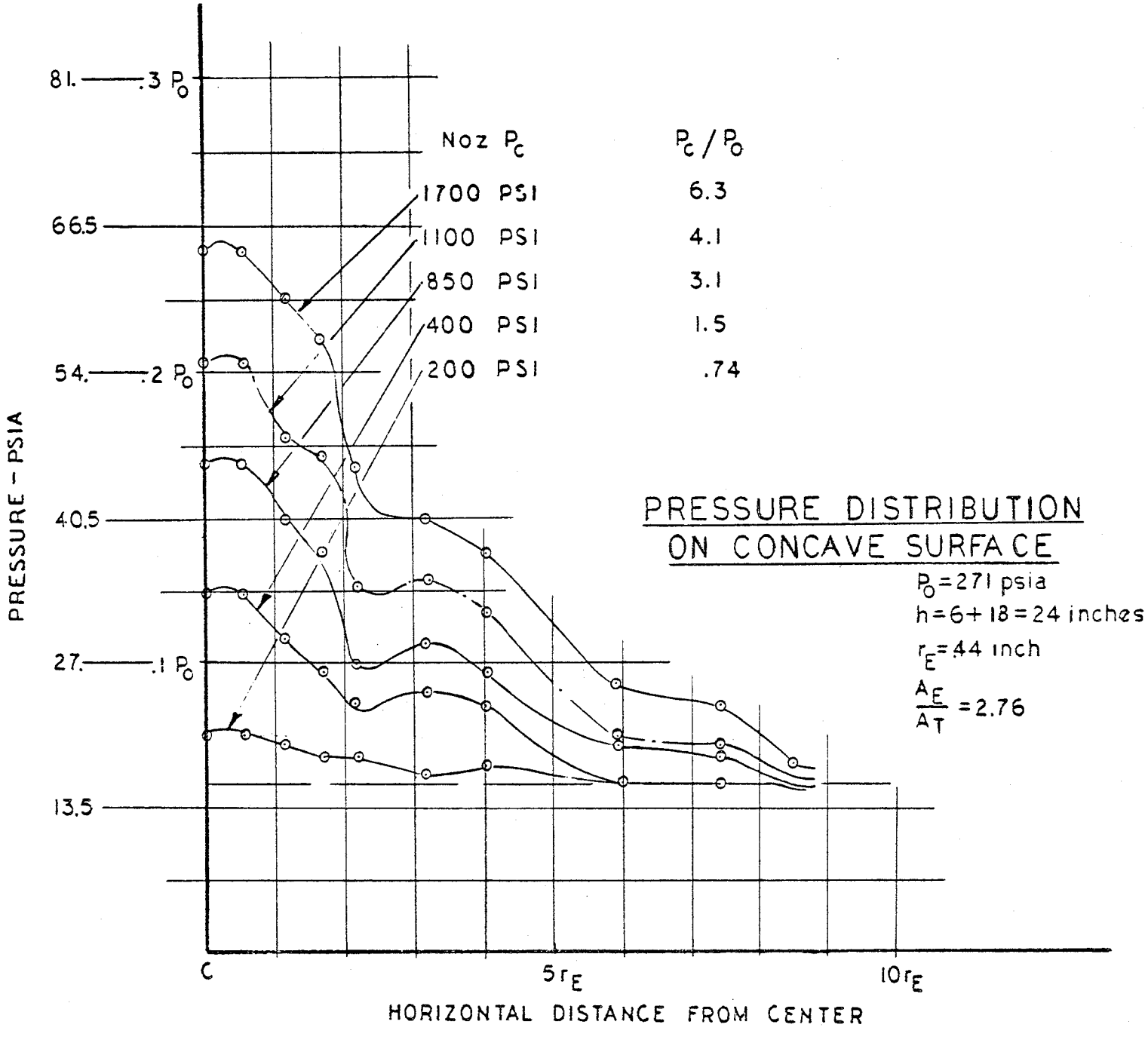
81. .3 P_o
66.5
54. .2 P_o
40.5
27. .1 P_o
13.5
PRESSURE - PSIA
Noz P_c
P_c / P_o
1700 PSI 6.3
1100 PSI 4.1
850 PSI 3.1
400 PSI 1.5
200 PSI .74
PRESSURE DISTRIBUTION ON CONCAVE SURFACE
P_o = 271 psia
h = 6 + 18 = 24 inches
r_E = .44 inch
$\frac{A_E}{A_T}$ = 2.76
C
$5r_E$
$10r_E$
HORIZONTAL DISTANCE FROM CENTER

FIGURE 10

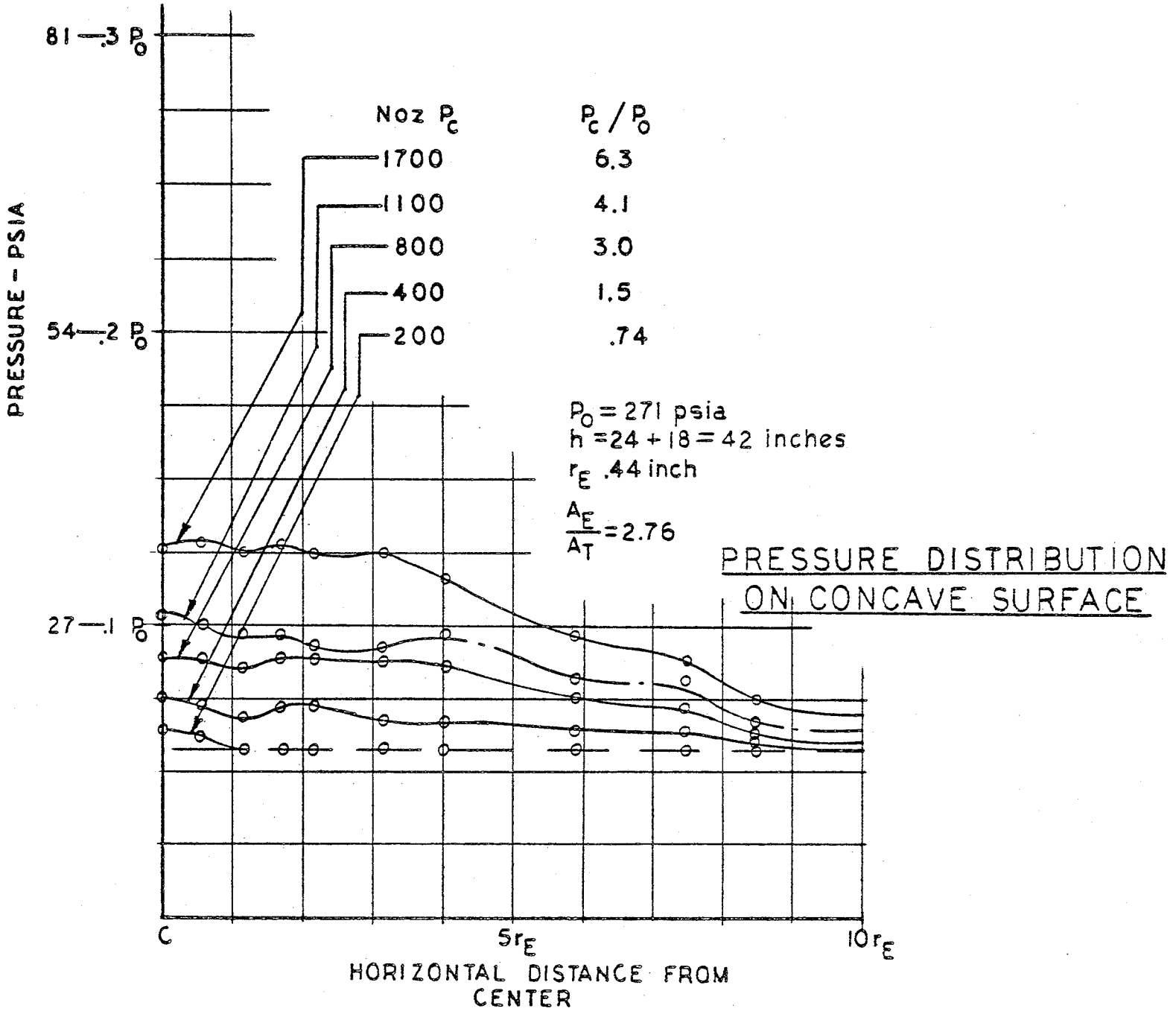
81 — .3 P_o
54 — .2 P_o
27 — .1 P_o
PRESSURE - PSIA
Noz P_c
P_c / P_o
1700
6.3
1100
4.1
800
3.0
400
1.5
200
.74
P_o = 271 psia
h = 24 + 18 = 42 inches
r_E .44 inch
$\frac{A_E}{A_T}$ = 2.76
PRESSURE DISTRIBUTION ON CONCAVE SURFACE
C
$5r_E$
$10r_E$
HORIZONTAL DISTANCE FROM CENTER

FIGURE II

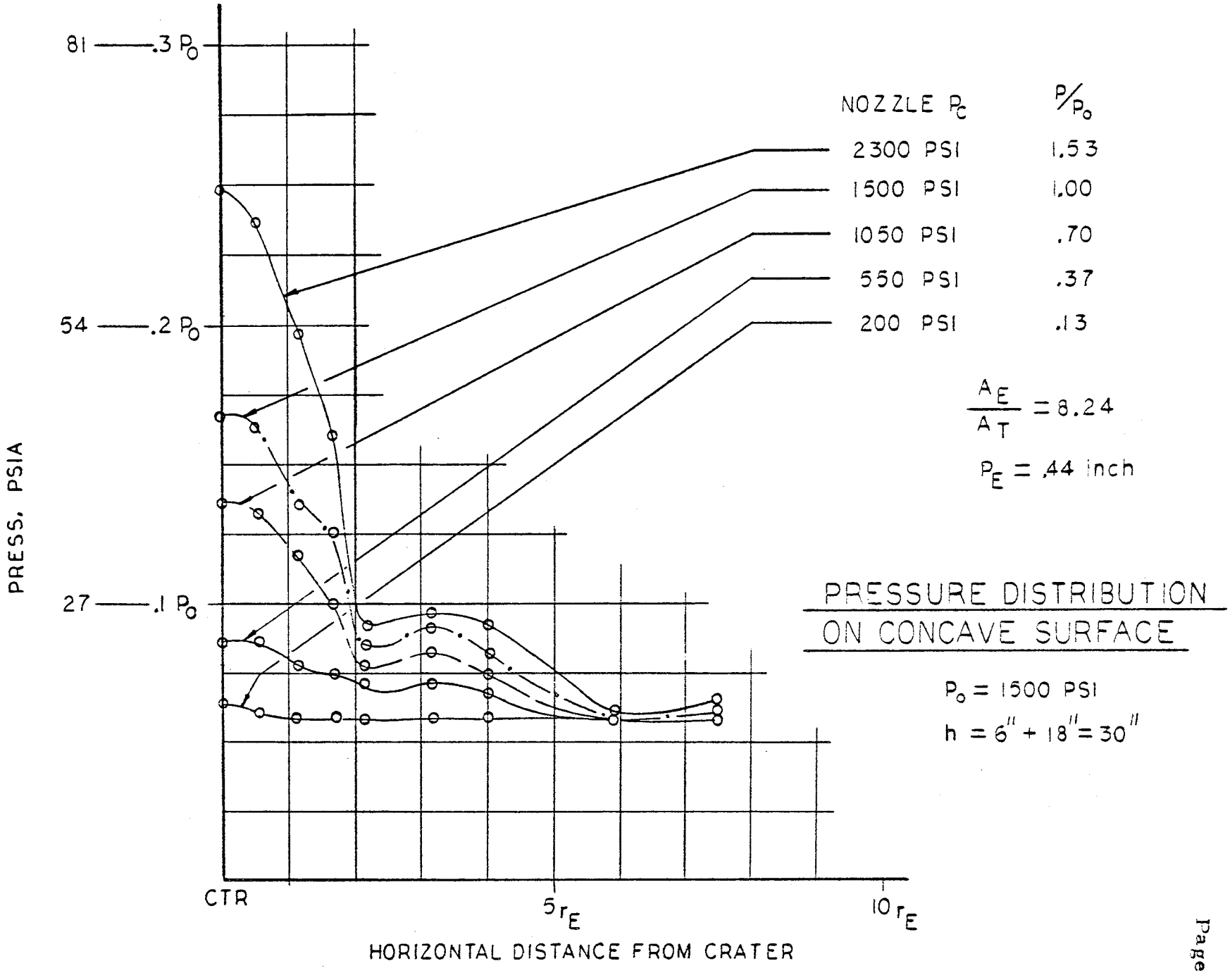
81 .3 P_o
54 .2 P_o
27 .1 P_o
PRESS. PSIA
NOZZLE P_c P/P_o
2300 PSI 1.53
1500 PSI 1.00
1050 PSI .70
550 PSI .37
200 PSI .13
$\frac{A_E}{A_T} = 8.24$
$P_E = .44$ inch
PRESSURE DISTRIBUTION
ON CONCAVE SURFACE
$P_o = 1500$ PSI
$h = 6'' + 18'' = 30''$
CTR
$5r_E$
$10r_E$
HORIZONTAL DISTANCE FROM CRATER

FIGURE 12

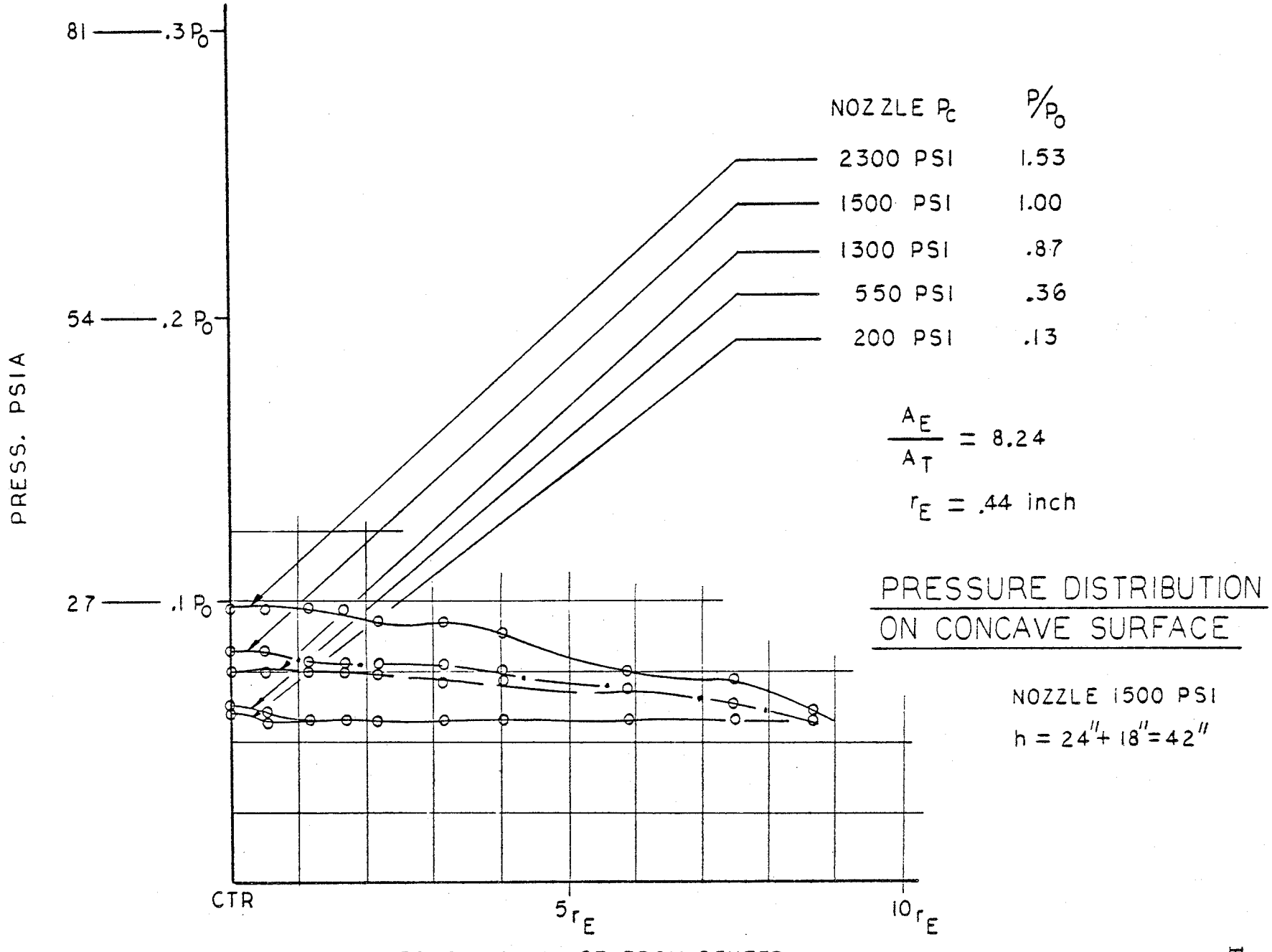
81 — .3 P0
54 — .2 P0
27 — .1 P0
PRESS. PSIA
NOZZLE Pc
P/P0
2300 PSI 1.53
1500 PSI 1.00
1300 PSI .87
550 PSI .36
200 PSI .13
AE/AT = 8.24
rE = .44 inch
PRESSURE DISTRIBUTION
ON CONCAVE SURFACE
NOZZLE 1500 PSI
h = 24" + 18" = 42"
CTR
5rE
10rE
HORIZONTAL DISTANCE FROM CENTER

FIGURE 13

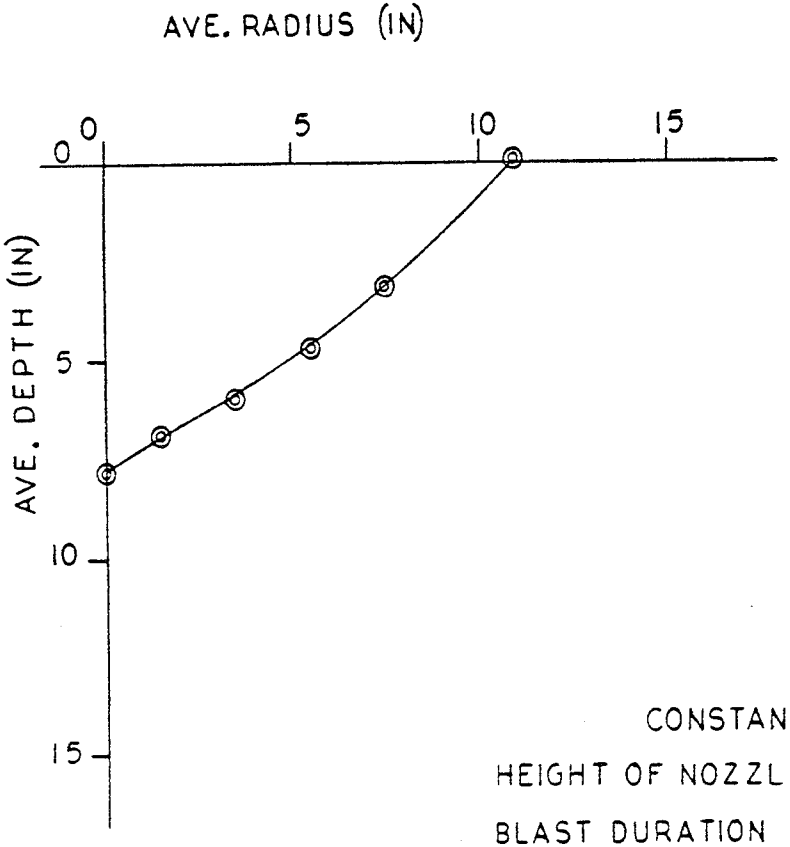

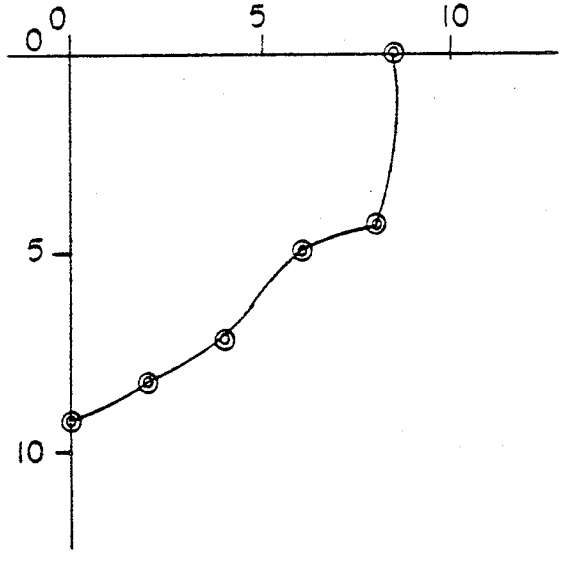

CONSTANTS			
HEIGHT OF NOZZLE	22.4"	HEIGHT OF NOZZLE	30"
BLAST DURATION	.5 SEC	BLAST DURATION	1.01 SEC
LINE PRESSURE	750 PSI	LINE PRESSURE	300 PSI
AVERAGE NOZZLE CHAMBER PRESSURE	232 PSI	NOZZLE CHAMBER PRESSURE	171 PSI

SAND CRATER CONTOURS

FIGURE 14

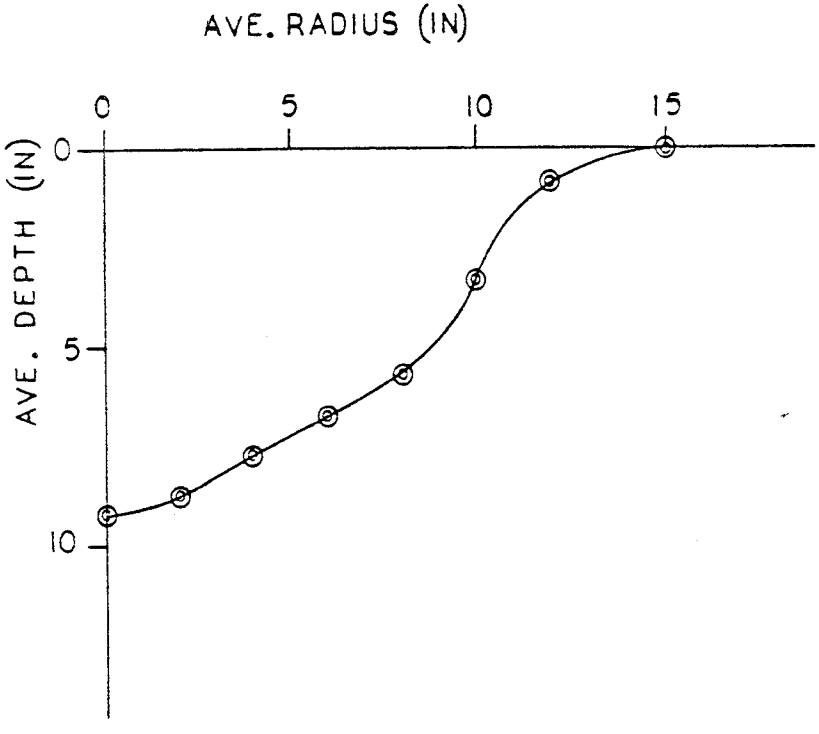

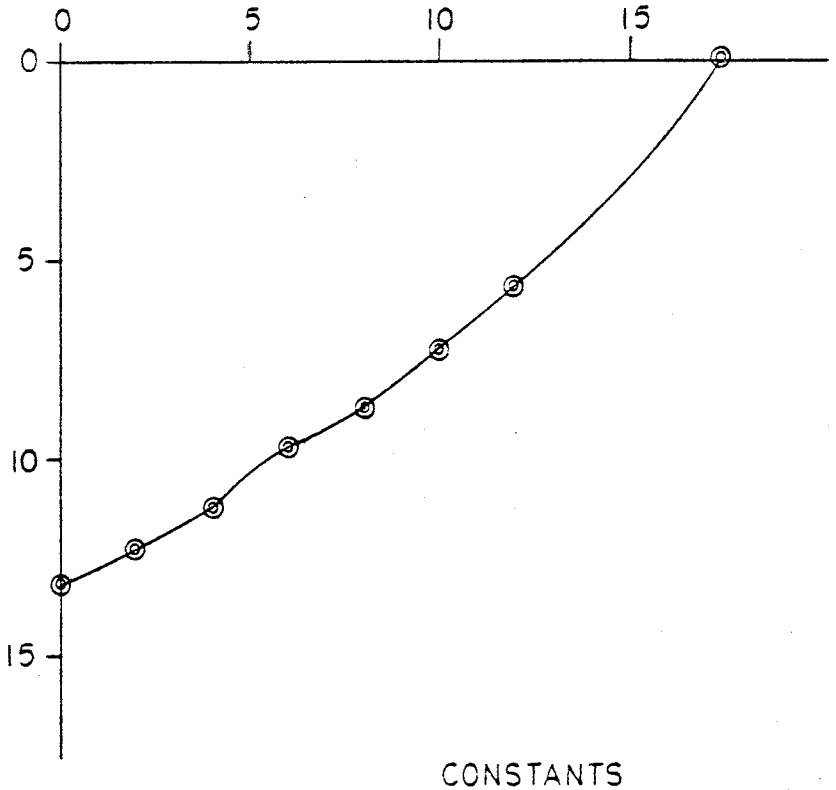

CONSTANTS	
HEIGHT OF NOZZLE	30"
BLAST DURATION	.7 SEC
LINE PRESSURE	850 PSI
NOZZLE CHAMBER PRESSURE	750 PSI

CONSTANTS	
HEIGHT OF NOZZLE	30"
BLAST DURATION	.8 SEC
LINE PRESSURE	2700 PSI
AVERAGE NOZZLE CHAMBER PRESSURE	838 PSI

SAND CRATER CONTOURS

FIGURE 15

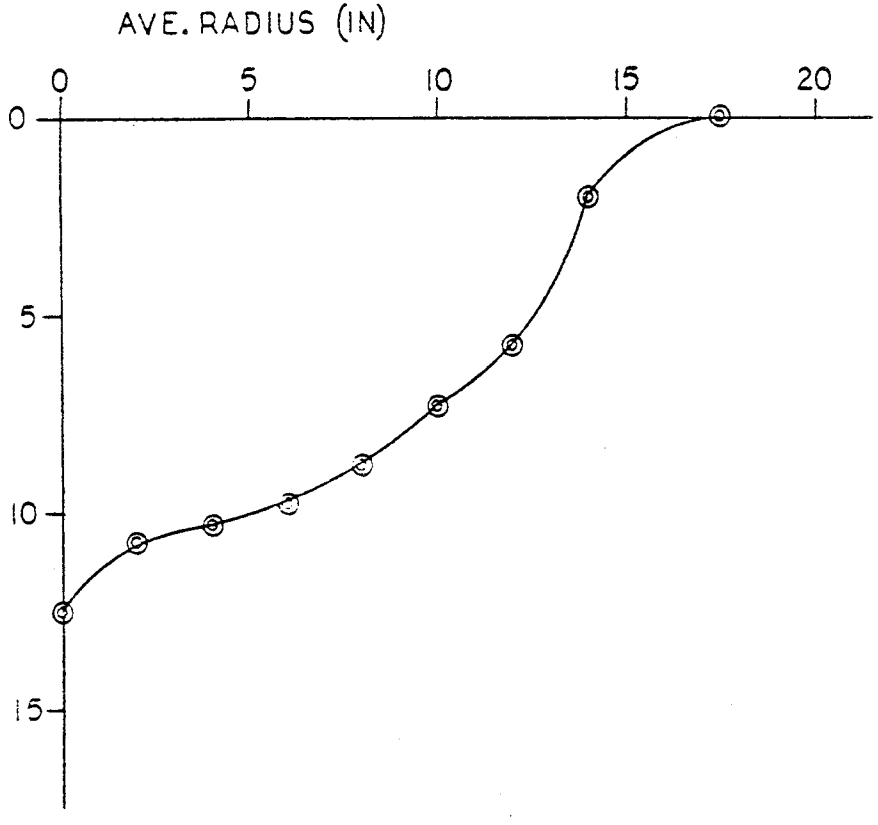

CONSTANTS	
HEIGHT OF NOZZLE	30"
BLAST DURATION	.79 SEC
LINE PRESSURE	1800 PSI
AVERAGE NOZZLE CHAMBER PRESSURE	711 PSI

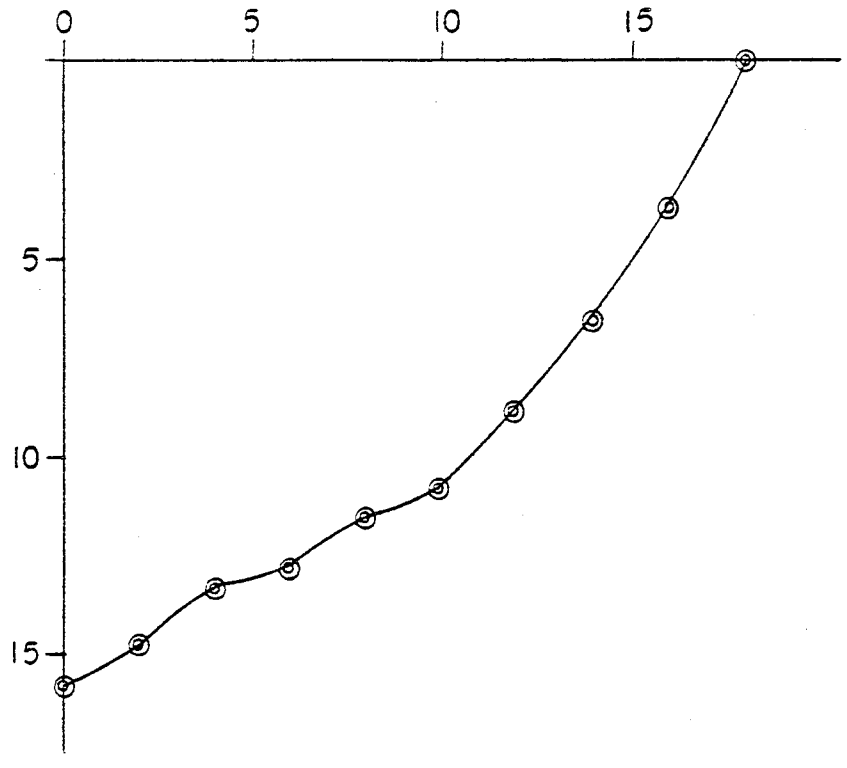

CONSTANTS	
HEIGHT OF NOZZLE	30"
BLAST DURATION	1.09 SEC
LINE PRESSURE	2800 PSI
AVERAGE NOZZLE CHAMBER PRESSURE	1113 PSI

SAND CRATER CONTOURS

FIGURE 16

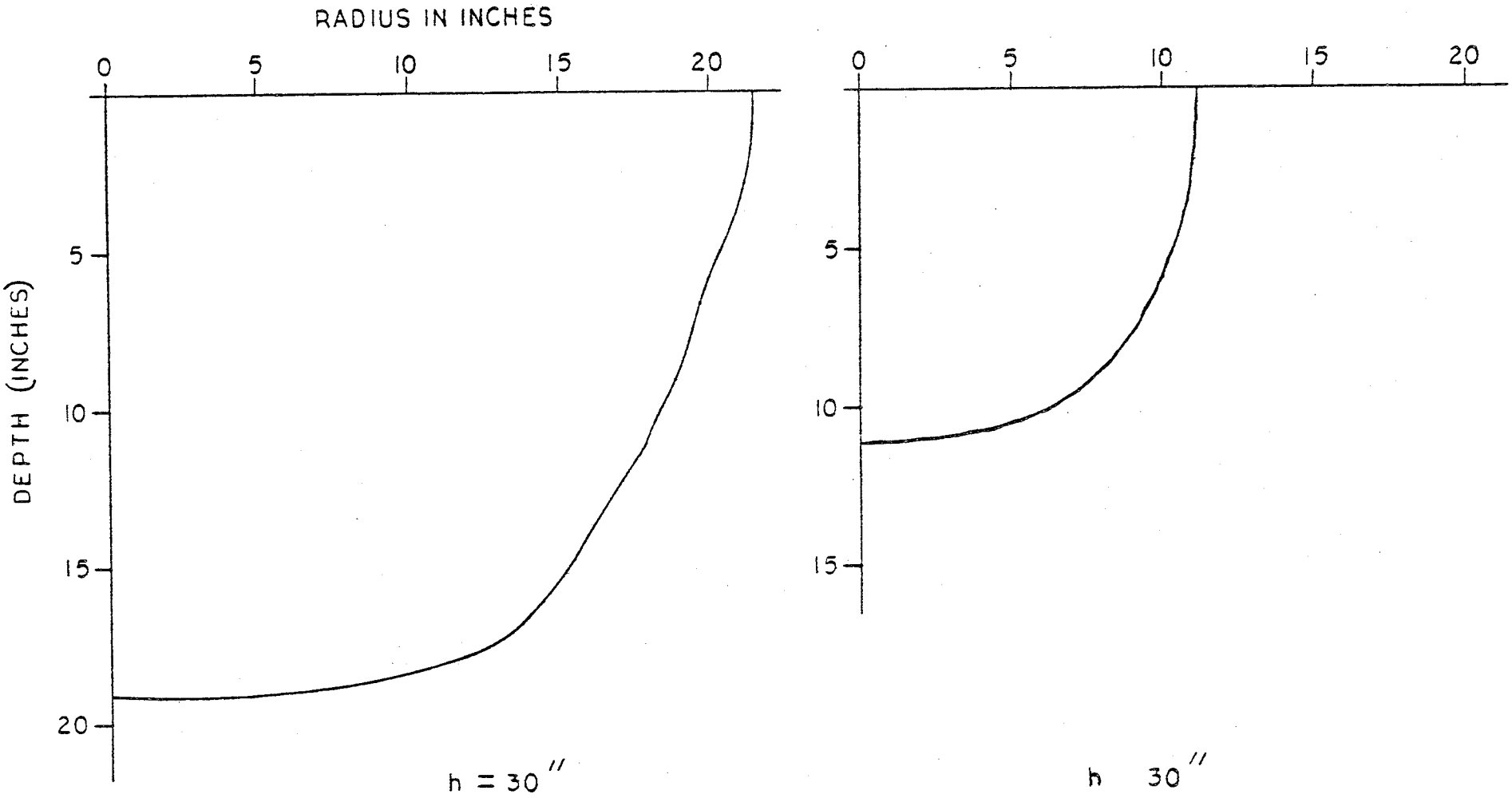

h = 30″
P_L = 2800 PSI
AVE P_C = 1750 PSI
Δ_T = 2.2 SEC.

h 30″
P_L = 1500 PSI
AVE P_C = 900 PSI
Δ_T = .8 SEC

CRATER CONTOURS, UNIFORM RED CLAY

FIGURE 17

OBLIQUE INCIDENCE DATA

JET VERTICAL

SOIL — SAND

P_L = 2800 AV. P_c = 1000 PSI

TIME .6 SEC

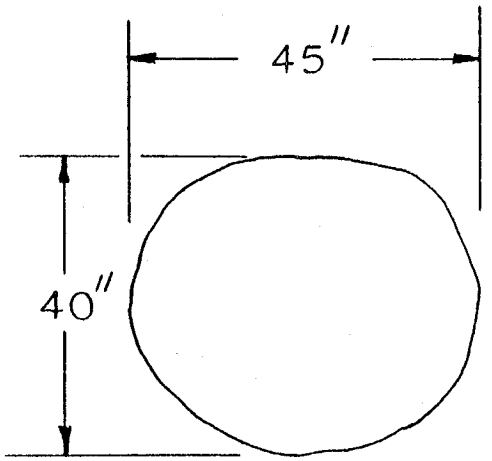

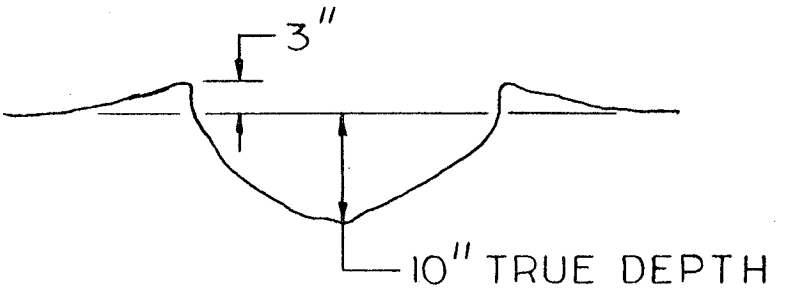

JET AT 5° W/VERTICAL

TIME .5 SEC

H = 16"

P_L = 2000 PSI

AV. P_c = 700 PSI

TRUE DEPTH 6"

RIM HT. 2"

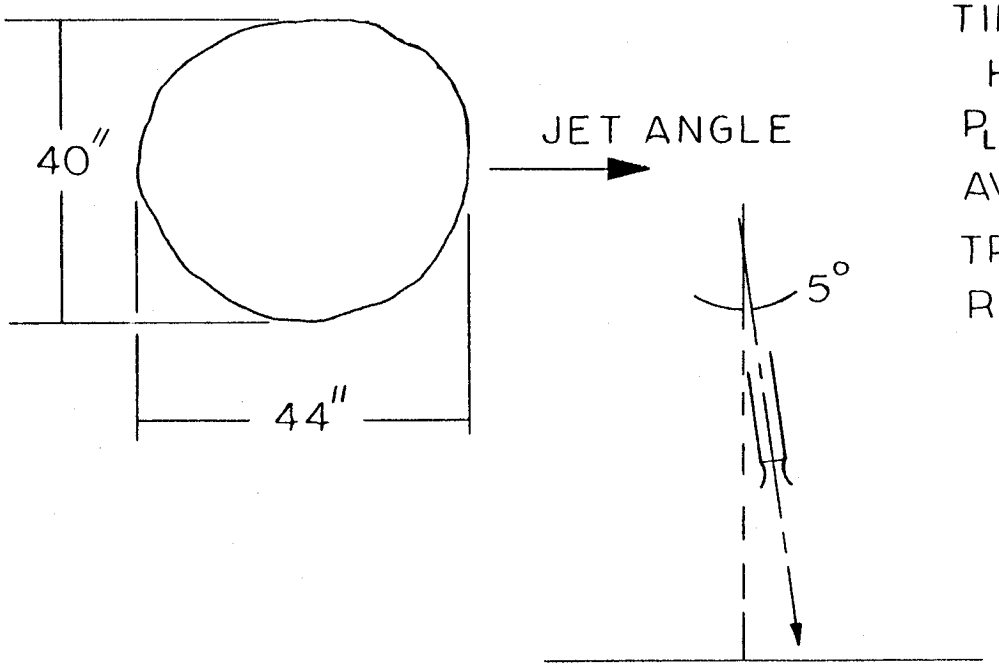

FIGURE 18

OBLIQUE INCIDENCE DATA

JET AT 10° W/VERTICAL

SOIL-SAND
H = 16″
P_L = 2800 PSI
AV. P_C = 800 PSI
TIME .5 SEC

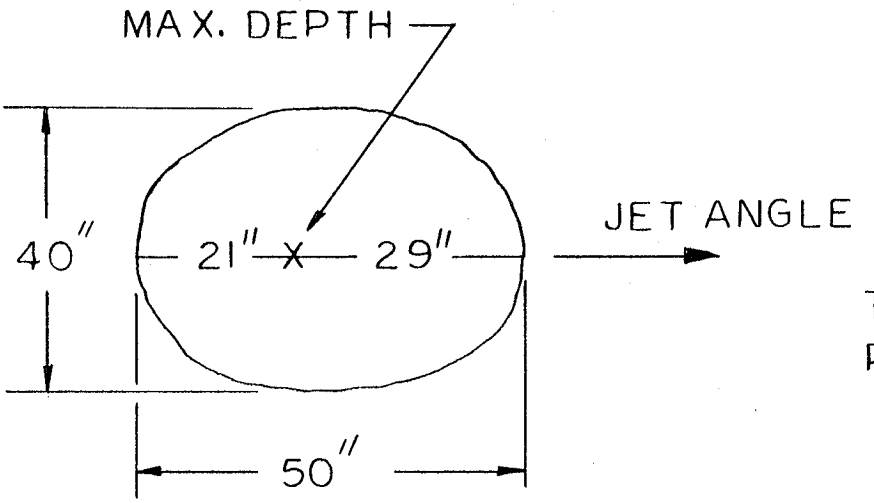

TRUE DEPTH 10.5″
RIM HEIGHT 3″

JET AT 20° W/VERTICAL

H = 16″
P_L = 2800 PSI
P_C = 1000 PSI

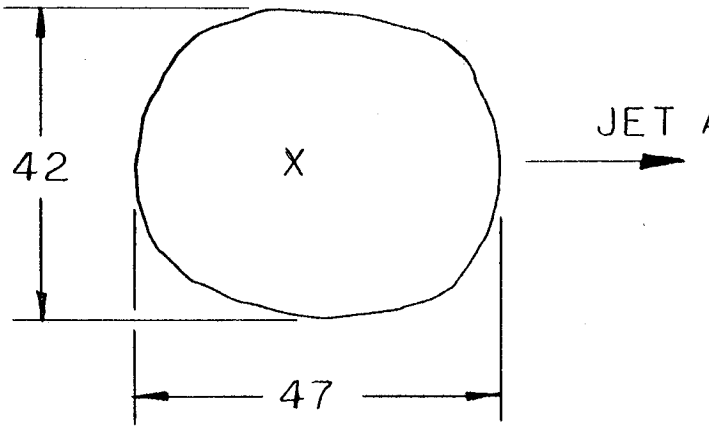

TRUE DEPTH 9″
RIM HEIGHT 4″

FIGURE 19

OBLIQUE INCIDENCE DATA

JET AT 40° W/VERTICAL

H=17″
P_L=2800 PSI
AV. P_C=1000 PSI
TIME=.6–.7 SEC

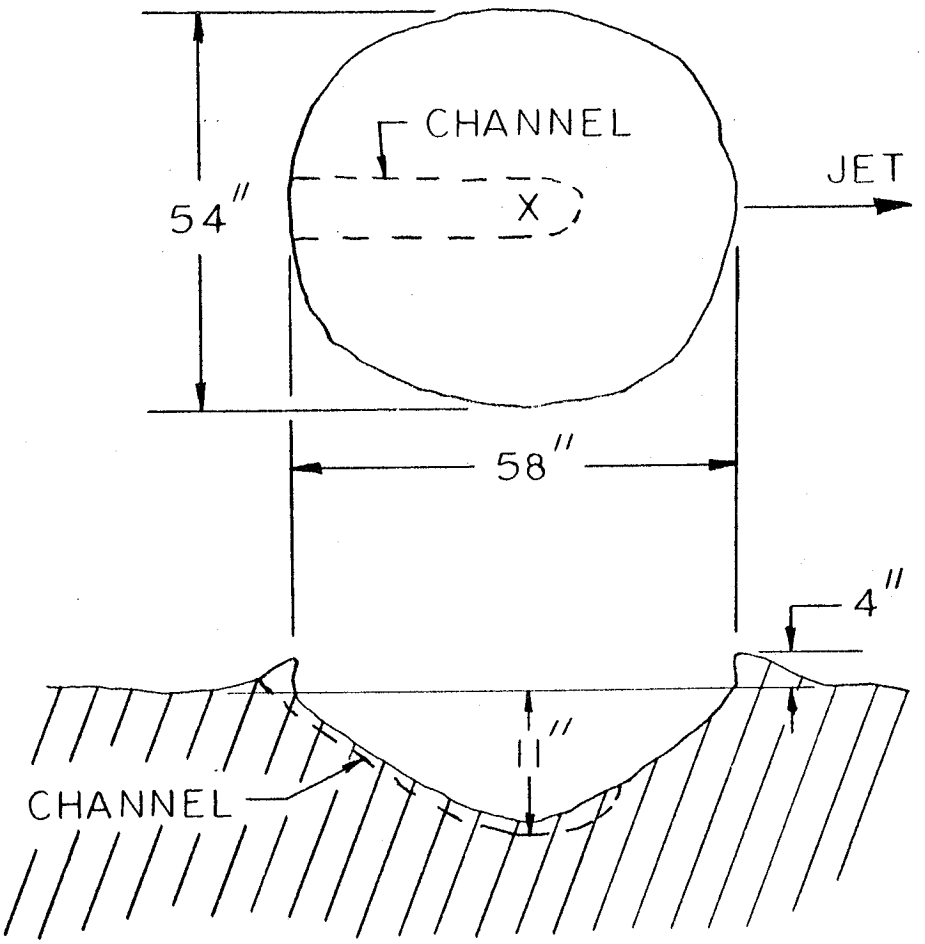

TRUE DEPTH 11″
RIM HEIGHT 4″

FIGURE 20

CRATERING BY MOVING NOZZLE
(SAND)

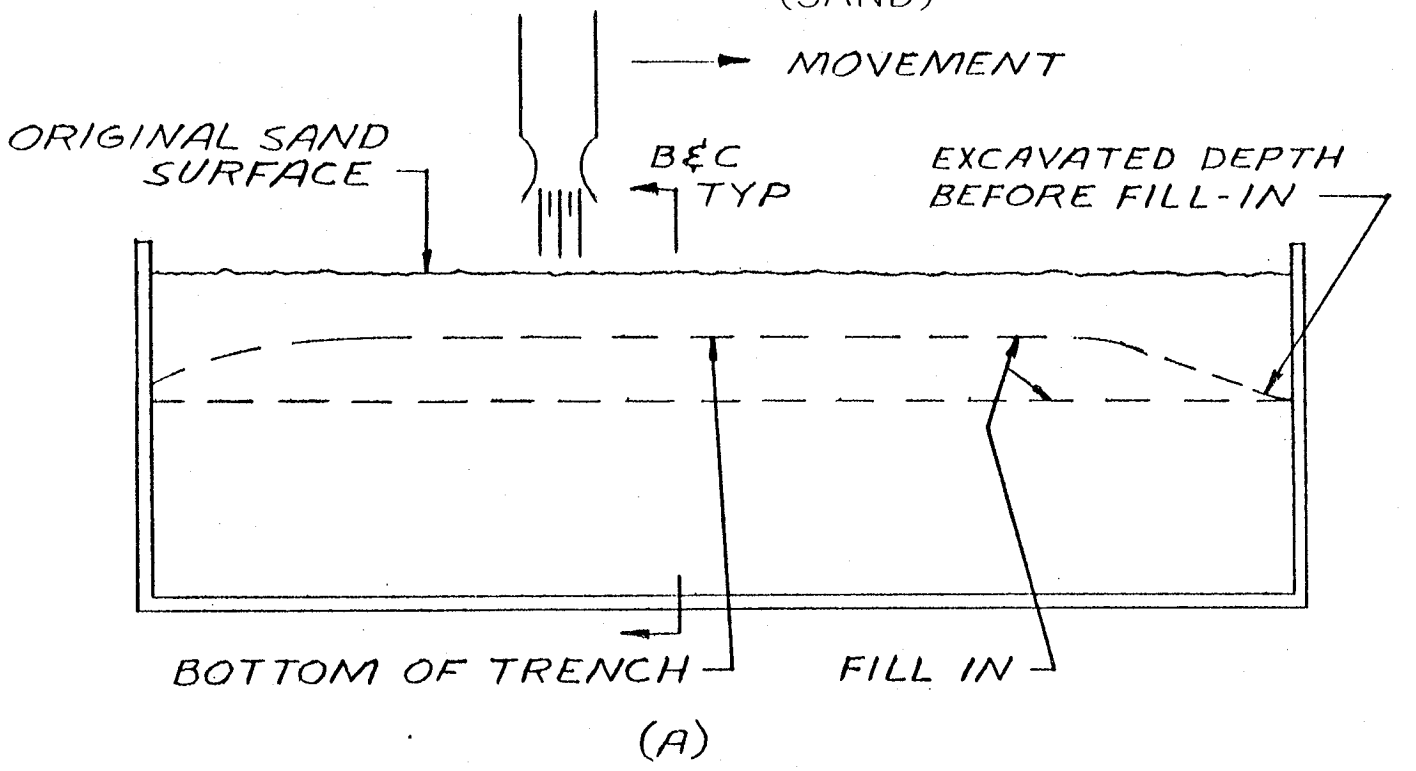

(A)

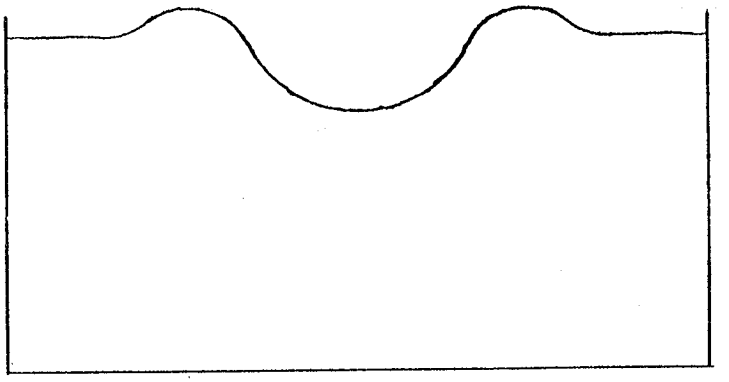

(B)

CROSS SECTION FOR LOW SURFACES PRESSURES

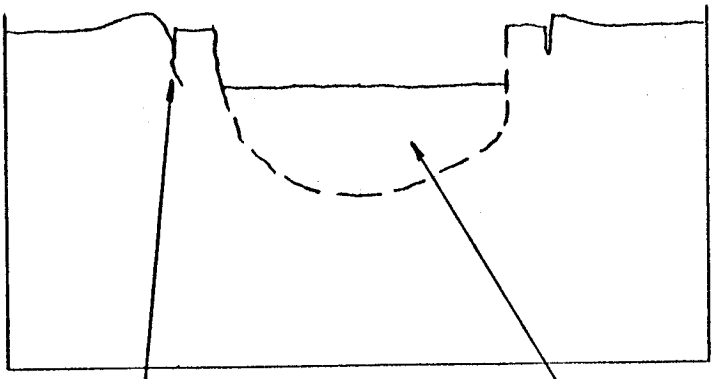

(C)

CROSS SECTION FOR HIGH SURFACE PRESSURES

FIGURE 21

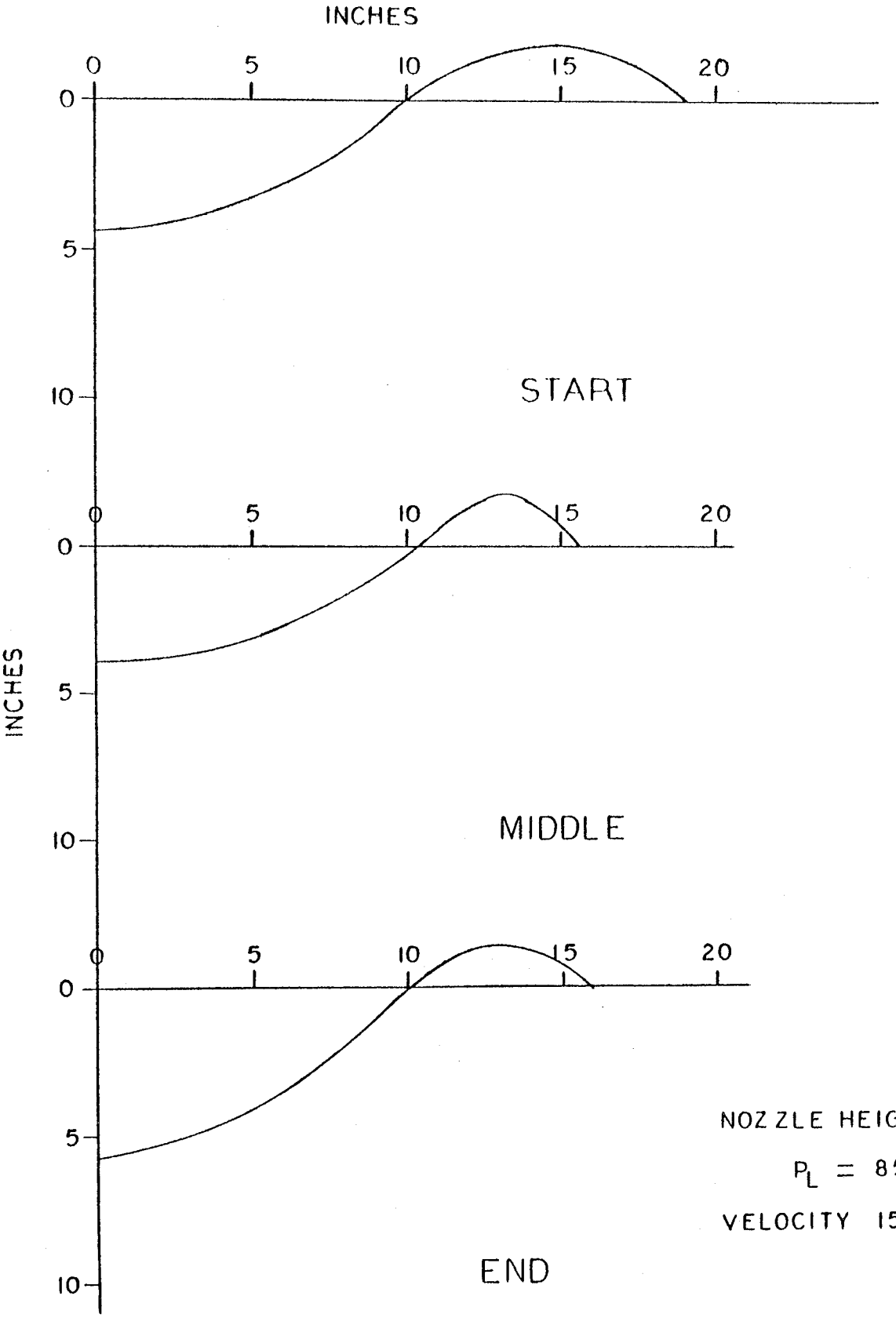

MOVING NOZZLE TRENCH CONTOURS (SAND)

FIGURE 22

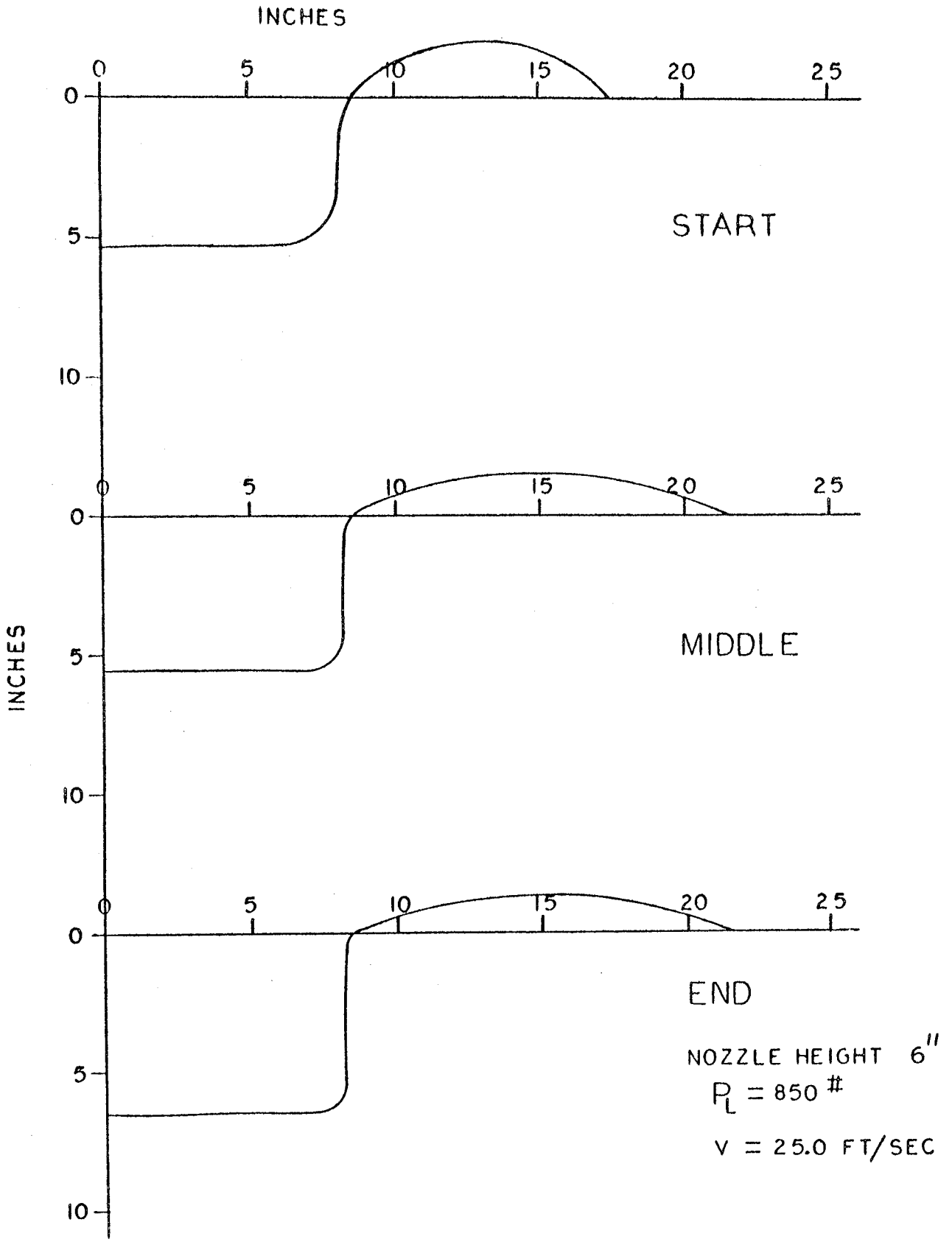

MOVING NOZZLE TRENCH CONTOURS (SAND)

FIGURE 23

SUMMARY -- COLD GAS, MOVING TEST (SAND)

THRUST 650 LBS.

Horizontal Velocity Ft/Sec	Nozzle Height Inches	Trench Depth Inches	Trench Width Inches
5	6	7	31
5	24	12	34
5	54	12.5	36
10	6	7	28
10	24	9	31
10	54	15	35
30	6	9	26
30	24	11.5	28
30	54	10	30

FIGURE 24

MOVING JET-COLD GAS-FIELD CLAY

(PROGRESS FROM LEFT TO RIGHT)

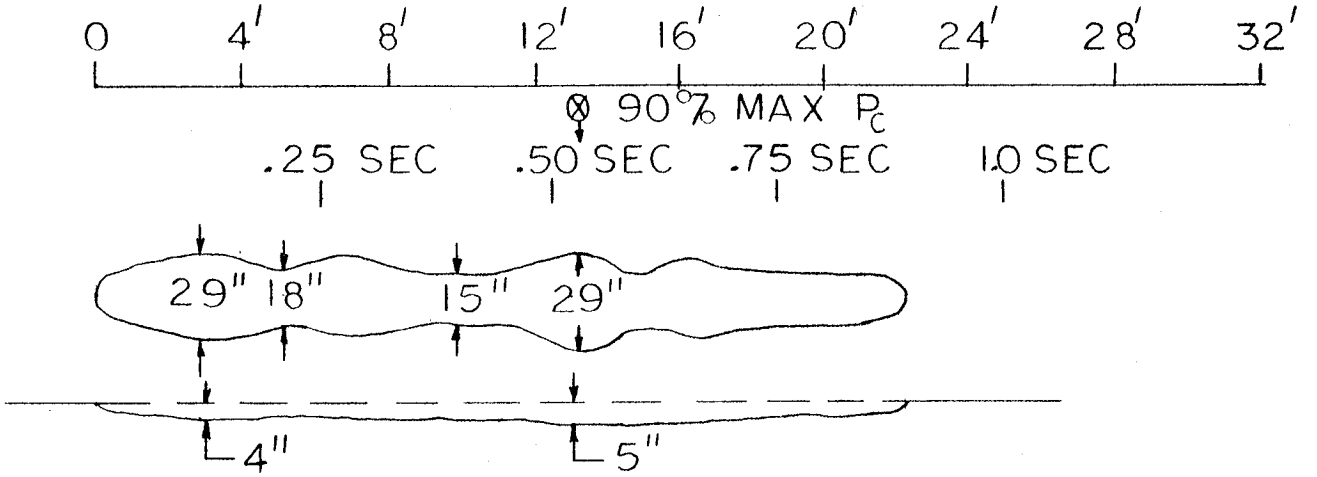

SPEED 25 FT/SEC P_c (MAX)=1800 PSI SOD-CLAY

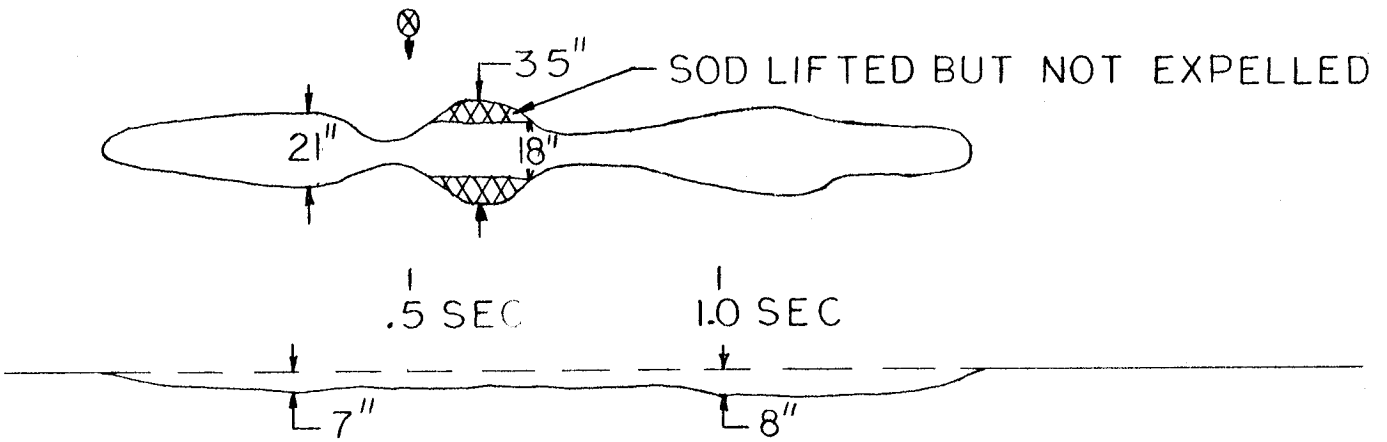

SPEED 17 FT/SEC P_c (MAX)=1800 PSI TERRAIN, SOD&CLAY

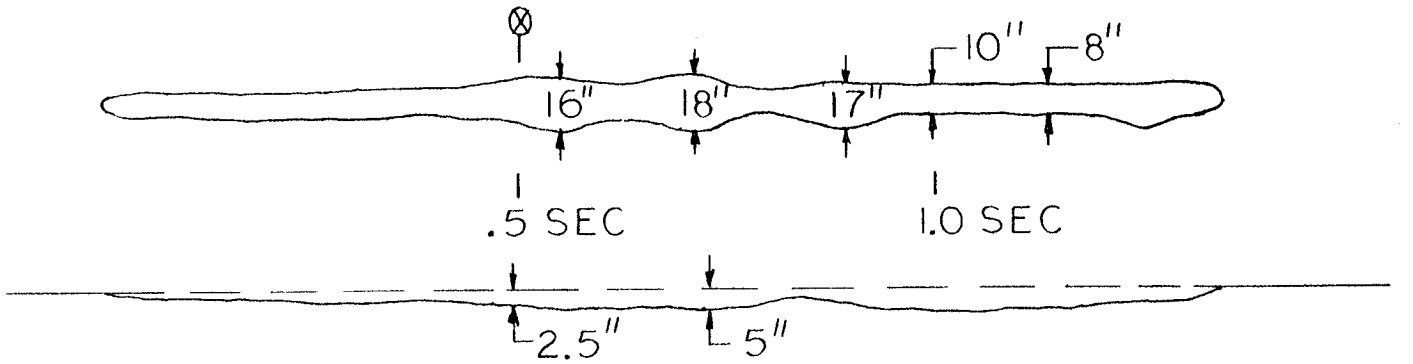

SPEED 23 FT/SEC P_c (MAX)=1400 PSI SOD-CLAY

FIGURE 25

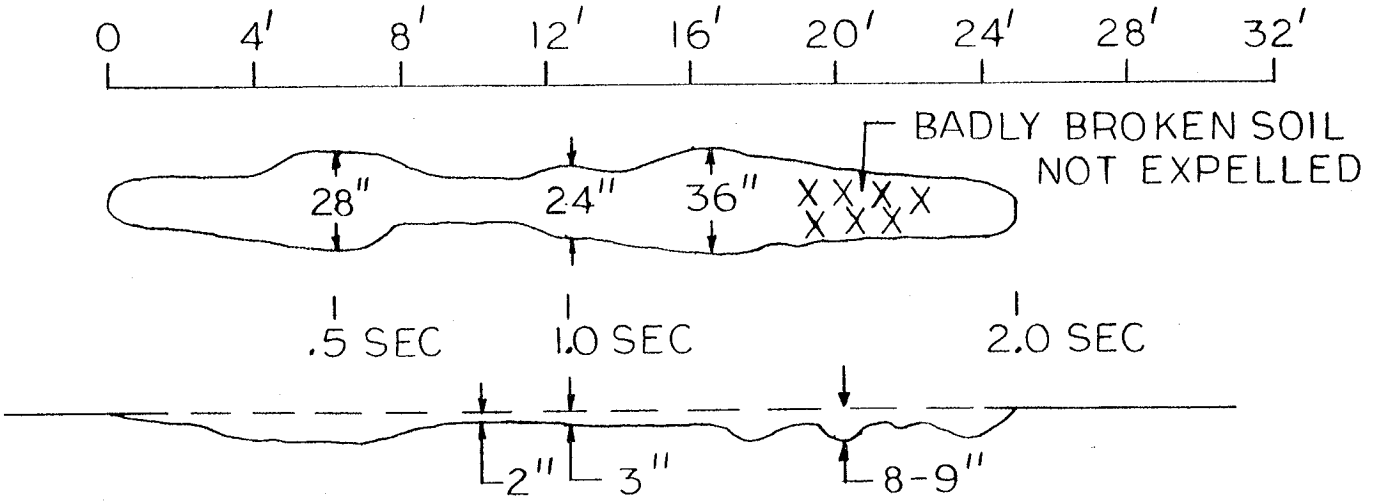

SPEED 12.5 FT/SEC, P_c (MAX)=1600 PSI SOD-CLAY

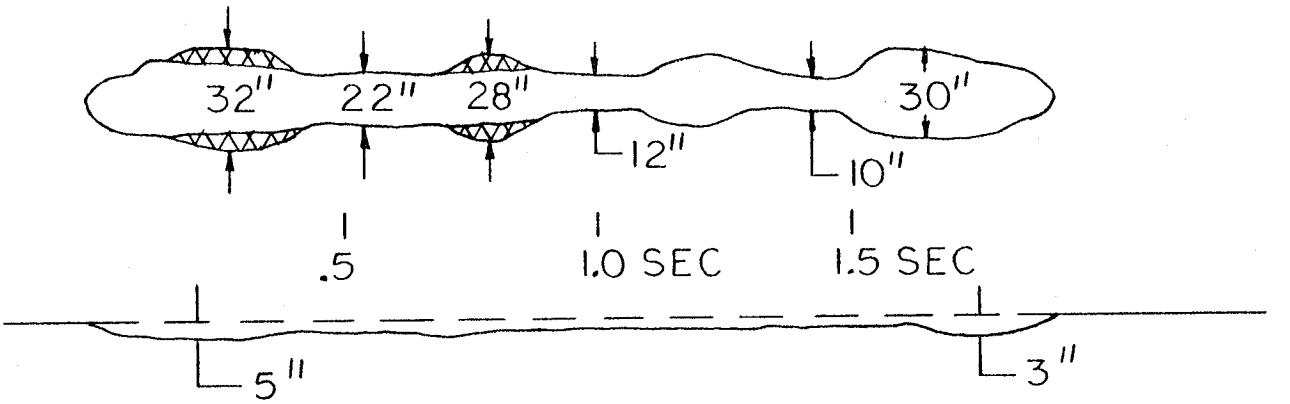

SPEED 14 FT SEC P_c (MAX)=1600 PSI SOD & CLAY

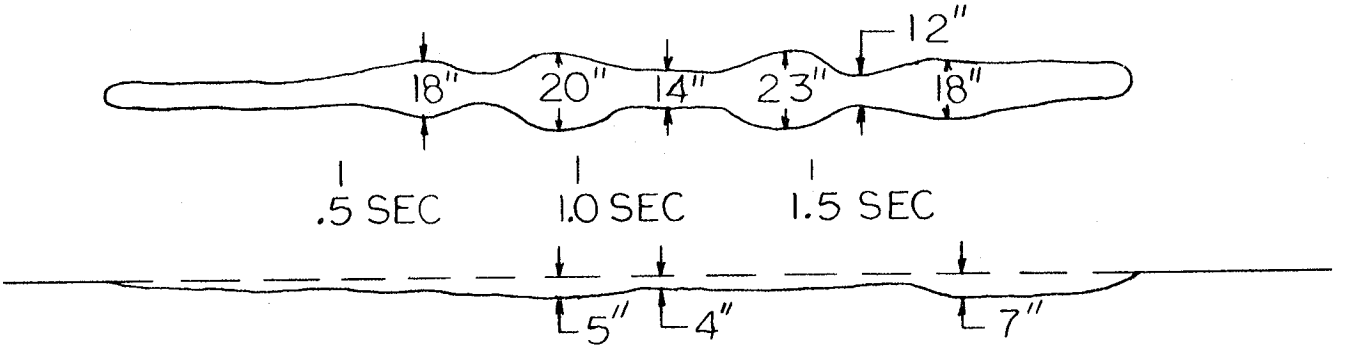

SPEED 13 FT/SEC P_c (MAX)=1600 PSI SOD & CLAY

MOVING JET- COLD GAS- FIELD CLAY

FIGURE 26

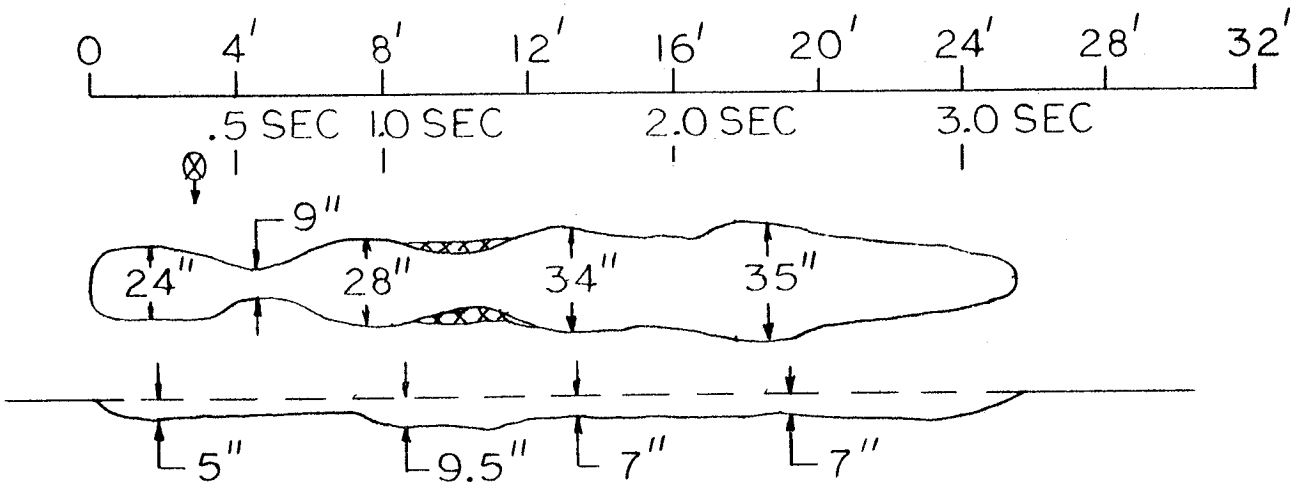

SPEED 8 FT SEC P_c (MAX)=1400 PSI SOD-CLAY

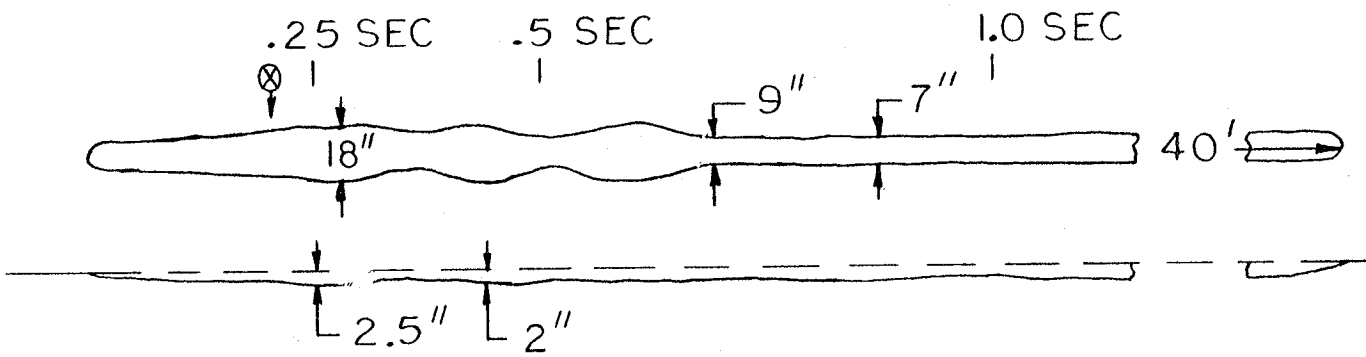

SPEED 25 FT/SEC P_c (MAX)=850 PSI SOD-CLAY
HARD PAN

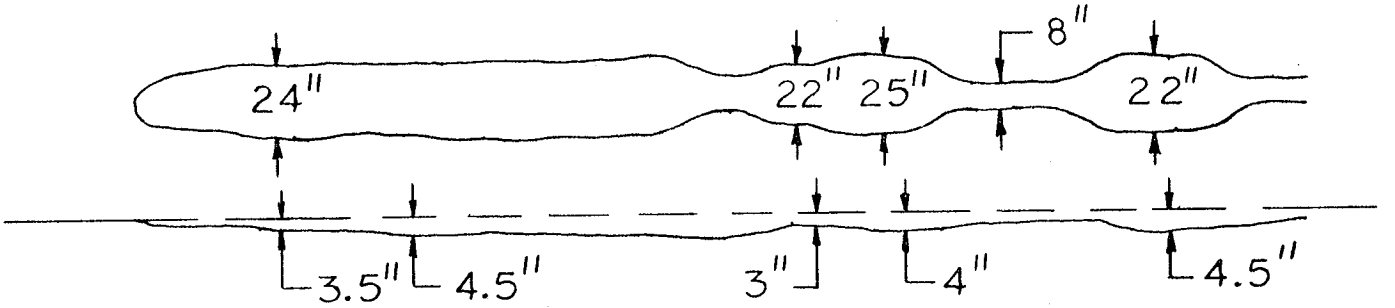

SPEED 12.5 FT/SEC P_c (MAX)=850 PSI SOD-CLAY
HARD PAN

MOVING JET-COLD GAS-FIELD CLAY

FIGURE 27

SUMMARY -- HOT FIRING TESTS

Soil	Average Horizontal Velocity Ft/Sec	Average Vertical Velocity Ft/Sec	Trench Dimensions Maximum Width Inches	Trench Dimensions Maximum Depth Inches
Sand	11.5	25.3	34	16
Sand	19.1	25.7	28	14
Sand	28.9	26.0	28	11
Earth	11.5	25.3	23	6
Earth	19.1	25.7	17	6
Earth	28.9	26.0	12	4
Sod	11.5	25.3	19	6
Sod	19.1	25.7	26	7
Sod	28.9	26.0	19	6
Sand	Stationary		(Dia.) 43	14
			Nozzle Height = 18"	

FIGURE 28

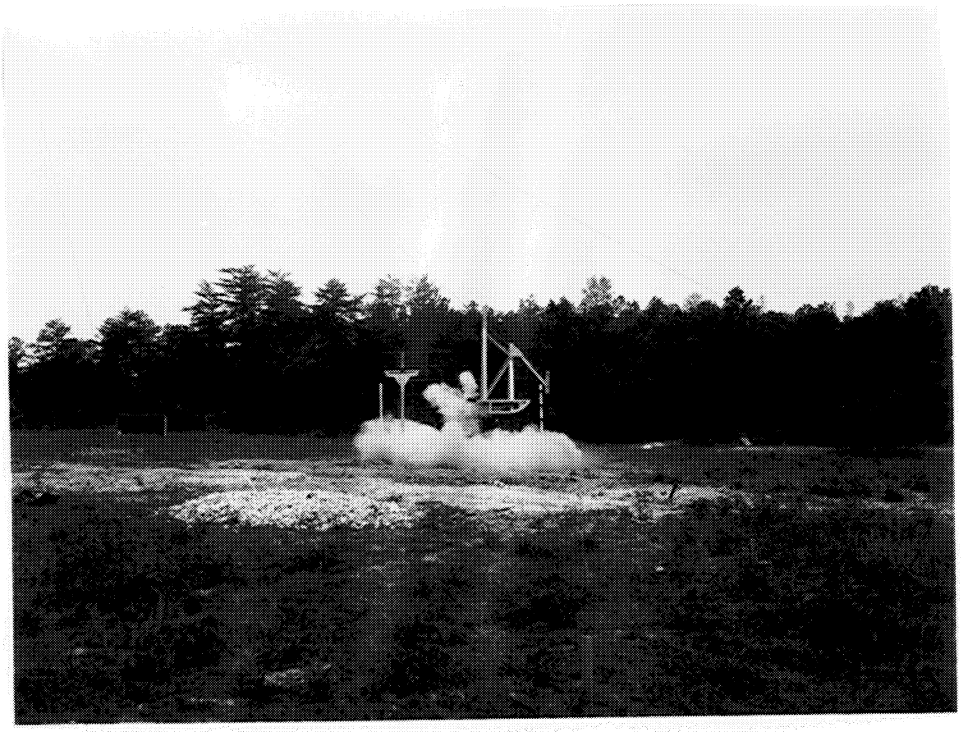

FIGURE 29

HOT FIRING TEST

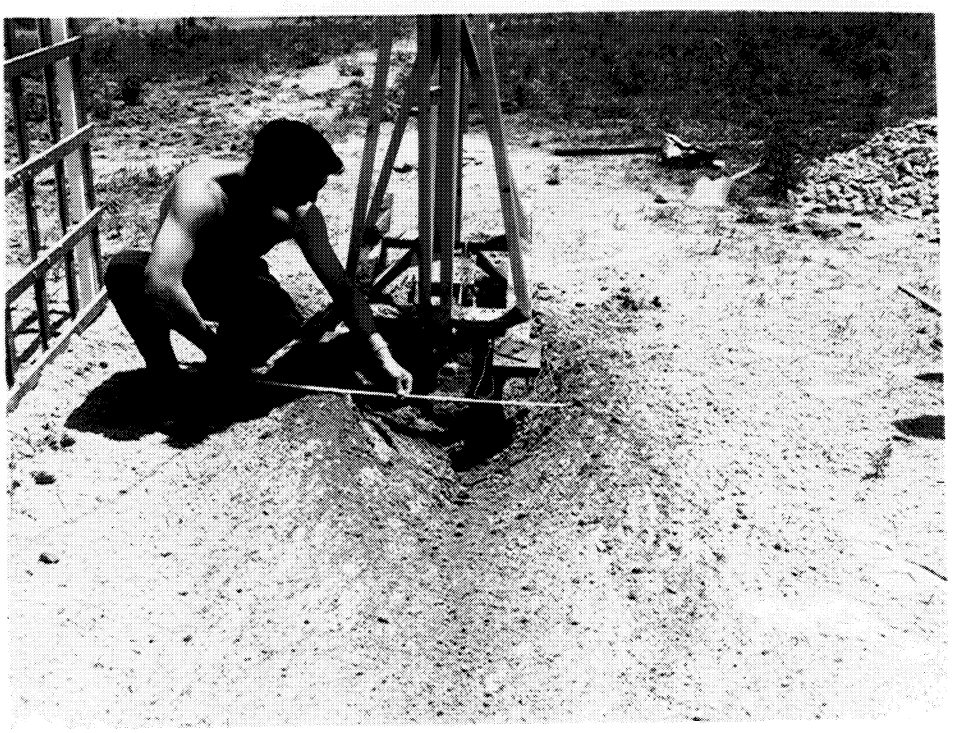

FIGURE 30

DESCENDING ROCKET - SAND

FIGURE 31

STATIONARY HOT FIRING - SAND

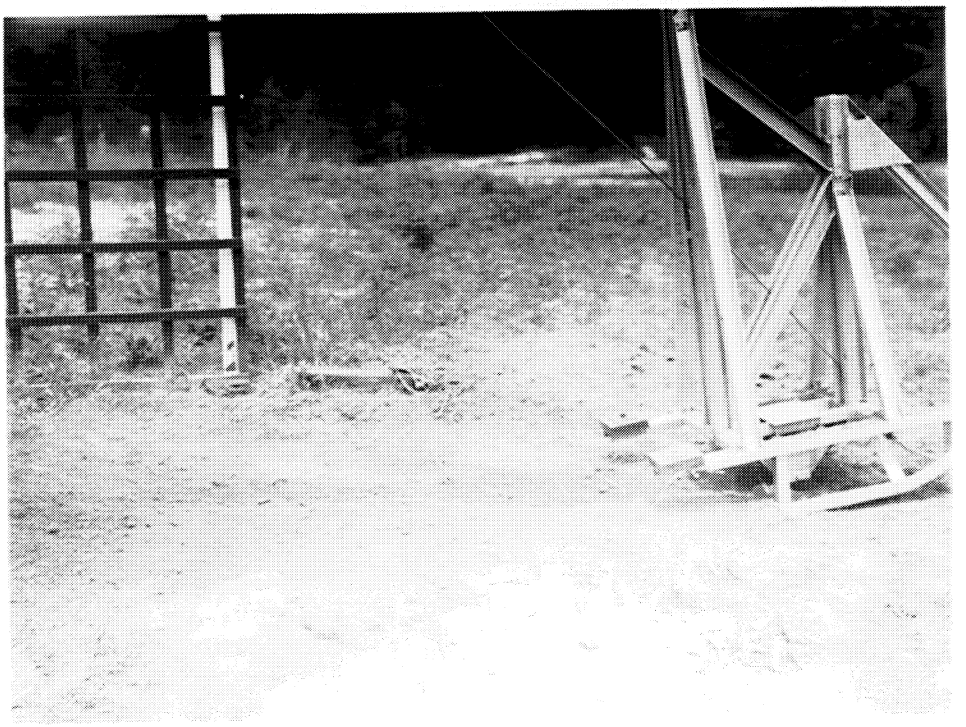

FIGURE 32

DESCENDING ROCKET - SOD COVERED EARTH

CABLE ANGLE 41° SHOT NO. 3 SOD IN DAMP EARTH

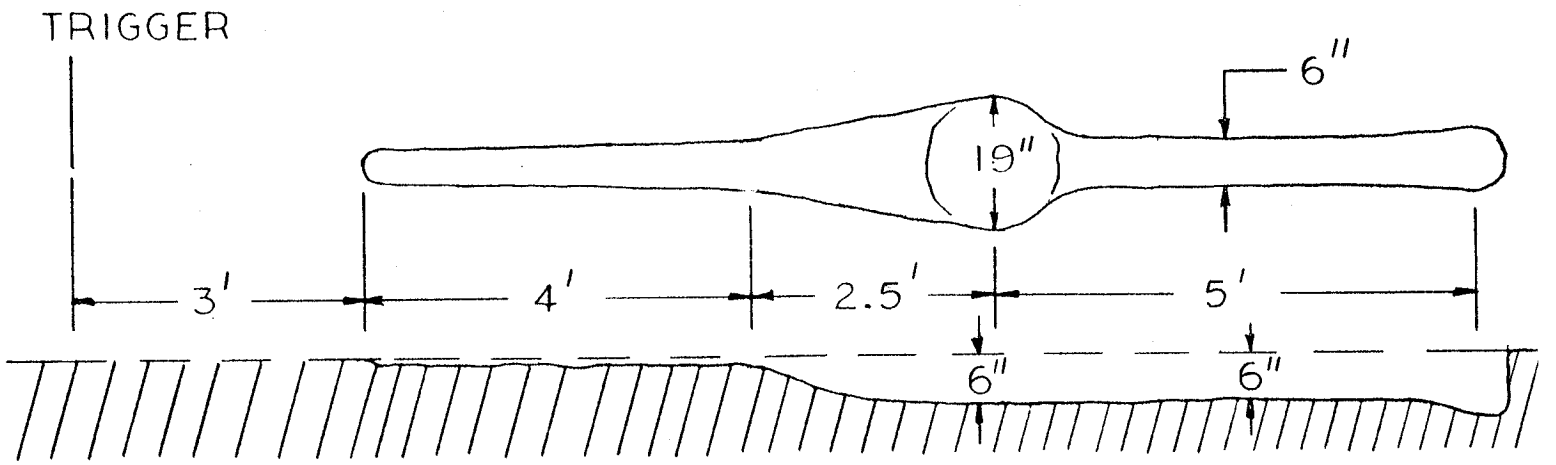

CABLE ANGLE 54° SHOT NO. 4 SOD IN DAMP EARTH

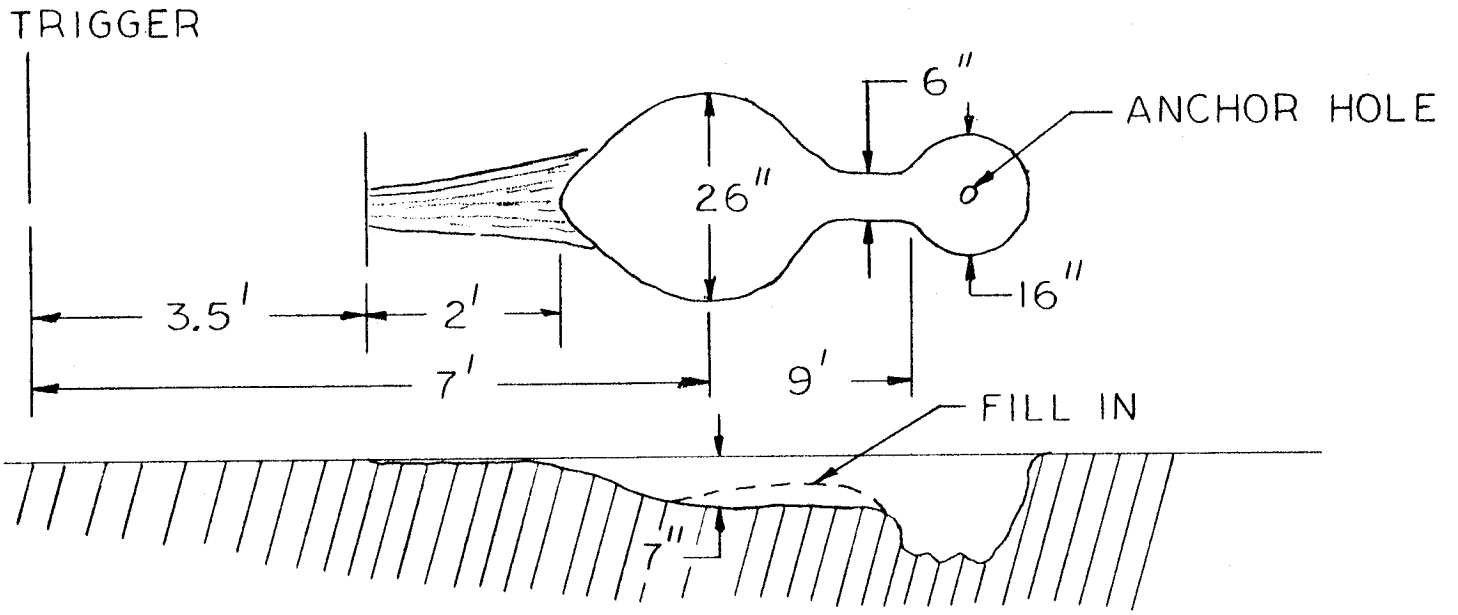

CABLE ANGLE 54° SHOT NO. 5 SCALPED EARTH

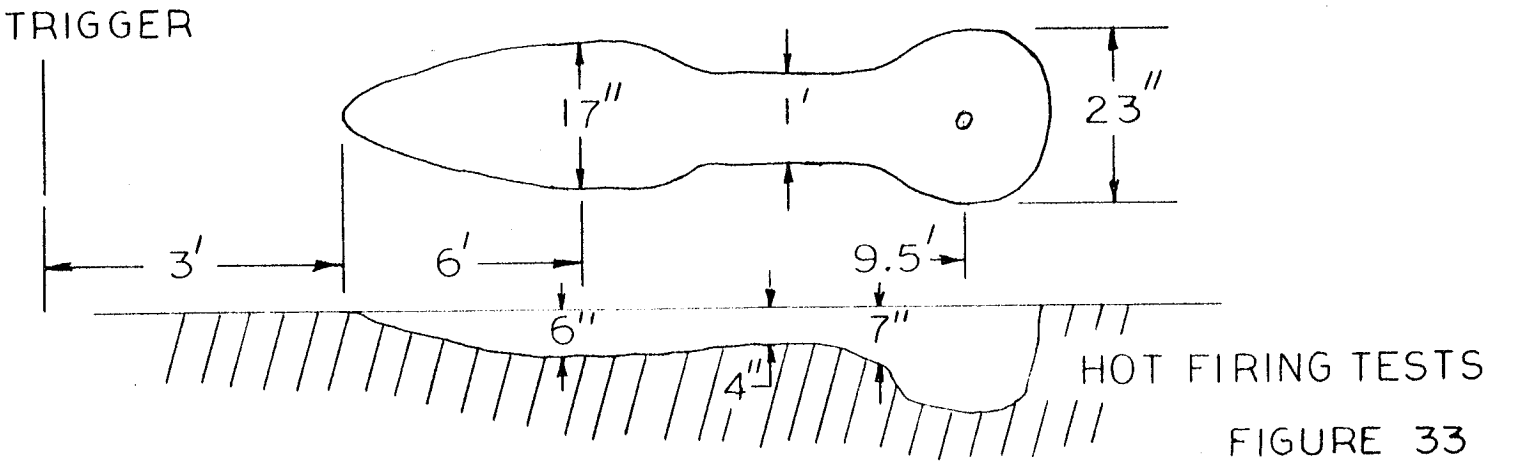

HOT FIRING TESTS

FIGURE 33

CABLE ANGLE 41°, SHOT NO. 6, SCALPED EARTH

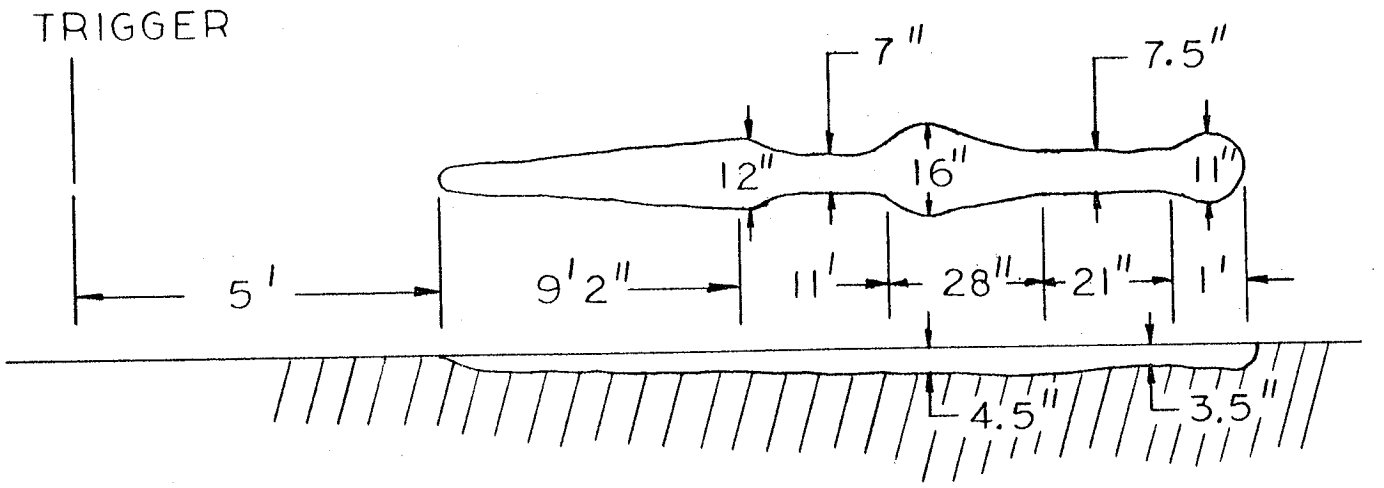

CABLE ANGLE 70°, SHOT NO. 9, SCALPED EARTH

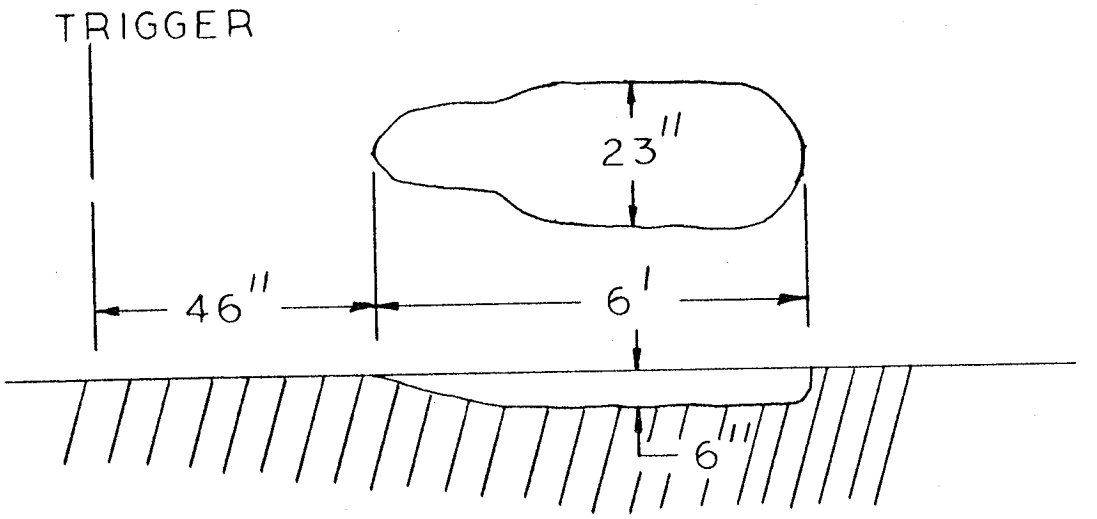

CABLE ANGLE 70°, SHOT NO. 10, SOD IN DAMP EARTH

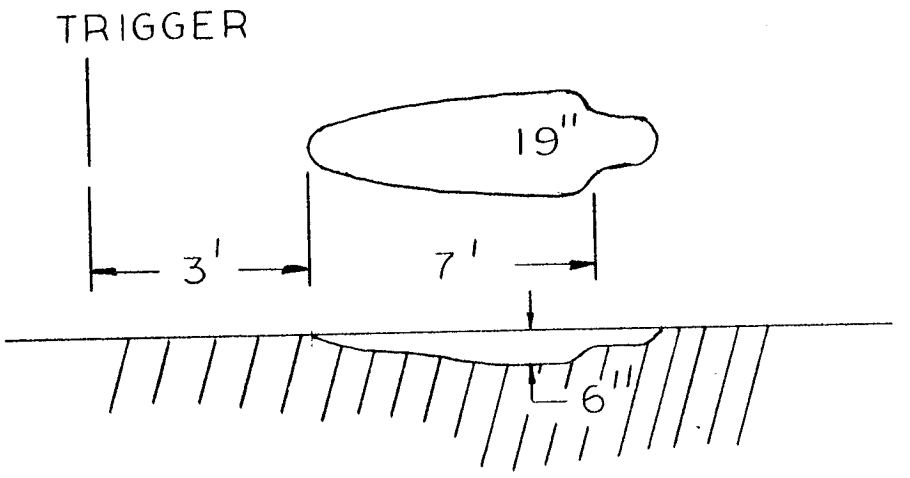

HOT FIRING TESTS

FIGURE 34

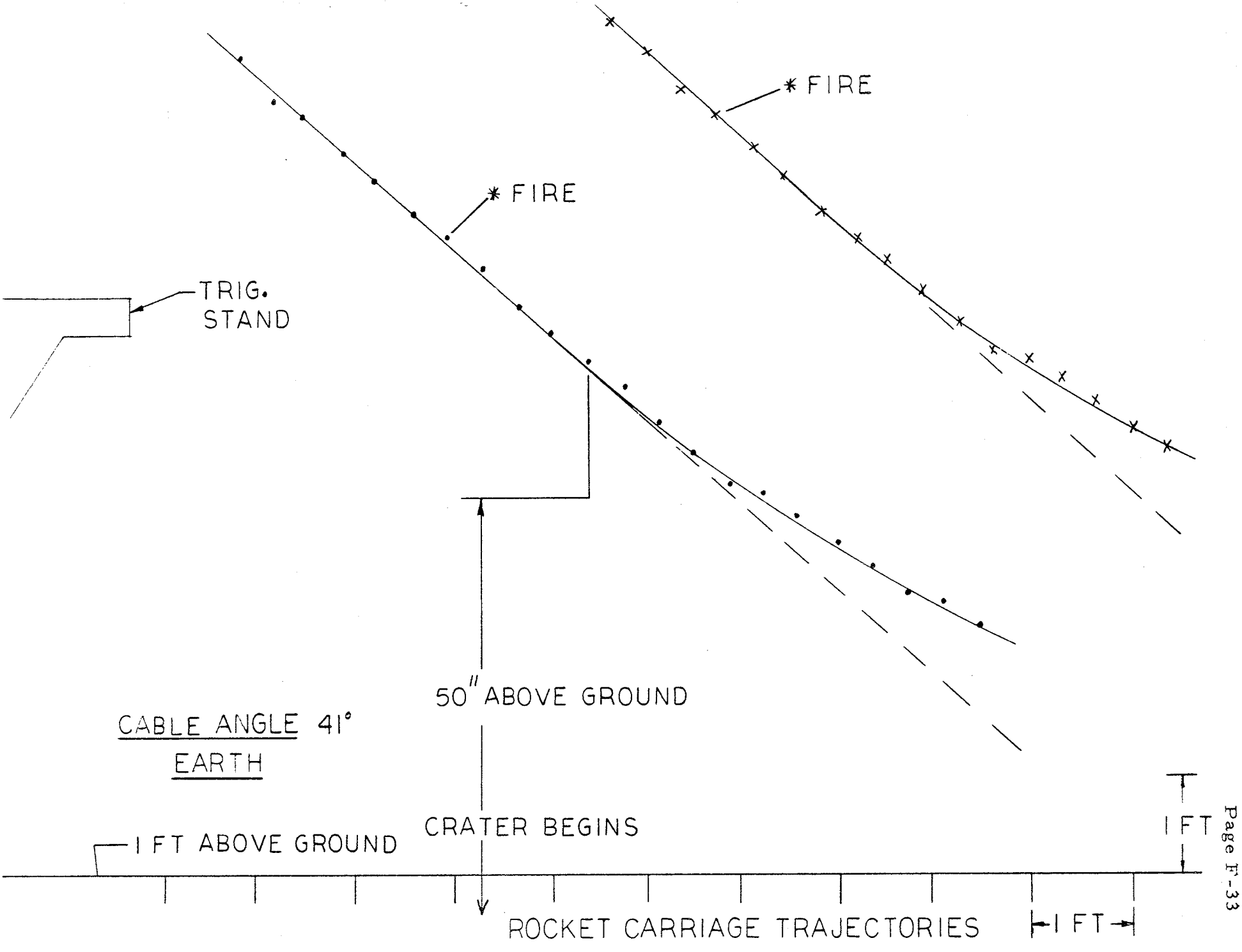
* FIRE
* FIRE
TRIG.
STAND
50" ABOVE GROUND
CABLE ANGLE 41°
EARTH
CRATER BEGINS
1 FT ABOVE GROUND
1 FT
ROCKET CARRIAGE TRAJECTORIES
1 FT

FIGURE 35

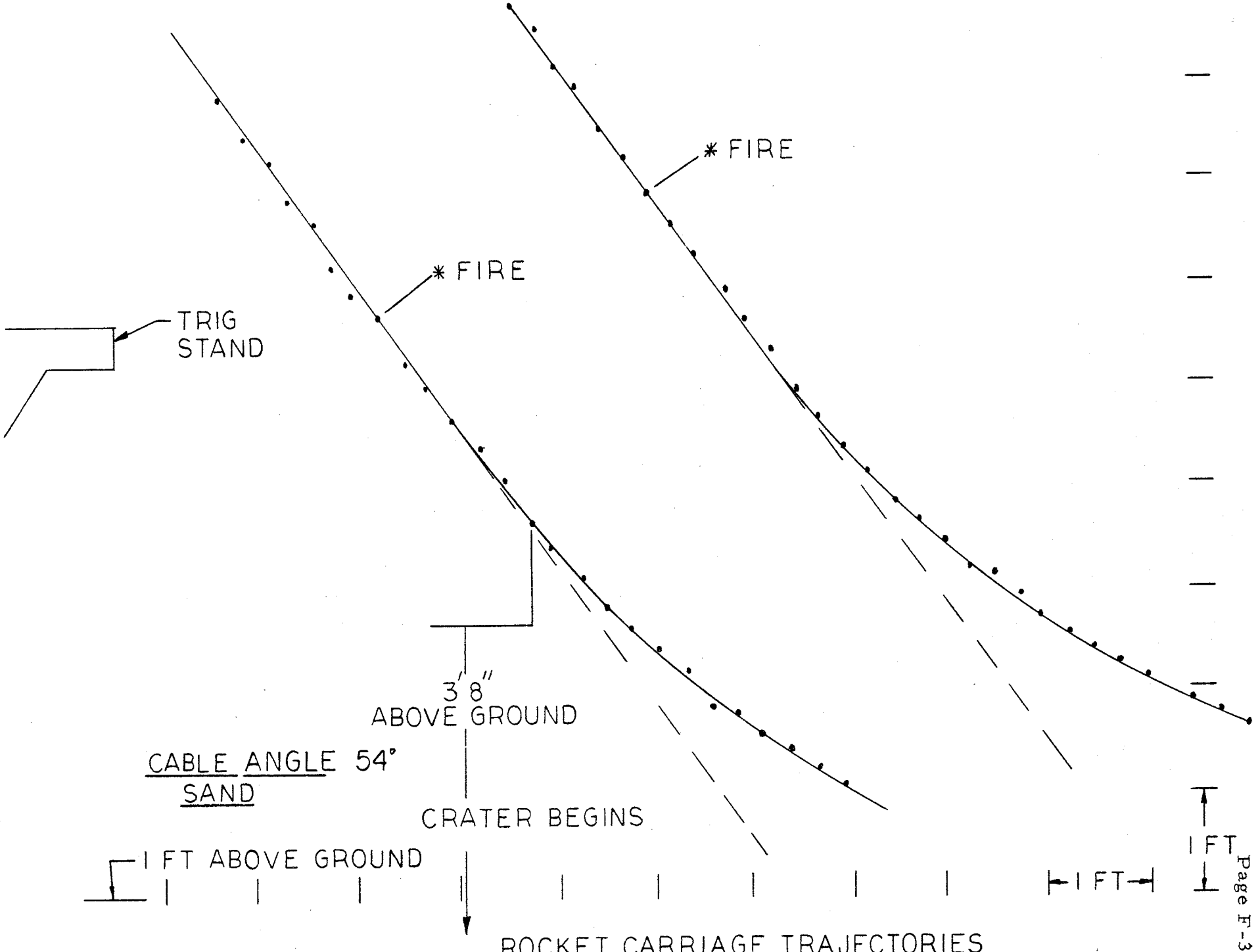
* FIRE
* FIRE
TRIG STAND
3' 8"
ABOVE GROUND
CABLE ANGLE 54°
SAND
CRATER BEGINS
1 FT ABOVE GROUND
1 FT
1 FT
ROCKET CARRIAGE TRAJECTORIES

FIGURE 36

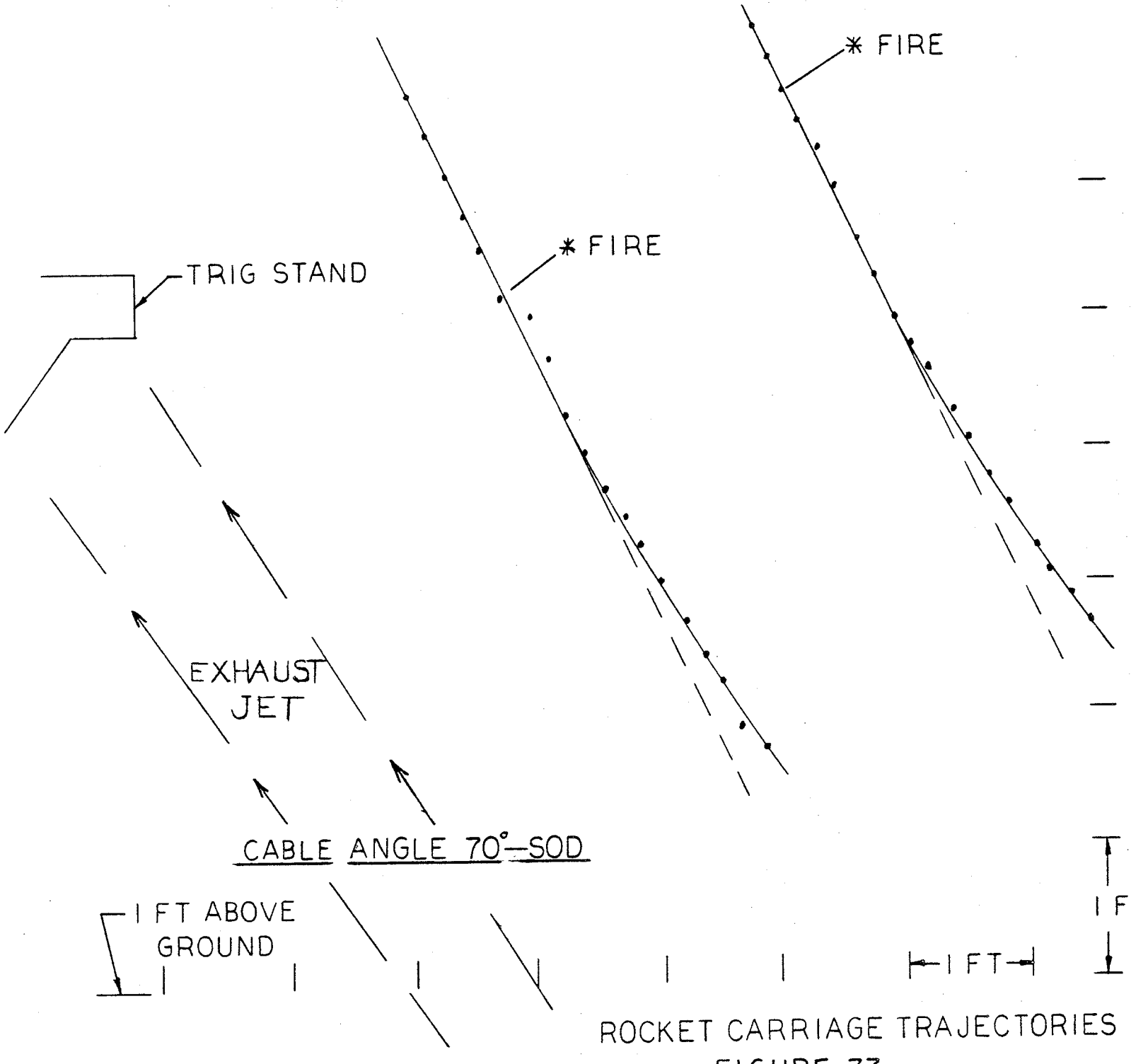

ROCKET CARRIAGE TRAJECTORIES
FIGURE 37

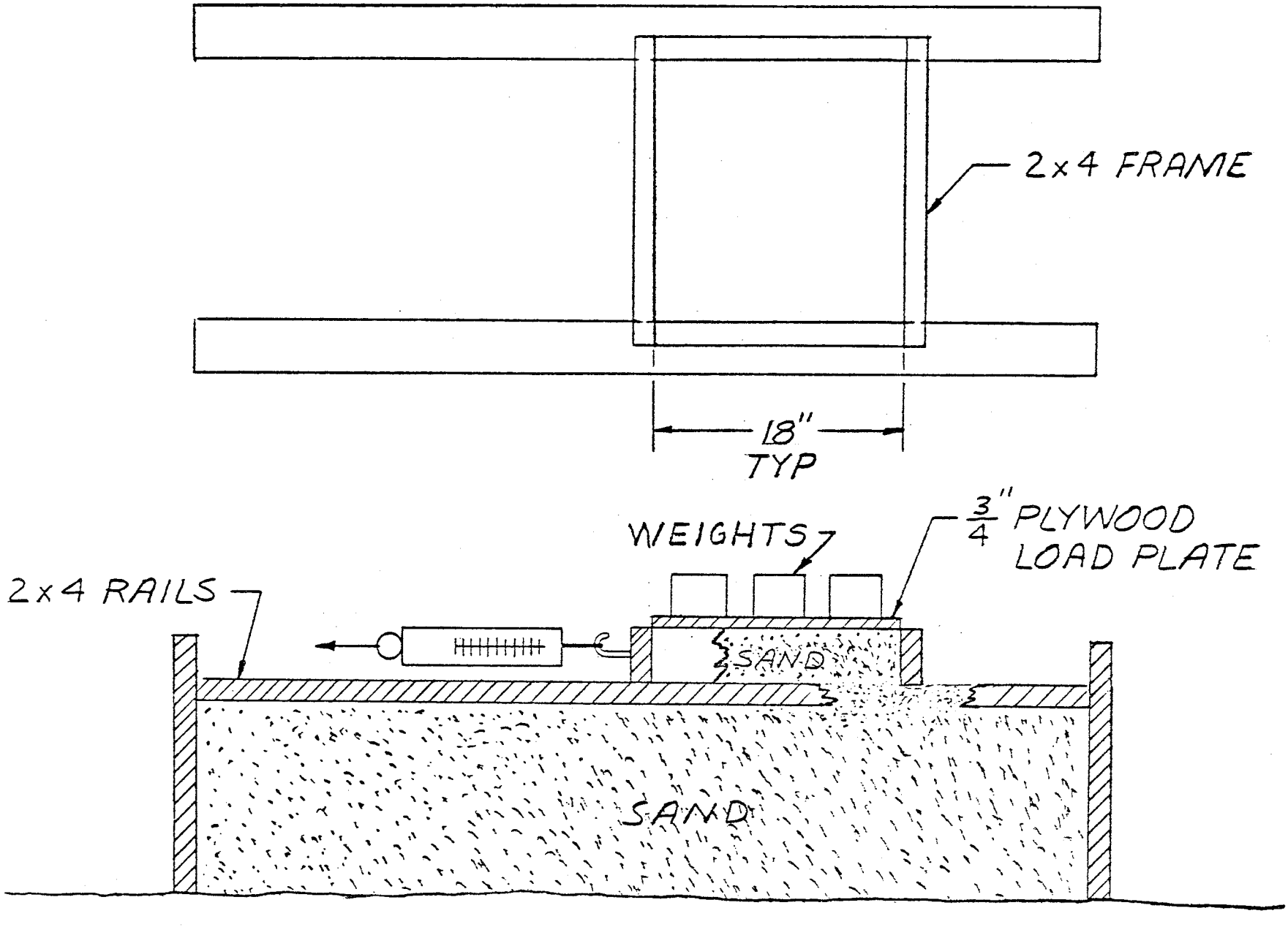

SHEAR TEST APPARATUS

FIGURE 38

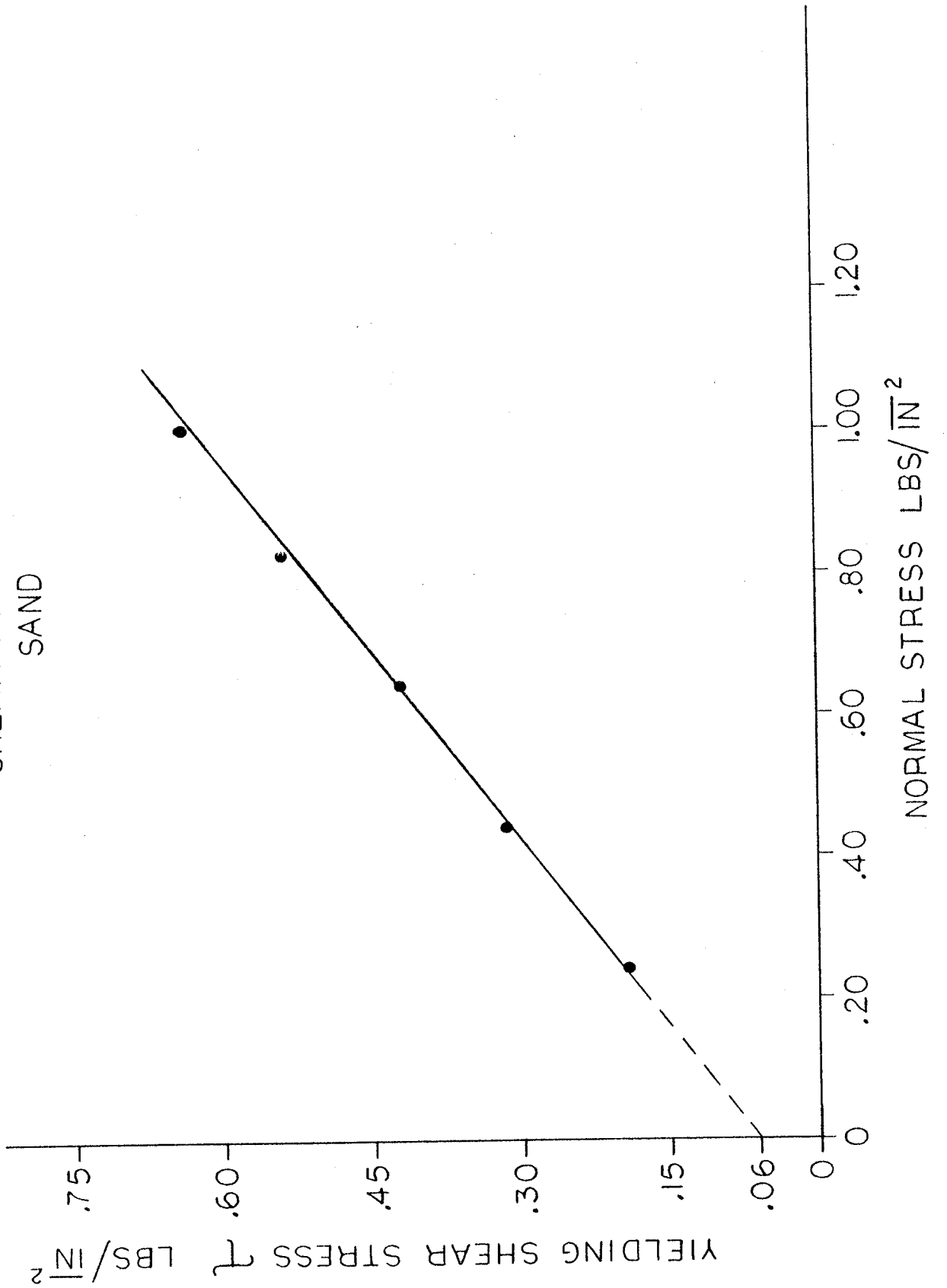
SHEAR TEST DATA
SAND
YIELDING SHEAR STRESS τ LBS/IN²
.75
.60
.45
.30
.15
.06
0
0
.20
.40
.60
.80
1.00
1.20
NORMAL STRESS LBS/IN²

FIGURE 39

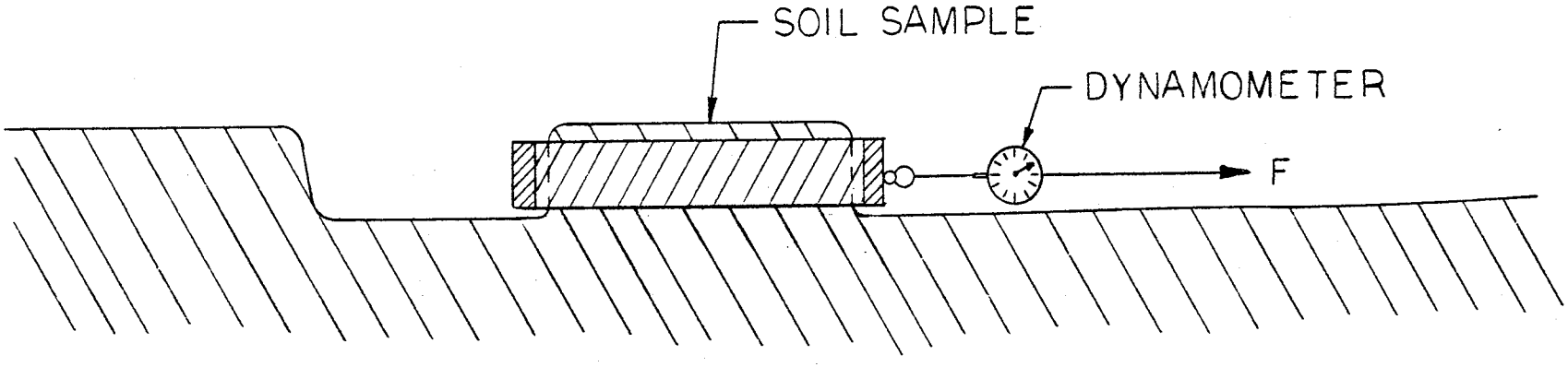

GENERAL ARRANGEMENT OF APPARATUS FOR SOIL SHEAR TEST IN FIELD

FIGURE 40

GRAIN SIZE DISTRIBUTION CURVE

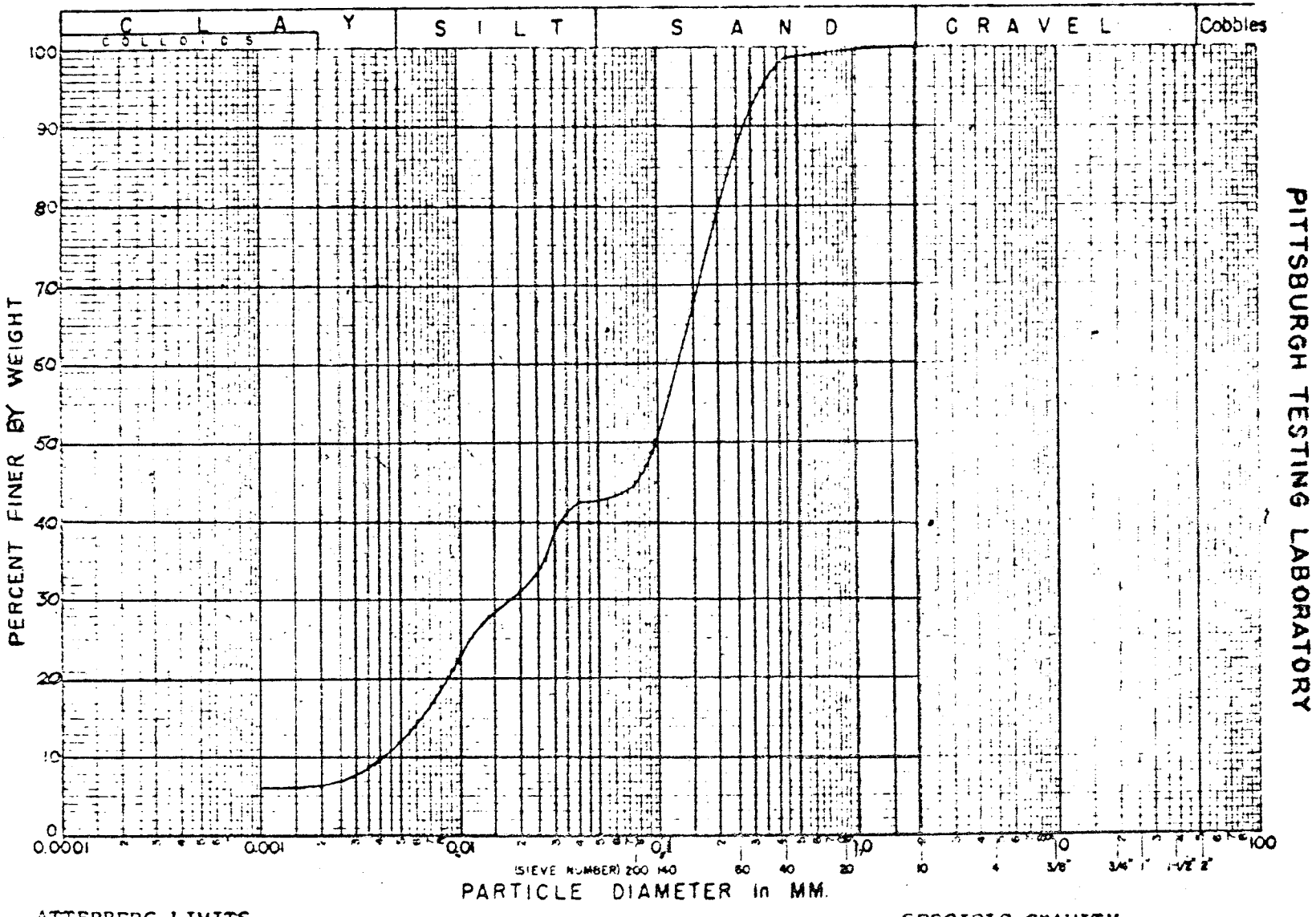

PITTSBURGH TESTING LABORATORY

ATTERBERG LIMITS

Non-Plastic

MOISTURE CONTENT %
(AS RECEIVED)

6.2

SPECIFIC GRAVITY

2.591

Figure 41

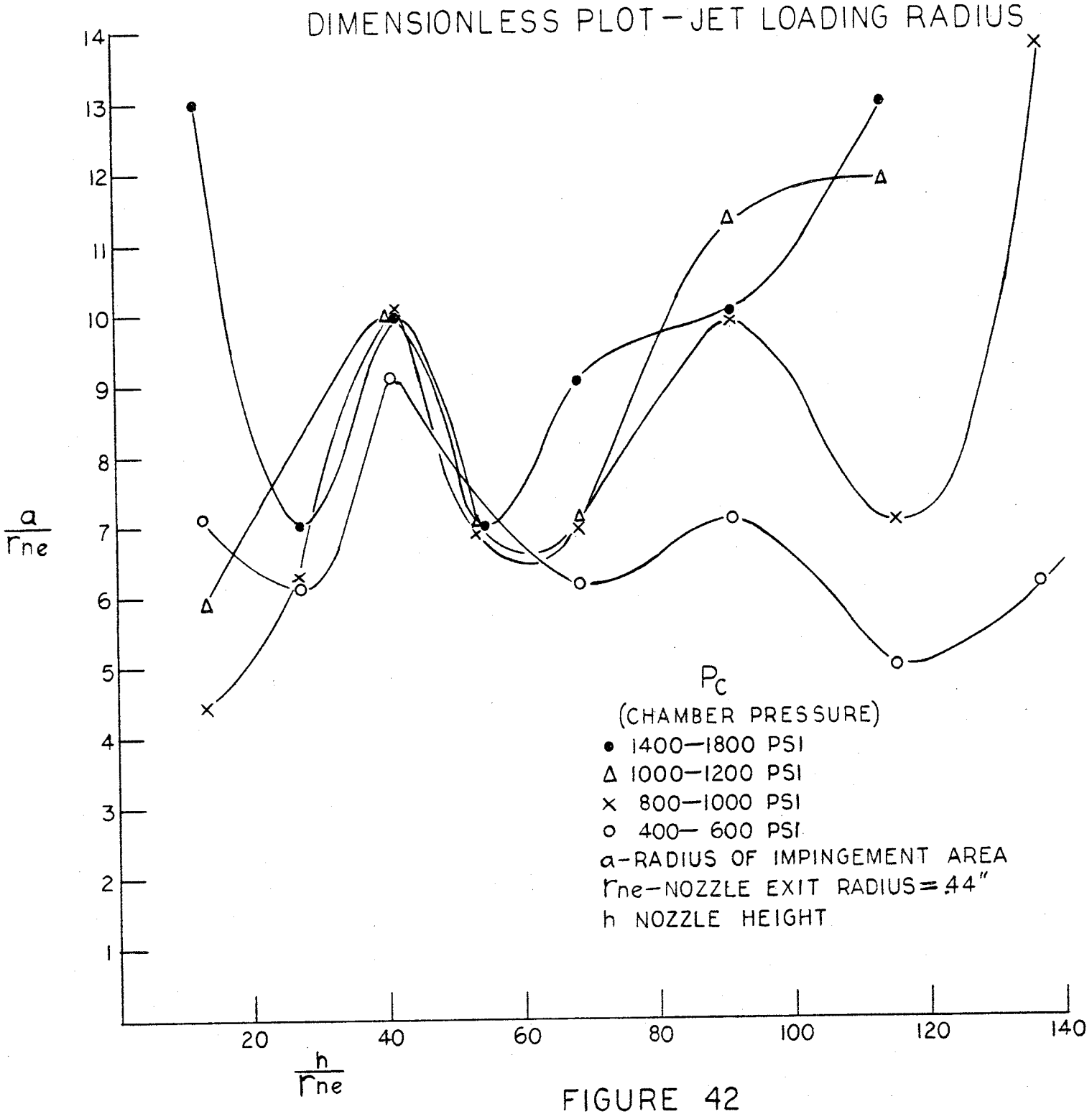
DIMENSIONLESS PLOT – JET LOADING RADIUS
a/rne
h/rne
Pc
(CHAMBER PRESSURE)
• 1400–1800 PSI
Δ 1000–1200 PSI
× 800–1000 PSI
o 400– 600 PSI
a-RADIUS OF IMPINGEMENT AREA
rne-NOZZLE EXIT RADIUS=.44"
h NOZZLE HEIGHT

FIGURE 42

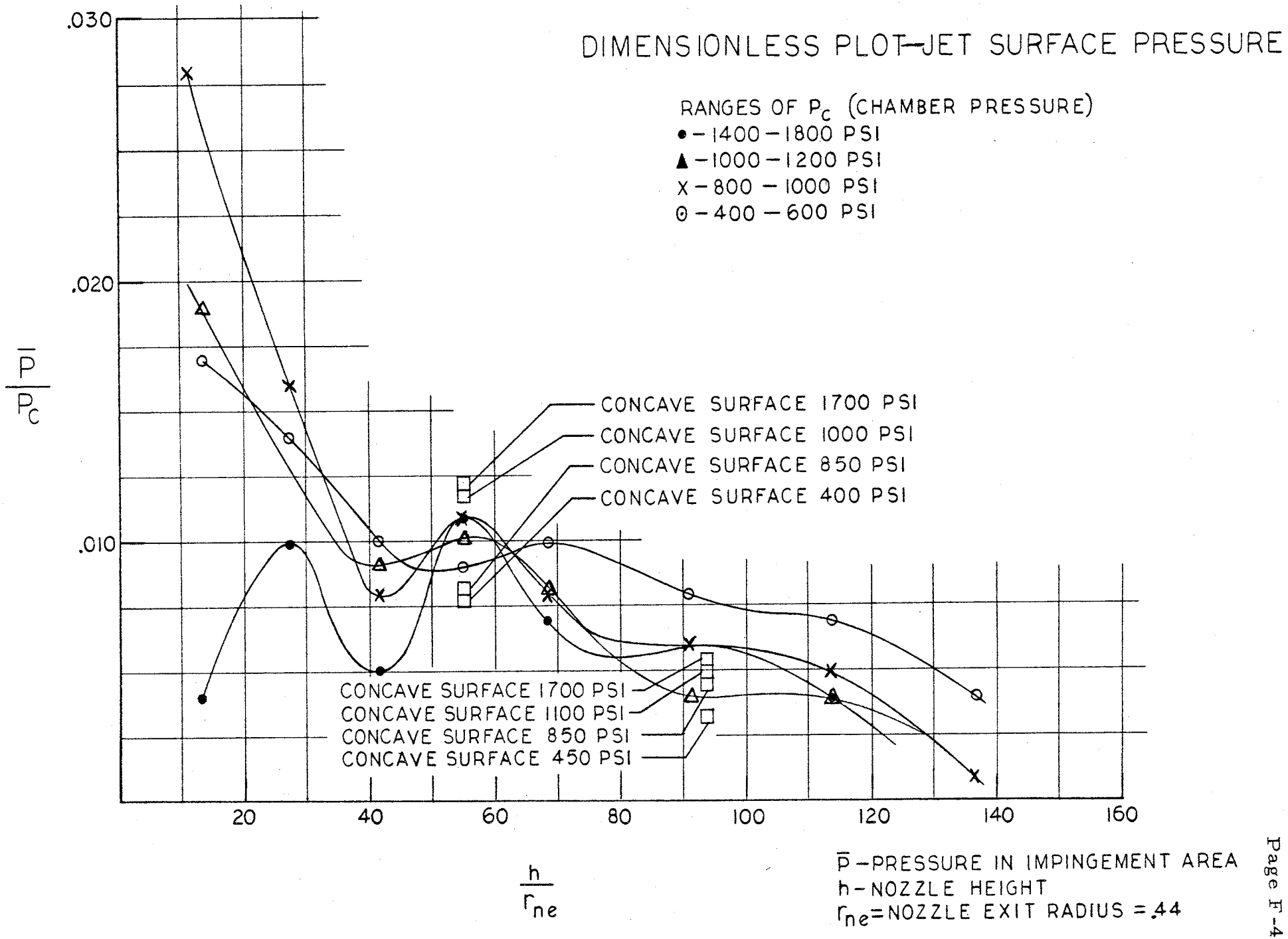
DIMENSIONLESS PLOT—JET SURFACE PRESSURE
RANGES OF P_c (CHAMBER PRESSURE)
● – 1400 – 1800 PSI
▲ – 1000 – 1200 PSI
X – 800 – 1000 PSI
⊙ – 400 – 600 PSI
CONCAVE SURFACE 1700 PSI
CONCAVE SURFACE 1000 PSI
CONCAVE SURFACE 850 PSI
CONCAVE SURFACE 400 PSI
CONCAVE SURFACE 1700 PSI
CONCAVE SURFACE 1100 PSI
CONCAVE SURFACE 850 PSI
CONCAVE SURFACE 450 PSI
.030
.020
.010
$\frac{\bar{P}}{P_c}$
20
40
60
80
100
120
140
160
$\frac{h}{r_{ne}}$
$\bar{P}$ – PRESSURE IN IMPINGEMENT AREA
h – NOZZLE HEIGHT
r_{ne} = NOZZLE EXIT RADIUS = .44

FIGURE 43

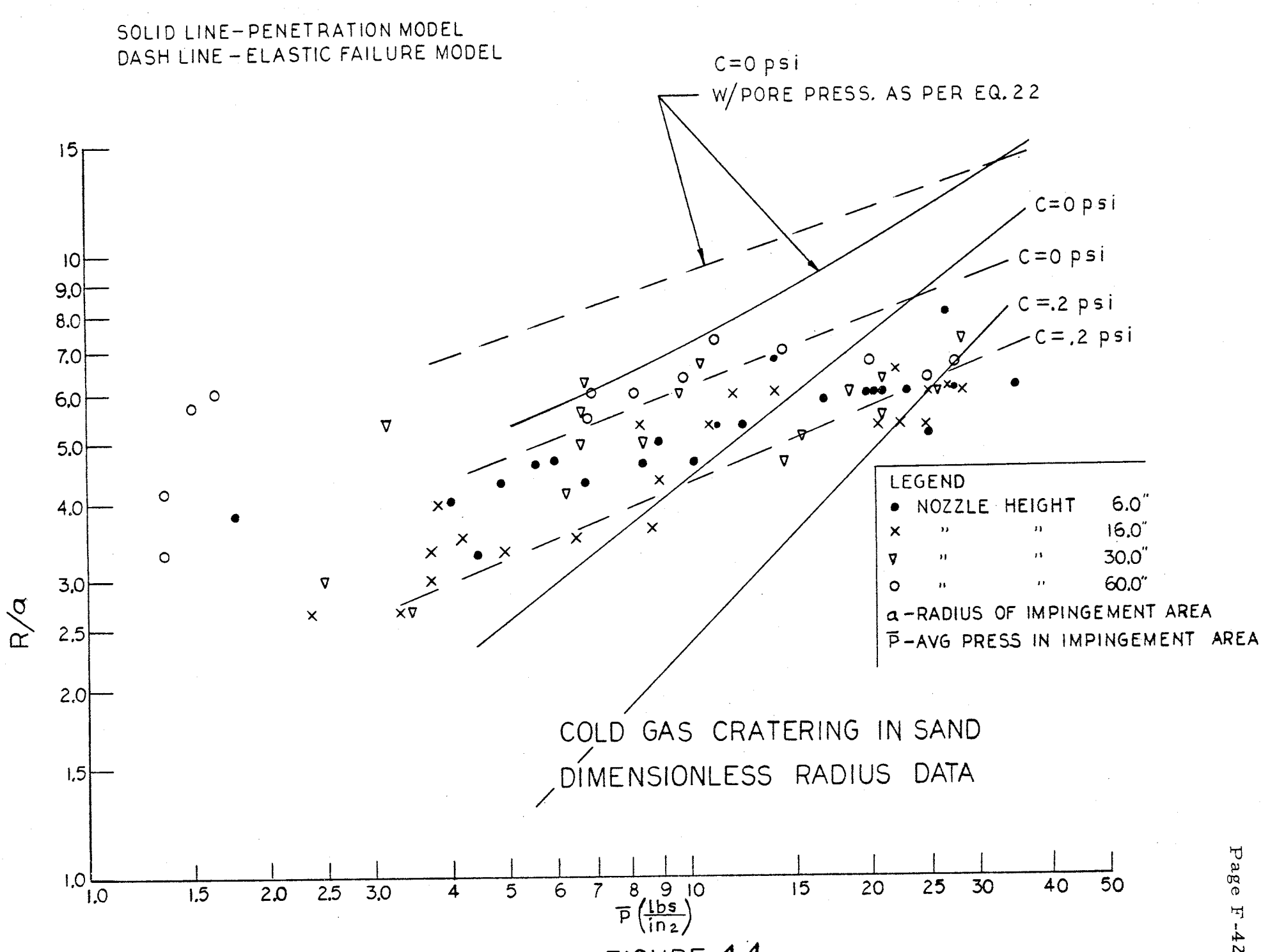
SOLID LINE – PENETRATION MODEL
DASH LINE – ELASTIC FAILURE MODEL
C=0 psi
W/PORE PRESS. AS PER EQ. 22
C=0 psi
C=0 psi
C=.2 psi
C=.2 psi
LEGEND
NOZZLE HEIGHT 6.0"
" " 16.0"
" " 30.0"
" " 60.0"
a – RADIUS OF IMPINGEMENT AREA
P̄ – AVG PRESS IN IMPINGEMENT AREA
R/a
15
10
9.0
8.0
7.0
6.0
5.0
4.0
3.0
2.5
2.0
1.5
1.0
1.0 1.5 2.0 2.5 3.0 4 5 6 7 8 9 10 15 20 25 30 40 50
P̄ (lbs/in2)
COLD GAS CRATERING IN SAND
DIMENSIONLESS RADIUS DATA

FIGURE 44

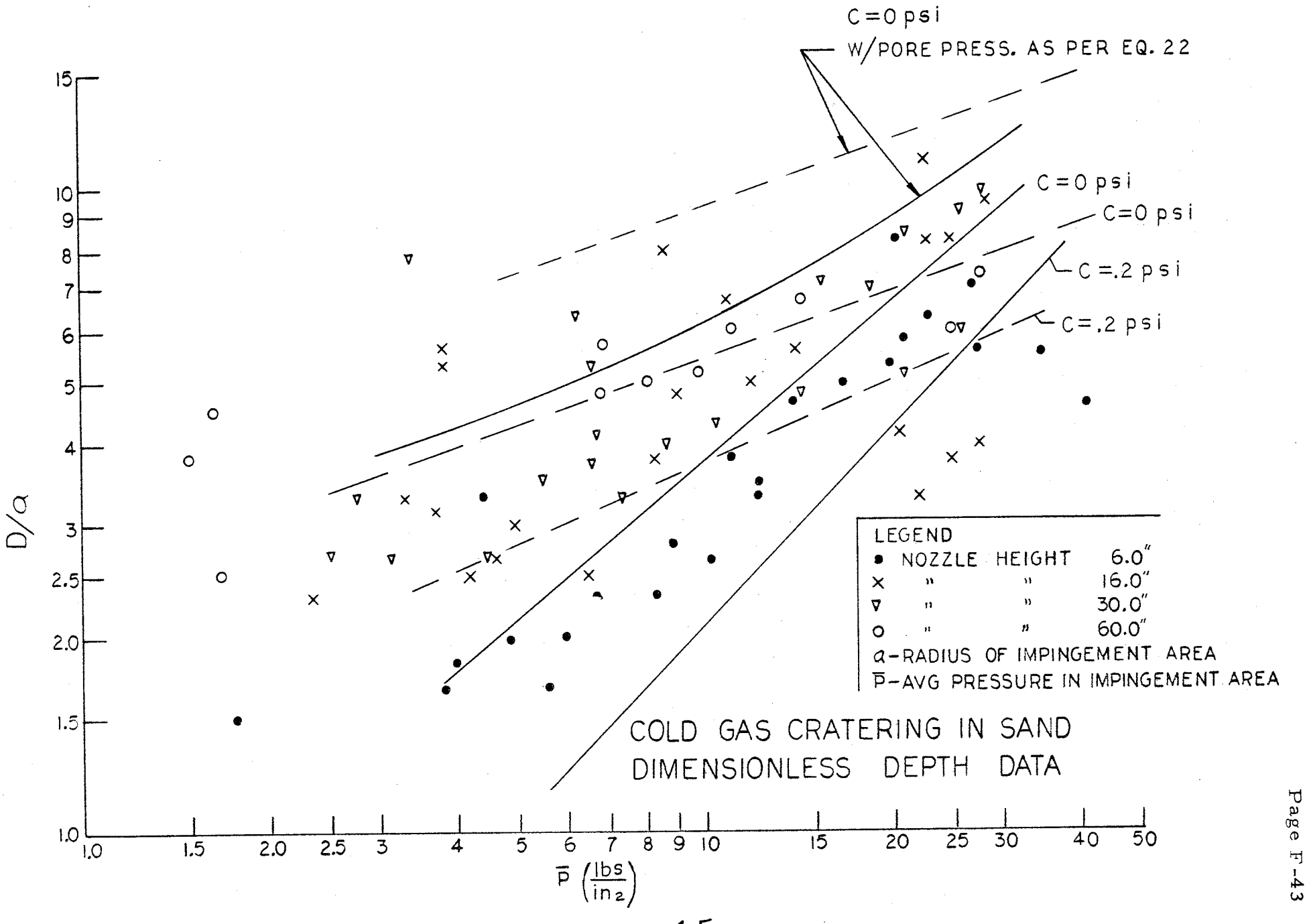
SOLID LINE – PENETRATION MODEL
DASH LINE – ELASTIC FAILURE MODEL
C = 0 psi
W/PORE PRESS. AS PER EQ. 22
C = 0 psi
C = 0 psi
C = .2 psi
C = .2 psi
LEGEND
• NOZZLE HEIGHT 6.0"
× " " 16.0"
▽ " " 30.0"
○ " " 60.0"
a – RADIUS OF IMPINGEMENT AREA
P̄ – AVG PRESSURE IN IMPINGEMENT AREA
COLD GAS CRATERING IN SAND
DIMENSIONLESS DEPTH DATA
D/a
P̄ (lbs/in²)
15
10
9
8
7
6
5
4
3
2.5
2.0
1.5
1.0
1.0
1.5
2.0
2.5
3
4
5
6
7
8
9
10
15
20
25
30
40
50

FIGURE 45

SOLID LINE-PENETRATION MODEL
DASH LINE-ELASTIC FAILURE MODEL

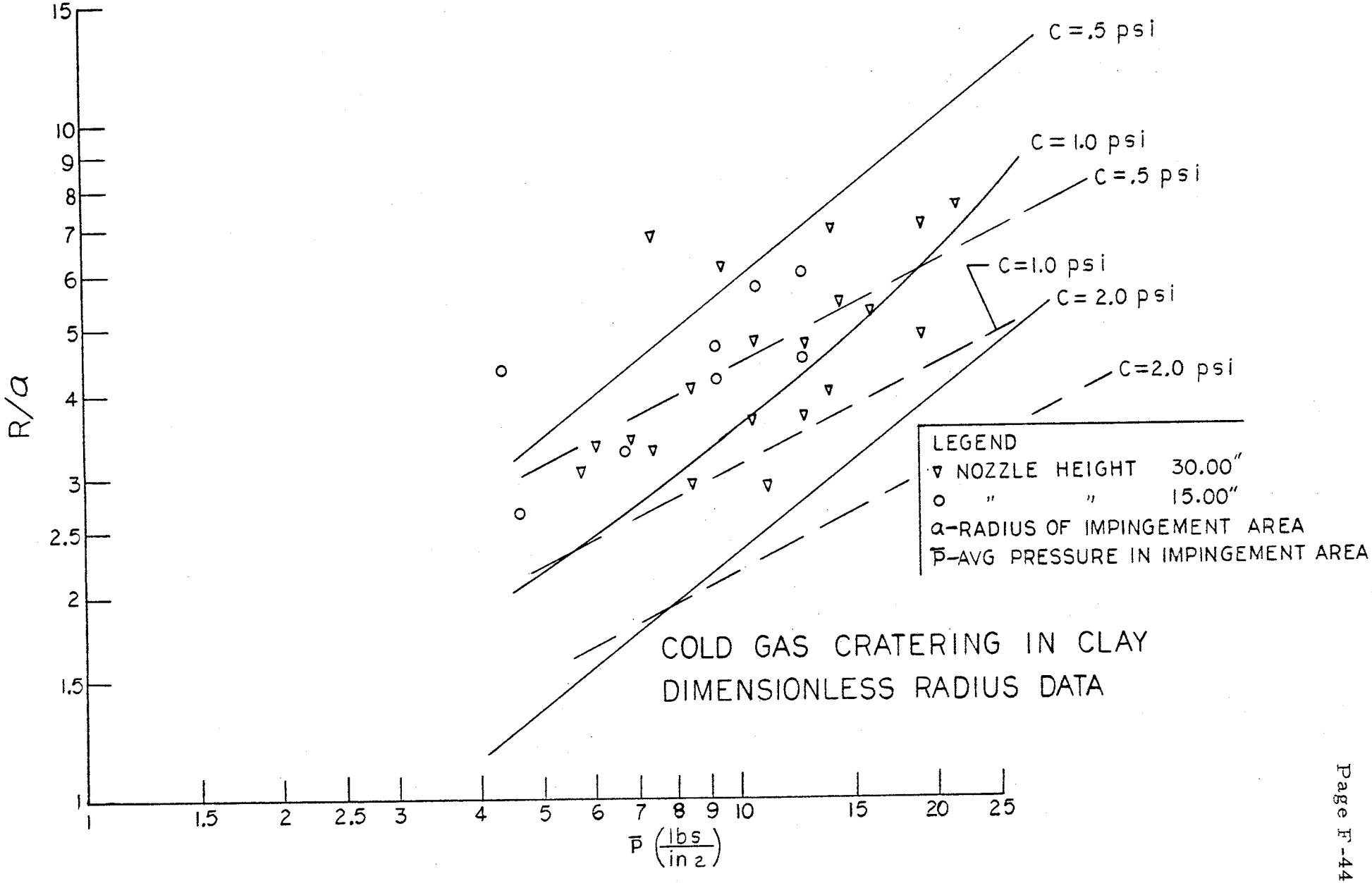

FIGURE 46

SOLID LINE–PENETRATION MODEL
DASH LINE–ELASTIC FAILURE MODEL

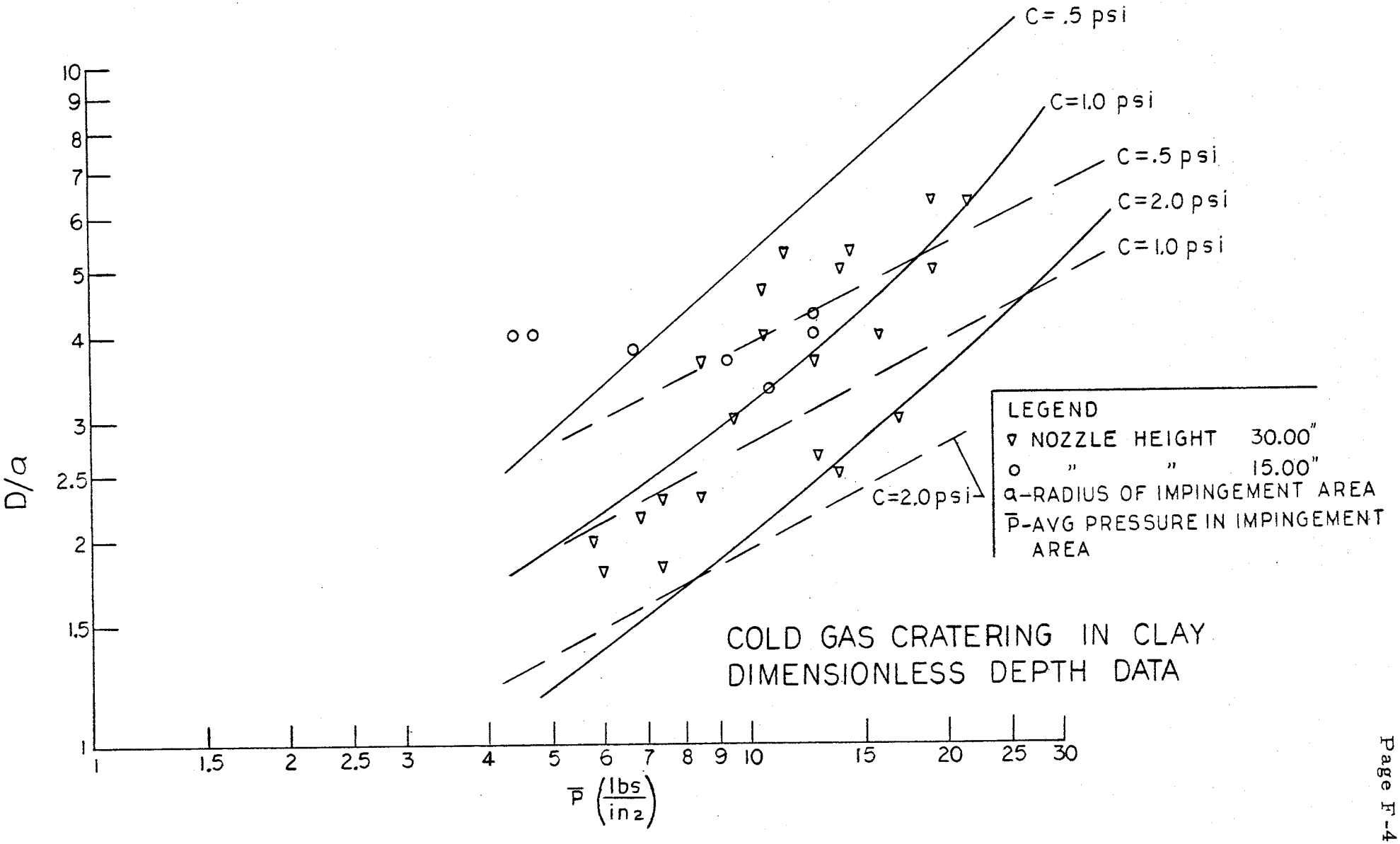

FIGURE 47

FASTAX FRAMES OF CRATERING ACTION

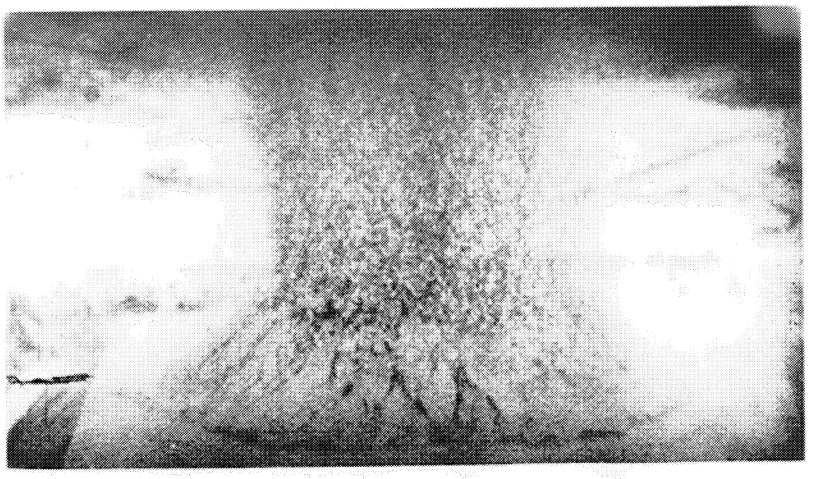

SAND

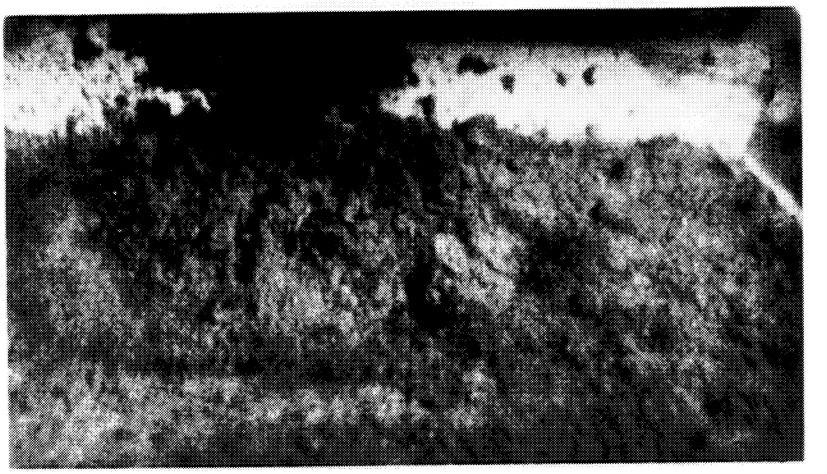

CLAY

FIGURE 48

PROJECTILE PENETRATION MODEL

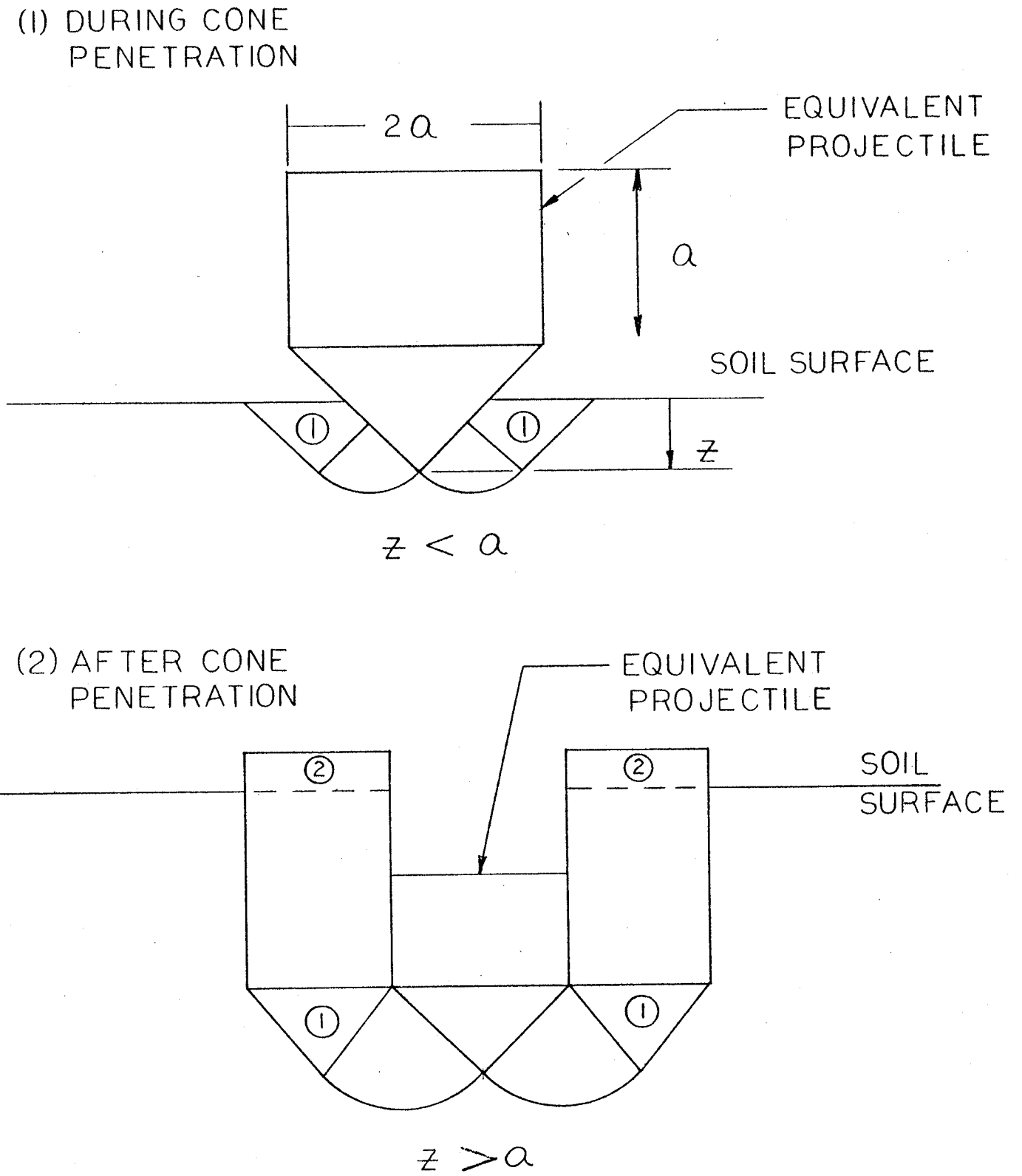

FIGURE 49

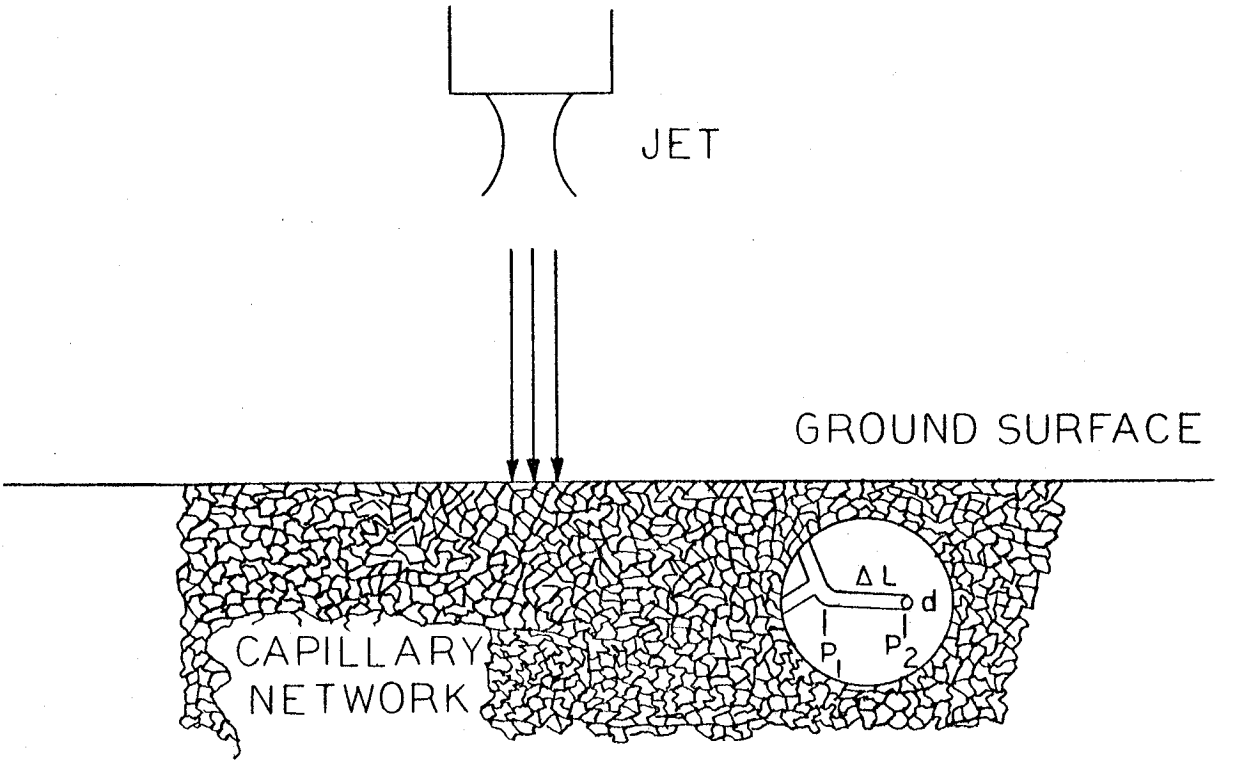

SOIL PORE PRESSURE MODEL

FIGURE 50

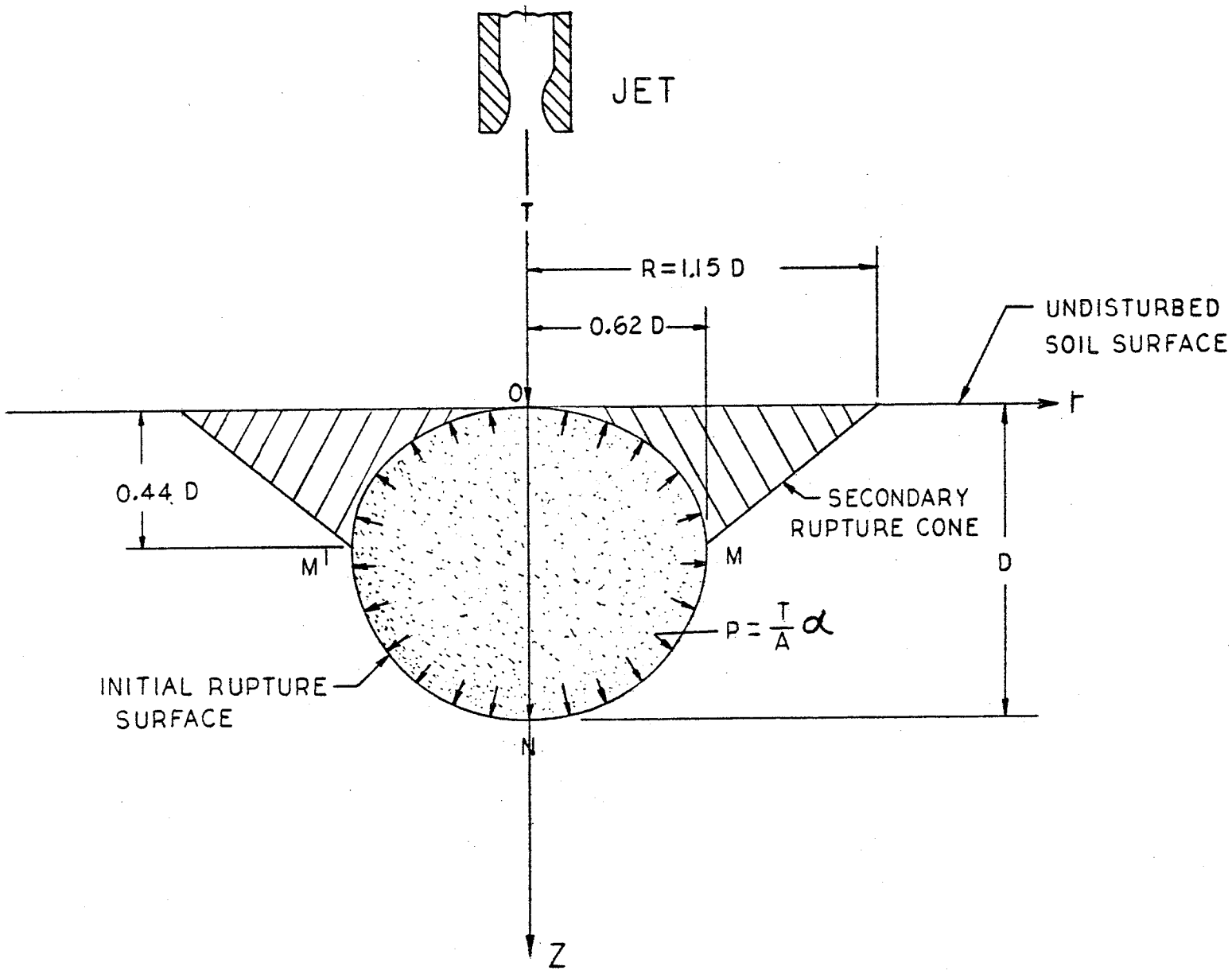

ELASTIC
CRATERING MODEL

FIGURE 51

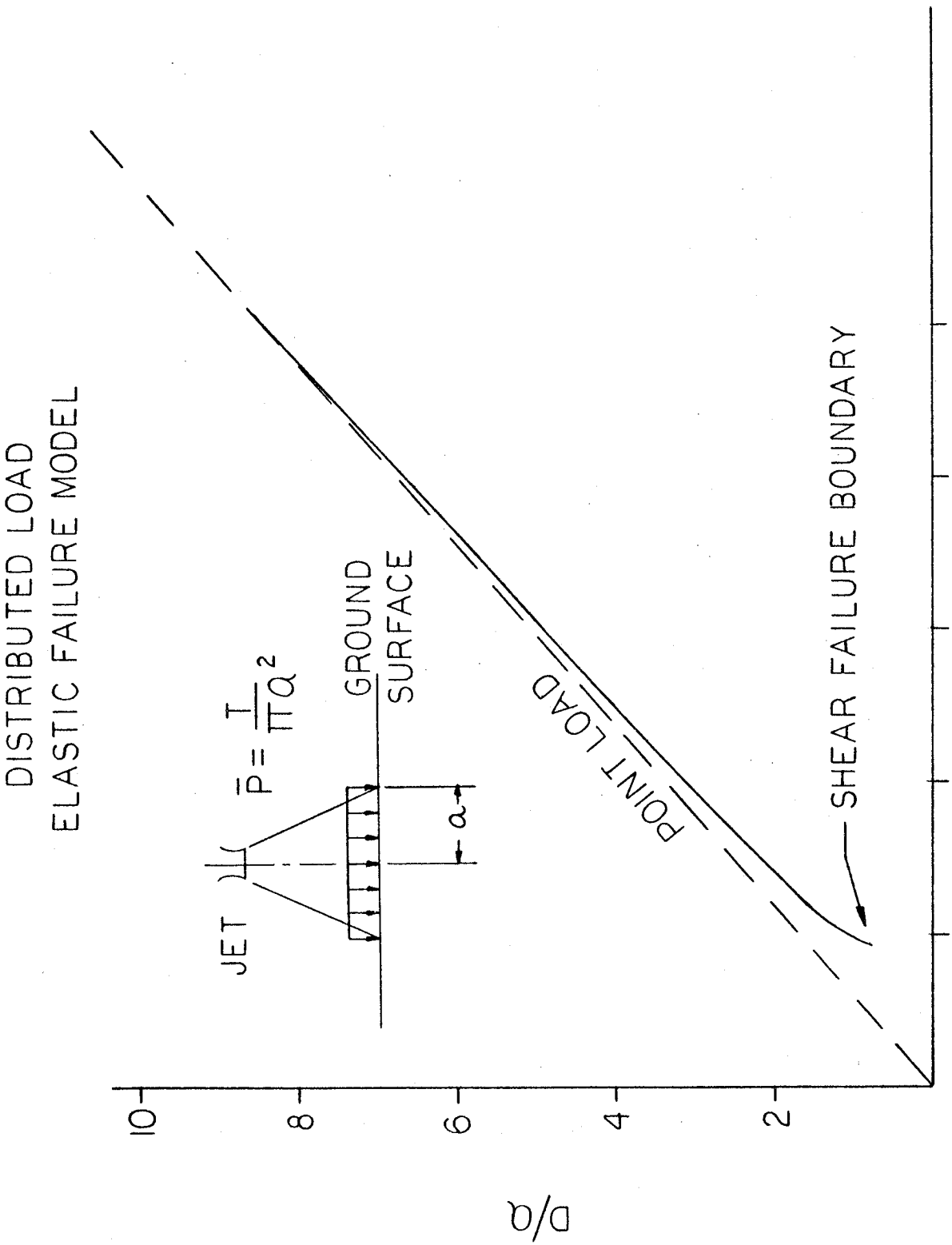
DISTRIBUTED LOAD
ELASTIC FAILURE MODEL
JET
$\bar{P} = \frac{I}{\pi Q^2}$
GROUND SURFACE
a
POINT LOAD
SHEAR FAILURE BOUNDARY
D/a
$\sqrt{\bar{P}/c}$
2
4
6
8
10

FIGURE 52